University of Zululand

Octupole degrees of freedom in Uranium-230

by

Mhlangano Freedom Nkalanga

Dissertation presented for the degree of Master of Physics in faculty of Science and Agriculture at the University of Zululand.

Supervisors:
Dr R. A. Bark,
Department of Subatomic Physics, iThemba LABS

Prof S. S. Ntshangase,
Department of Physics and Engineering, University of Zululand

June 2021

Abstract

The nuclei ^{230}U and ^{232}U were considered to possibly have tetrahedral shape because their negative-parity bands lacked in-band E2 transitions. From a study about the implications of tetrahedral shape in ^{230}U and ^{232}U [7], it was discovered that these bands were better described as octupole vibrations. This was concluded from the observation of the in-band E2 transitions from the negative-parity bands which contradicted the idea of tetrahedral shape. However, more in-band E2 transitions were observed in ^{232}U compared with ^{230}U where only one in-band E2 transition was observed.

This study seeks to observe in-band E2 transitions from the low-lying negative-parity states of ^{230}U. The nucleus ^{230}U was produced and studied at iThemba LABS using the reaction ^{232}Th(α, 6n)^{230}U at 63 MeV beam energy. Gamma-rays from ^{230}U were detected and measured with AFRODITE coupled to a recoil detector. The recoil detector was an essential tool in this measurement as it helps to suppress fission background that is associated with this type of reaction. The negative-parity band was extended with two new tentative states. No in-band E2 transtions were observed in the low-lying negative-parity states, and only one new tentative in-band E2 transition was observed from the new levels. Intrinsic dipole moments, energies of the observed states, and transitions are compared to systematics of neighboring nuclei. Related similarities in the intrinsic dipole moments, and energies are noticed in the systematics. These results still support octupole deformation rather than tetrahedral deformation.

Declaration

I Mhlangano Freedom Nkalanga hereby declare that this thesis is my work that has been not submitted anywhere for awards. Every source of information used in this thesis has been acknowledged.

Signature  .....

Acknowledgements

I would like to extend my thankfulness to my iThemba LABS supervisor, Dr R. A. Bark. I am thankful for the assistance, guidance, productive countless meetings and discussions, even though it was not easy because of the pandemic as some techniques required one-on-one explanations. I have benefited more from your expertise and knowledge. In this regard, I also thank my university supervisor Prof S. S. Ntshangase. I also wish to thank the following People: Dr T. D. Bucher to partake in the experiment set up, Linda Mdletshe and Abel Sithole for taking me through the data analysis steps. And thanks to everyone who took a shift during the experiment. And also thanks to Dr H. M. Kapau from the University of Zambia for the proofreading and suggestions he made. My special thanks go to iThemba LABS for providing research facilities, and the National Research Foundation (NRF) for opportunities and financial support to Students.

Contents

List of Figures

List of Tables

Chapter 1

Introduction

This Chapter introduces the study of *Octupole degrees of freedom in Uranium-230*. The chapter begins by providing background information pertaining the motivation for undertaking the study from the perspective of theoretical headways made on the subject and knowledge gaps that emerge from such. Thereafter, the chapter looks at the aim of the current study in the context of past works done on the subject and knowledge gaps that the current enquiry undertakes. It concludes by providing an outline for the thesis, aligned in the context of the established aim of the study.

In nuclear structure, nuclei can be described according to their shapes. The well known shapes are spherical, quadrupole, and octupole shapes. However, from theoretical studies, another form of nuclear shape that may exist is the tetrahedral shape [1–4]. This new shape is expected to manifest in the actinide region where octupole deformation is most favoured. This is not surprising as the tetrahedral shape is also a type of octupole deformation. Some of the nuclei suspected to have tetrahedral shape include the uranium isotopes, ^{230}U, and ^{232}U. The suspicion came from the hypothesis that negative-parity bands with no E2 transitions could be a signature of tetrahedrality [3–5]. The level schemes for the two uranium isotopes, ^{230}U and ^{232}U, had missing E2 transitions in their negative-parity bands, according to the early work by B. Ackermann *et al.,* [6]. Figure 1.1 shows the level schemes for ^{230}U, and ^{232}U [6].

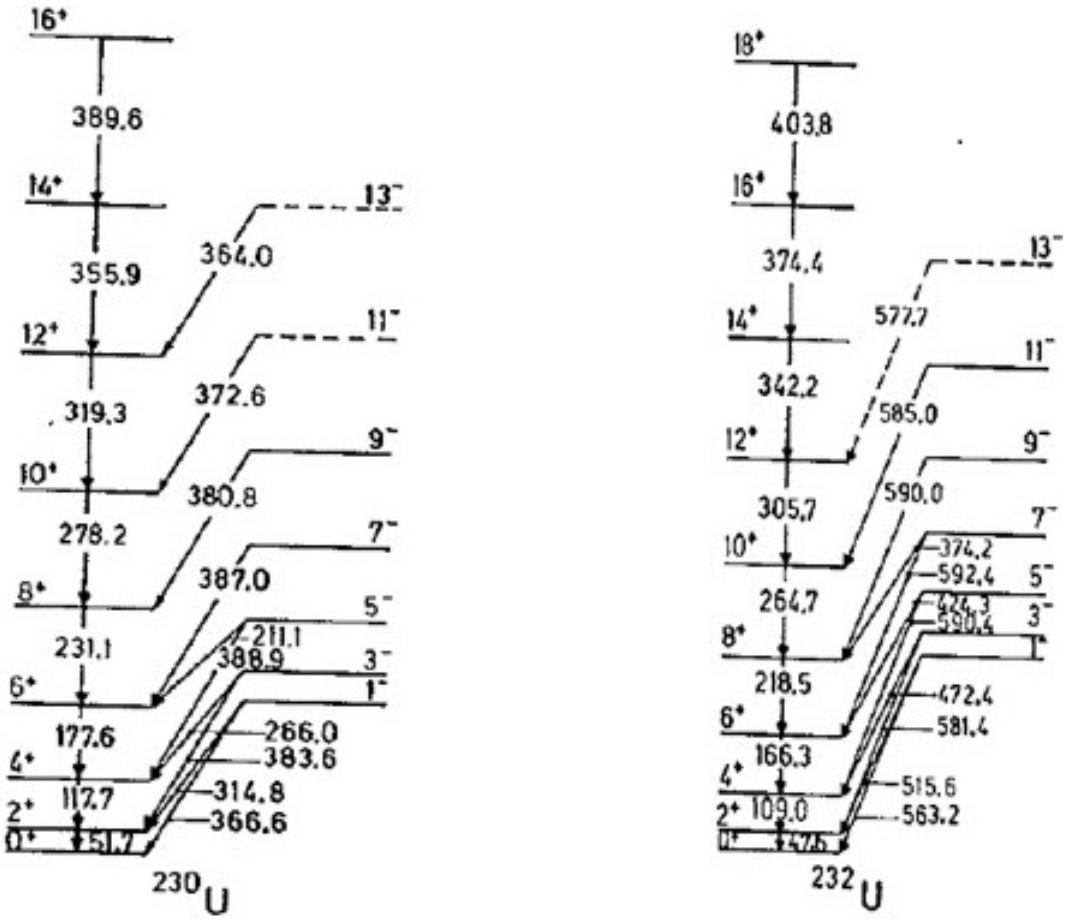

Figure 1.1: *Level schemes for Uranium-230 and Uranium-232 lacking in-band E2 transitions in their negative-parity bands [6].*

1.1 Motivation

In a study carried by S. S. Ntshangase *et al.*, it was found that the negative-parity bands of ^{230}U, and ^{232}U are better described as octupole vibrational bands, rather than bands of tetrahedral shape [7]. This came after the study made a remarkable discovery by observing E2 transitions in the negative-parity bands of the two isotopes. This overruled the existence of tetrahedral shape in ^{230}U and ^{232}U. Figure 1.2 shows the level schemes for ^{230}U, and ^{232}U after the study. These nuclei were produced using the nuclear reaction ^{232}Th + ^{4}He at 42 MeV for ^{232}U and 61 MeV for ^{230}U. Also, the experiment for this study was carried out with 8 clover detectors. However, for ^{230}U, only one E2 transition and one tentative E2 transition were observed in the negative-parity band, and the band had been populated to a lower spin compared to that of ^{232}U. Therefore, there is still much to be done to understand the negative-parity band of ^{230}U. It is of interest to study the nucleus again to

observe more E2 transitions in the negative-parity band.

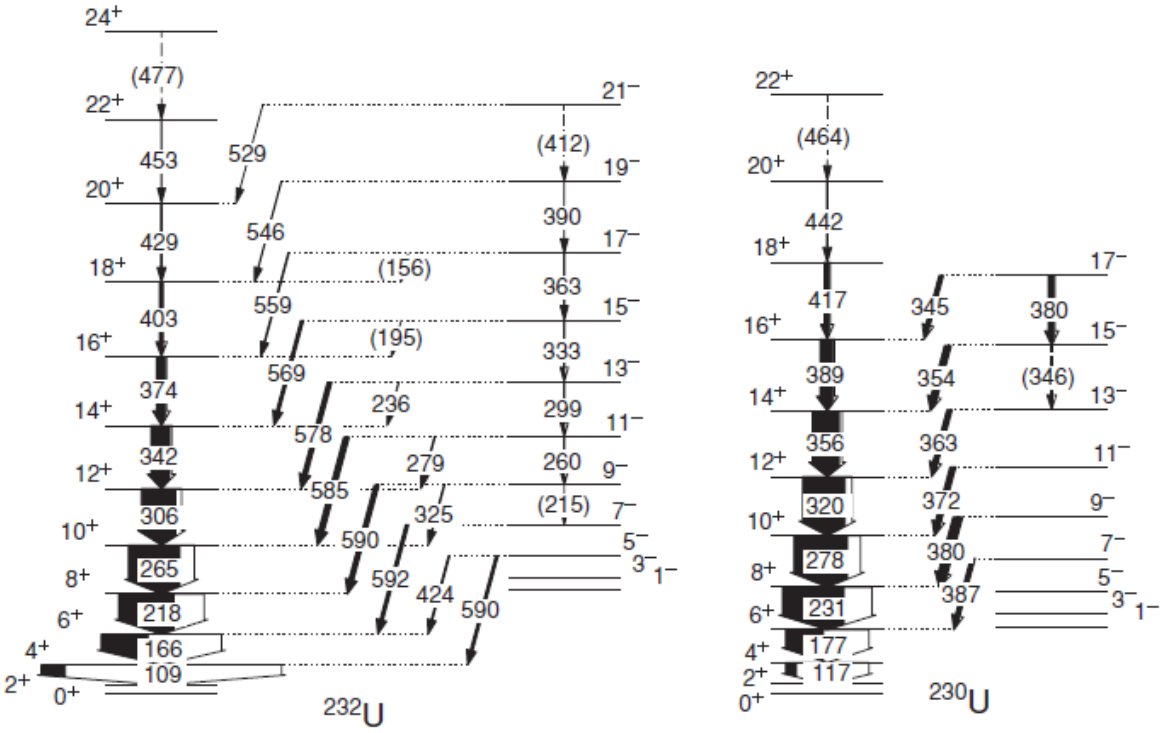

Figure 1.2: *The new level schemes of Uranium 232(left) and Uranium 230 (right) [7].*

1.2 Aim of the study

The work covered in this thesis is focused on understanding the nucleus of ^{230}U. The study aims to understand whether the low-lying negative-parity states of this nucleus are of tetrahedral, or octupole vibrational in nature. The study aims to achieve this by observing E2 transitions in low-lying negative-parity states, and may be extend the negative-parity band to a higher spin in the hope of observing more E2 transitions. The reaction will be carried out at 63 MeV with extra four clover detectors compared to 61 MeV from the previous experiment [7].

1.3 Thesis outline

This thesis consists of five chapters, with each chapter addressing specific issues related to the aim of the thesis, as follows:

- Chapter 1 has contextualised the study, providing motivation for its undertaking and clearly stating the aim of the study.
- In Chapter 2, gives an overview of the theoretical background of nuclear structure.
- Chapter 3 lays out the experimental setup and techniques conducted to perform the experiment. It provides a methodological basis informing the experimental setup and techniques that guided the study.
- Chapter 4 describes the data analysis.
- Chapter 5 presents the results in the context of the aim of the study, and discussion.
- Lastly, Chapter 6 provides the summary and conclusion to the study.

Chapter 2

Nuclear properties

The current chapter focuses on nuclear properties as part of the theoretical framework of the study. The chapter discusses, among other things, nuclear shapes, octupole deformation, symmetry rotation, nuclear excitation, electromagnetic transition rates, octupole correlations, tetrahedral shapes and tetrahedral bands.

2.1 Nuclear deformation

Nuclei are made up of nucleons (protons and neutrons). The nucleons occupy shells of increasing energy, from lowest to the highest energy shell depending on the number of nucleons. Nuclei having closed shells (fully-filled shells) are spherical in shape. Nuclei with open shells (not fully-filled shells) are deformed in shape. Deformation is due to the arrangement of the nucleons in the unfilled shells; this effect is greatest when the shells are half-filled (i.e. nuclei with half-filled shells are characterized by more deformed shapes). As the shells become close to full, deformation decrease, and the spherical shape is restored [8].

2.2 Nuclear shapes

Nuclear shapes can be represented in terms of spherical harmonics $Y_\lambda^\mu(\theta,\phi)$ [8]. The distance from the center to surface of the nucleus can be written as an expansion in spherical harmonics.

$$R(\theta,\phi) = R_0\left[1 + \sum_{\lambda=0}^{\infty}\sum_{\mu=-\lambda}^{\lambda}\alpha_{\lambda\mu}Y_\lambda^\mu(\theta,\phi)\right] \tag{2.1}$$

where R_0 is the radius of a spherically shaped nucleus with a constant volume. The coefficient $\alpha_{\lambda\mu}$ is the shape parameter which describes the changes in the nuclear shape with respect to the multipole order λ. The parameter λ gives the deformation type (spherical, quadrupole, octupole, etc) for the nucleus [2, 8].

For $\lambda = 0$, which defines a monopole, the nucleus is spherical with no deformation and the parameter α_{00} only changes the radius of the sphere. The volume of the nucleus should remain constant in any deformation. For $\lambda = 1$, which defines a dipole, the parameter $\alpha_{1\mu}$ translates the shape of the nucleus without deforming it, i.e; without changing its shape. Figure 2.1 shows how the monopole and dipole terms affect the nucleus without changing its shape [8, 9].

Therefore, the lowest important multipole order is $\lambda = 2$, which defines a quadrupole shape; the second significant multipole order is $\lambda = 3$; which defines an octupole shape. Figure 2.2 compares the spherical shape with quadrupole, and octupole deformations [8, 9].

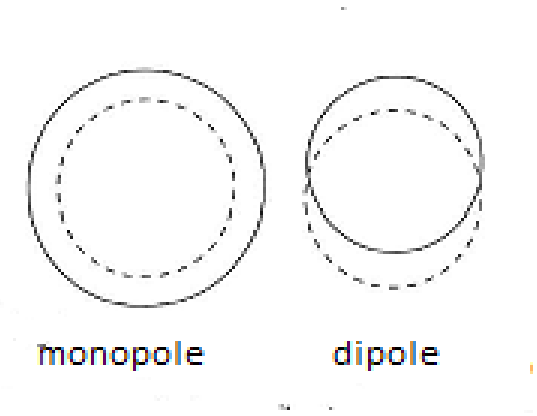

Figure 2.1: *The solid line is the equilibrium shape of the nucleus and the dashed line is the deformed shape [8].*

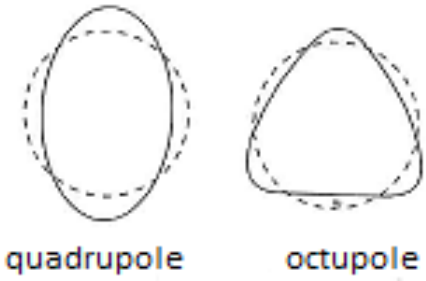

Figure 2.2: *Nuclear deformation from spherical to quadrupole, and from spherical to octupole* [8].

2.2.1 Quadrupole shape

Quadrupole deformed nuclei are defined by $\lambda = 2$, the spherical harmonic Y_2^{μ} and the coefficients α_{21}, α_{22}, α_{20}, α_{2-1}, and α_{2-2}. Due to the symmetry that the nucleus possesses, the parameters are reduced to α_{20} and $\alpha_{22} = \alpha_{2,-2}$, the other coefficients vanish as a result of the symmetry [9, 10]. Figure 2.3 shows a nucleus having axially symmetric quadrupole deformation. In general, the radius of a quadrupole shaped-nucleus will be defined by the equation:

$$R(\theta, \phi) = R_0[\,1 + \alpha_{20} Y_2^0 + \alpha_{22}(Y_2^2 + Y_2^{-2})] \tag{2.2}$$

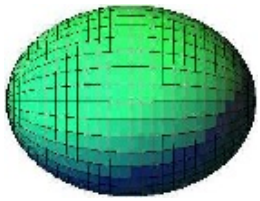

Figure 2.3: *A symmetric quadrupole deformed nucleus.*

A very often used parameterization of the quadrupole deformation is the Lund convention. It uses two sets of parameters which are β_2 and γ, where β_2 defines how much the nucleus is axially deformed. The larger β_2 is, the more deformed the nucleus is, and the smaller β_2 is, the less deformed the nucleus is. The parameter γ, is an angle defining the triaxiality of the shape i.e, whether the nucleus is axially symmetric or not, and to what degree. The relationship between the coefficients α_{20}, and α_{22} with the deformation parameters β_2, and γ is defined by the equations [9, 10]:

$$\alpha_{20} = \beta_2 cos\gamma \tag{2.3}$$

$$\alpha_{22} = \frac{1}{\sqrt{2}}\beta_2 sin\gamma \tag{2.4}$$

The variation of nuclear shapes with γ is shown in figure 2.4. For $\gamma = 0°$, the nuclear shape corresponds to what is called a prolate deformation for positive β, and to an oblate deformation for negative β. For $\gamma = 60°$, the nucleus corresponds to an oblate deformation for positive β ,and prolate deformation for negative β. The nuclear shape is axially symmetric for values of $\gamma = 60°$, 0, $-60°$, and $-120°$ and triaxial for any other values of γ [9,10]. The prolate, oblate, and triaxial shapes are shown in figure 2.5.

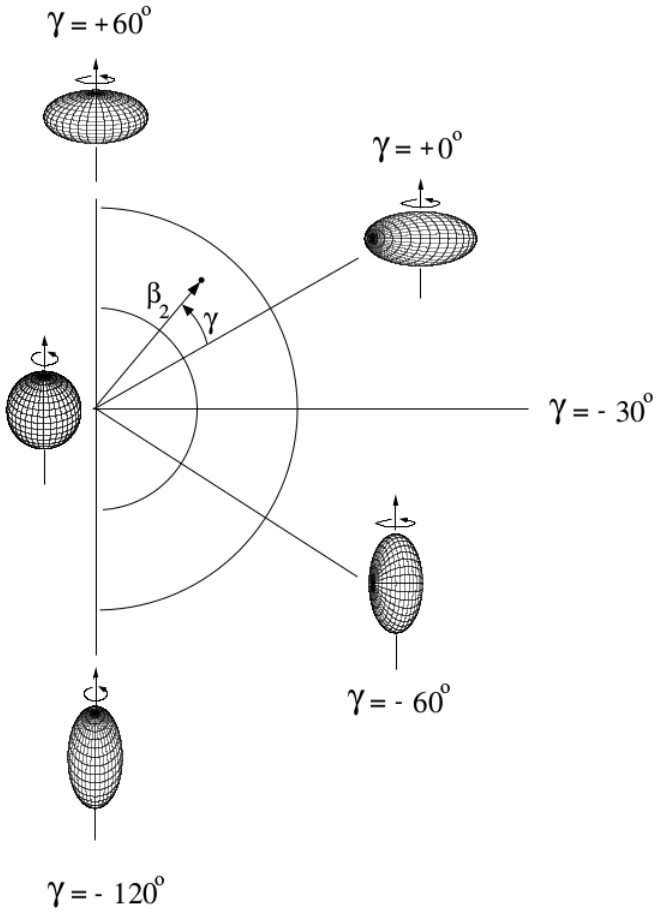

Figure 2.4: *The Lund convention of nuclear shape corresponding to the different values of γ [11].*

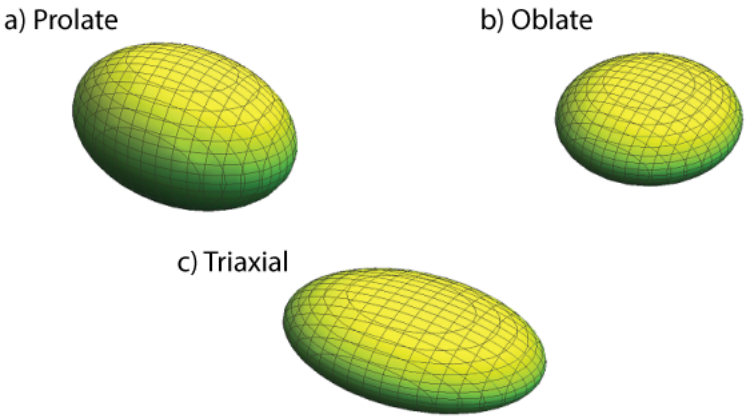

Figure 2.5: *Axially symmetric shaped nuclei (a) and (b), triaxial shaped nucleus (c) [12].*

2.2.2 Octupole shape

The octupole shape is defined by $\lambda = 3$, the spherical harmonic Y_3^μ and the coefficient $\alpha_{3\mu}$. The coefficient α_{30} gives the nucleus has a pear-like shape. The pear-shape is reflection asymmetric i.e, the shape flips if $r \rightarrow -r$ (r is the axis of symmetry) [13]. Reflection asymmetry could explain the observation of negative-parity states next to the ground state band; this will be discussed in section 2.4. Figure 2.6 shows an example of an octupole shaped nucleus.

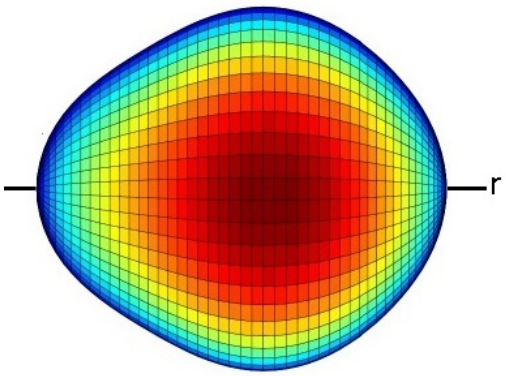

Figure 2.6: *A schematic diagram of how an octupole deformed (pear-shape) nucleus looks [14].*

2.3 Octupole deformation

Unlike quadrupole deformation that exists almost across the entire nuclear chart, octupole deformation manifests for specific numbers of protons (Z) and neutrons (N). Figure 2.7 shows that it is when either N or Z, or both, are near: 34, 56, 88, or 134. The left-hand side of figure 2.7 shows the orbitals filled or occupied by these number of nucleons, and the right-hand side shows where such nuclei lay on the nuclear chart. The selected orbitals show that octupole deformation results from the interactions of nucleons occupying orbitals which have a difference of 3 units in orbital angular momentum ($\Delta \boldsymbol{l} = 3$), and a difference of 3 units in total angular momentum ($\Delta \boldsymbol{j} = 3$) [14–17]. Figure 2.7 clearly shows that the orbitals, where the interactions occur are: the $\boldsymbol{j}_{15/2}$ orbital with the $\boldsymbol{g}_{9/2}$ orbital, the orbital $\boldsymbol{i}_{13/2}$ with the $\boldsymbol{f}_{7/2}$ orbital, the orbital $\boldsymbol{h}_{11/2}$ with the $\boldsymbol{d}_{5/2}$ orbital, and the orbital $\boldsymbol{g}_{9/2}$ with the $\boldsymbol{p}_{3/2}$ orbital.

Octupole deformation is expected to manifest in the Radon-Radium, and in the Thorium-Uranium mass regions. Practical examples of these interactions leading to octupole deformation are in $^{220}_{86}$Rn and $^{224}_{88}$Ra [14,17]. In these nuclei, the Fermi surface for protons is on the $\boldsymbol{f}_{7/2}$ orbital, which interacts with the $\boldsymbol{i}_{13/2}$ orbital. For neutrons, the Fermi surface is on the $\boldsymbol{g}_{9/2}$ orbital which interacts with the $\boldsymbol{j}_{15/2}$ orbital [17]. These arrangements for Z and N give $^{220}_{86}$Rn and $^{224}_{88}$Ra octupole deformations.

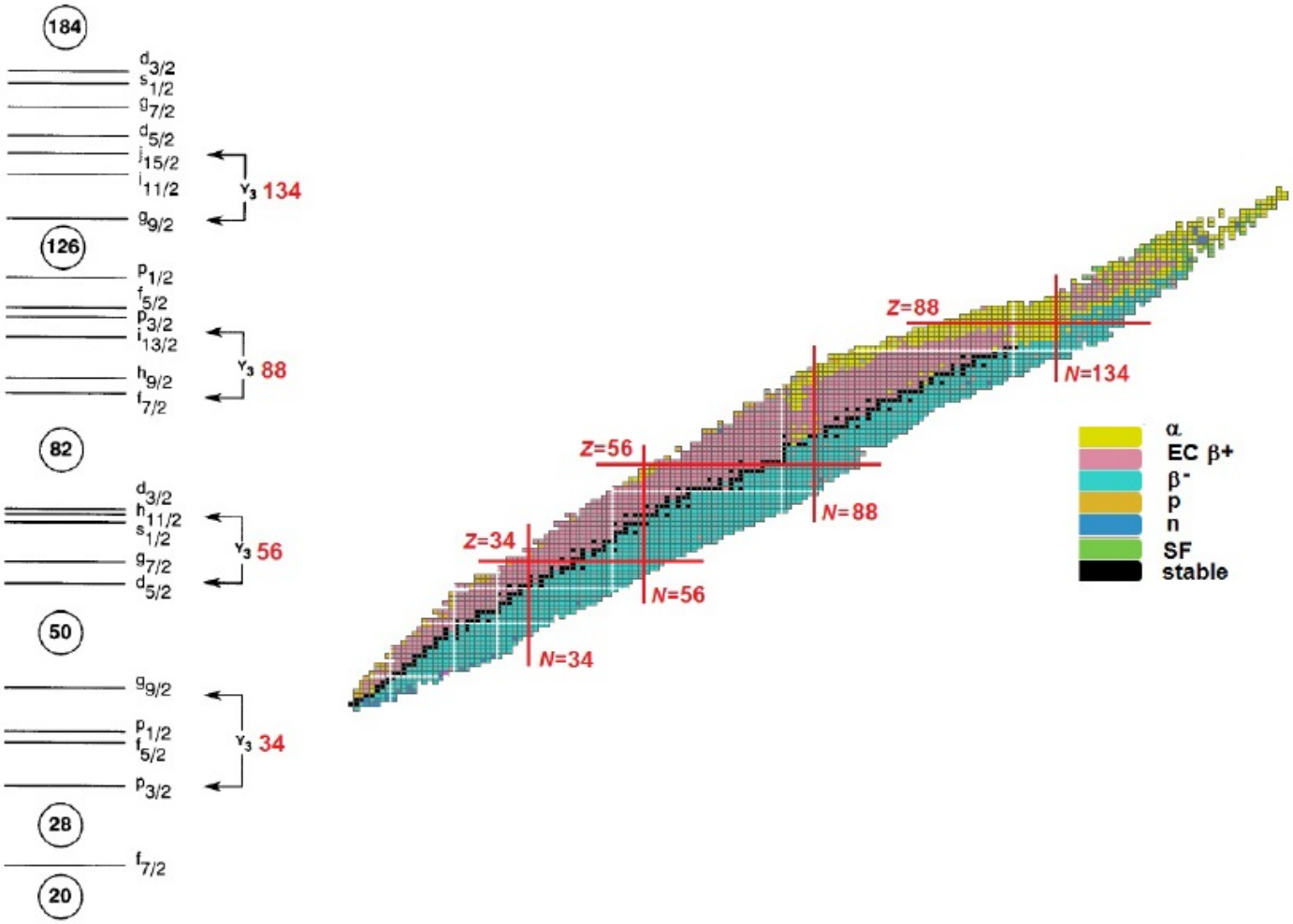

Figure 2.7: *A figure showing the energy levels for octupole deformation and where the deformation manifests on the nuclear chart, on the nuclear chart Z is horizontal and N the vertical [14].*

2.4 Nuclear excitation

Nuclei with more energy compared to their ground state may rotate. From quantum mechanics a sphere can not rotate as there are no observable changes due to symmetry, so only deformed nuclei can rotate. Classically, the magnitude of the angular momentum for a rotating object is given by:

$$L = \mathcal{J}\omega \tag{2.5}$$

where $\mathcal{J}$ is the moment of inertia and ω is the angular speed. With the square of the angular momentum taken from quantum mechanics, $l(l+1)\hbar^2$, the energy of the rotating object is given by:

$$E_R(l) = \frac{1}{2}\mathcal{J}\omega^2 = \frac{(\mathcal{J}\omega)^2}{2\mathcal{J}} = \frac{l(l+1)\hbar^2}{2\mathcal{J}} \tag{2.6}$$

Equation 2.6 determines the excitation energies for the levels of a deformed rotating nucleus. A large moment of inertia means that the nucleus is more deformed. Therefore, from equation 2.6 the excitation energies will be lower, such as in super-deformation ($\beta_2 = 0.6$) and hyper-deformation ($\beta_2 = 0.9$) compared to less deformed nuclei.

2.5 Reflection-asymmetry

A nucleus having reflection-symmetry is shown in figure 2.3. For an even-even rotating reflection-symmetric nucleus, the energy levels of the rotational band will have spin and parity of the sequence, $0^+, 2^+, 4^+, ...$ All energy levels of the rotational band will have the same positive-parity under space inversion because of symmetry [13,14]. The rotational band created by a rotating even-even reflection-symmetric nucleus is shown in figure 2.8. The spin and parity of the energy levels (states) are labeled as I^π, and are indicated on the right side of each level.

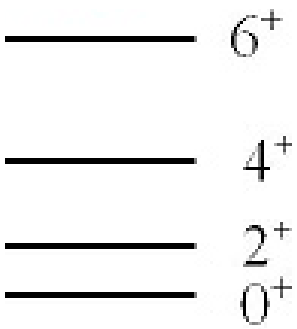

Figure 2.8: *Rotational band of even-even reflection-symmetric nucleus.*

A nucleus having octupole vibrations, and a nucleus having static octupole deformation are shown in (a) and (b) in figure 2.9, respectively. These are reflection-asymmetric nuclei. For an even-even rotating reflection-asymmetric nucleus, the rotational band $I^\pi = 0^+, 2^+, 4^+, ...$ is accompanied by energy levels with negative-parity. The collective model predicts that the negative-parity states arise as

a result of reflection-asymmetry in octupole deformation [18, 19]. Figure 2.10 show plots of nuclear potential energy, V, as a function of octupole deformation parameter β_3. When a symmetric nucleus acquires octupole deformation, there will be symmetry breaking. In figure 2.10(a), the potential energy has a minimum at $\beta_3 = 0$. The nucleus is axially symmetric and has reflection symmetry. In figure 2.10(b), a barrier at $\beta_3 = 0$ on the nuclear potential energy develops, the nucleus begins to have octupole vibrations as asymmetry is introduced. These vibrations appear as the side band having energy levels with spin and parity of the sequence $I^\pi = 1^-, 3^-, 5^-...$, next to the positive-parity rotational band. The negative-parity energy levels appear at higher energy relative to the positive-parity energy levels (ground state band). Practical examples of octupole vibrations are the nuclei of ^{232}U [7], the nuclei of ^{218,220,222}Rn, and nuclei of ^{228,230,232,234}Th, and ^{228}Ra [20]. In these nuclei, negative-parity states are observed sitting higher in energy relative to the positive-parity states, and the bands of the negative-parity states are interpreted as an octupole vibrators

When the nucleus continues to deform to a stable octupole deformation, the negative-parity states are lowered in energy, and may also interleave with the positive-parity states. At this stage, reflection-symmetry is completely broken, and reflection-asymmetry is matured, see figure 2.10(c). Experimental evidence of static octupole deformation is observed in the nuclei of ^{222,224,226}Ra, and ^{226}Th. In these nuclei, the negative-parity states are lowered in energy and interleave with the positive-parity states [13, 20, 21].

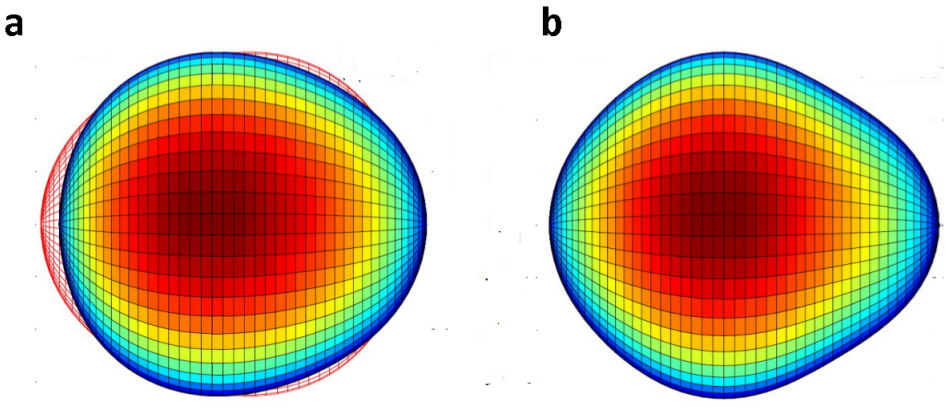

Figure 2.9: *Reflection-asymmetric nuclei. (a) Octupole vibration , and (b) Static octupole. The blue to red colour scale represents the y-values of the surface [14].*

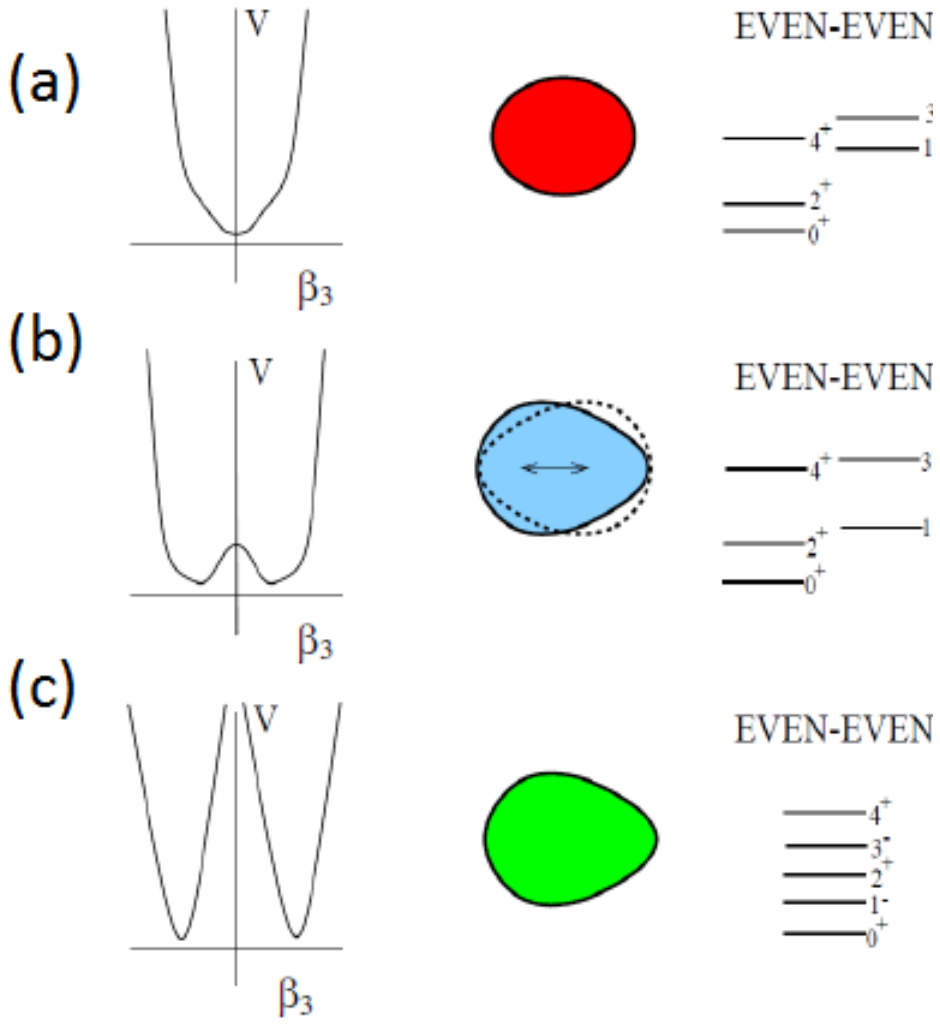

Figure 2.10: *Plots of potentials energy V, as a function of octupole deformation β_3. (a) represents a nucleus which is axially and reflection symmetry (c) corresponds to a static octupole deformed nucleus, and (b) is an intermediate form between (a) and (c) [10].*

2.6 Electromagnetic transition rates

Nuclei prefer to exist in their ground state. When a nucleus is in a state above the ground state, it can reach the ground state by emitting energy in the form of gamma-rays (chapter 4 explains in detail how the ground state is achieved). Figure 2.11 shows a transition from a state of higher energy to a state of lower energy. The energy of the gamma-ray is given by equation 2.7, while the angular momentum and parity are determined from those of the final and initial states using selection rules in equations 2.8 and 2.9.

$$E_\gamma = \Delta E_R \approx E_i - E_f \tag{2.7}$$

$$\mathbf{L}_i - \mathbf{L}_f \leq \mathbf{L}_\gamma \leq \mathbf{L}_i + \mathbf{L}_f \tag{2.8}$$

$$\pi_\gamma = \pi_f \cdot \pi_i \tag{2.9}$$

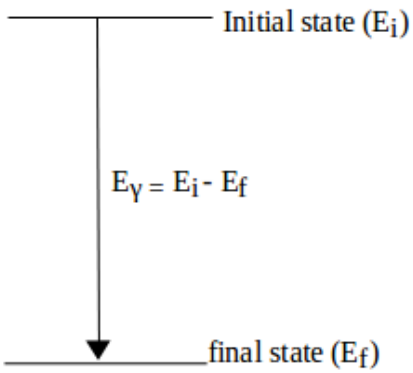

Figure 2.11: *Nucleus transition between two nuclear states.*

The gamma-ray can be magnetic (Mλ) or electric (Eλ) in nature having multipolarity $L = 1$ (dipole), 2 (quadrupole), 3 (octupole), and so on. Each corresponding λ units of angular momentum L. The emission probability in Weisskopf units (W.u) [8, 22], for the gamma-ray is given by the equation:

$$T(\sigma L) = \frac{P(\sigma L)}{\hbar\omega} = \frac{8\pi(L+1)}{L\hbar[(2L+1)!!]^2}\left[\frac{E\gamma}{\hbar c}\right]^{2L+1} B(\sigma L) \tag{2.10}$$

where σ can be E (electric) or M (magnetic), $\hbar\,\omega$ is the energy of the emitted gamma-ray photons, ω is the angular frequency of the radiation, $P(\sigma\lambda)$ is the power carried away by the electric or magnetic radiation, and $B(\sigma\lambda)$ is the reduced transition probability; the square of the modulus of the nuclear

matrix element. Equation 2.11 shows the relation.

$$B(\sigma\lambda, I_i \rightarrow I_f) = \frac{1}{2I_i + 1} | < I_f \| \hat{\mathbf{O}}_\lambda \| I_i > |^2 \tag{2.11}$$

where $\hat{\mathbf{O}}_{\sigma\lambda}$ is the multipole moment operator for changing the nucleus from an initial state to a final state through the emission of a gamma-ray. The type or nature of the emitted gamma-ray is determined by the parity of the states involved in the transition, as tabulated in table 2.1. For example, if the emitted gamma-ray is of multipole order $L = 1$, then its nature (i.e electric or magnetic) will be determined by whether or not parity changes. If the parity changes from the initial state to the final state, the radiation will be of E1 type, and if not, then the radiation will be of M1 type. The same rule applies to the other multipole orders. The multipole order also describes the distribution of matter in nuclei (see equation 2.1); this distribution determines the shape of a nucleus. However, the shape of a nucleus is not directly measured or observed from experiments, instead the electromagnetic transitions serve as the experimental observables.

Table 2.1: *Electromagnetic transitions.*

Radiation type	E1	M1	E2	M2	E3	M3	E4	M4	E5	M5
Change in Parity	Yes	No	No	Yes	Yes	No	No	Yes	Yes	No

2.6.1 E2 transitions

E2 transitions depend on the electric quadrupole moment operator Q_0. In the rotational model, the probability per unit time for E2 transitions will be given by equation 2.10, and the reduced transition probability $B(E2; I_i \rightarrow I_f)$ is given by [13, 23]:

$$B(E2, I_i \rightarrow I_f) = \frac{5}{16\pi} Q_0^2 < I_i K_i 20 | I_f K_f >^2 \tag{2.12}$$

in which $< I_i K_i 20 | I_f K_f >$ is the Clebsch-Gordon coeffecient for the the connected states, e is the elementary charge, and Q_0 is the intrinsic quadrupole moment and it is related to quadrupole deformation parameter β_2 from equations 2.3 and 2.4 as:

$$Q_0 = \frac{3}{\sqrt{5\pi}} Z R^2 \beta_2 \tag{2.13}$$

Therefore, E2 transitions will serve as an experimental observable for quadrupole deformed nuclei [18] and rotational bands of quadrupole deformed nuclei (as the one illustrated in figure 2.8) will be connected by a cascade of E2 transitions as shown in figure 2.12.

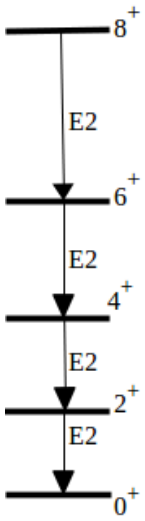

Figure 2.12: *A level scheme showing the cascade of E2 transitions linking the states of the rotational band for a quadrupole deformed nucleus.*

2.6.2 E1 transitions

For octupole deformation, there will be an addition of electric dipole moments (E1 transitions) connecting states of different parity [18]. In a pear-shaped nucleus, the protons accumulate at the pointed narrow end of the pear-shape, this is known as the lightning rod effect. The lightning rod effect creates a separation between the center of charge from the center of mass which gives rise to electric dipole moments in octupole deformed nuclei [18]. Figure 2.13 shows a visualization of the lightning rod effect.

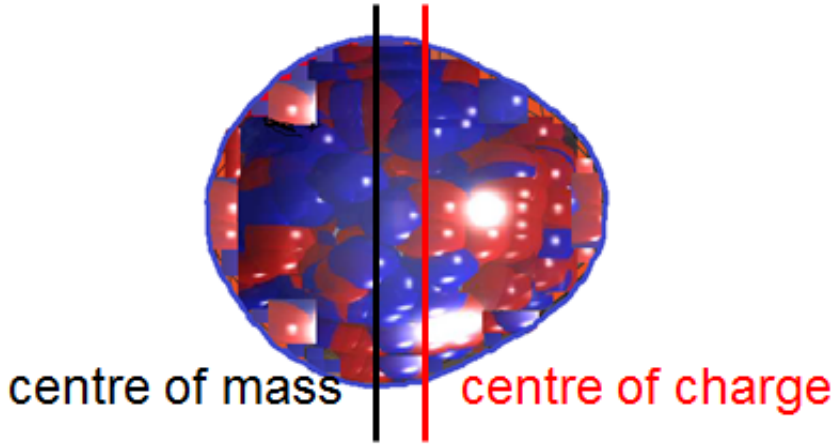

Figure 2.13: *An illustration of the lightning rod effect, the region between the two lines shows the separation between the center of mass and the center of charge. The red bubbles represent protons and the blue bubbles represent neutrons [18].*

In octupole vibrational bands, states of negative-parity are observed which at low spin, decay to the positive-parity state via $I^- \rightarrow (I-1)^+$ E1 transitions. In a static octupole deformation, the negative-parity states are interleaved with the positive-parity states, and the bands also decay through, $I^+ \rightarrow (I-1)^-$ E1 transitions. Thus, the E1 transitions will alternate between the two bands via, $I^+ \rightarrow (I-1)^-$ and $I^- \rightarrow (I-1)^+$ transitions [15–17, 24, 25]. Figure 2.14(a) shows the level scheme for an octupole vibrational Uranium-232 with the negative-parity states decaying through $I^- \rightarrow (I-1)^+$ E1 transitions, and figure 2.14(b) shows a static octupole nucleus, Thorium-226, with the negative-parity states decaying also through $I^+ \rightarrow (I-1)^-$ E1 transitions.

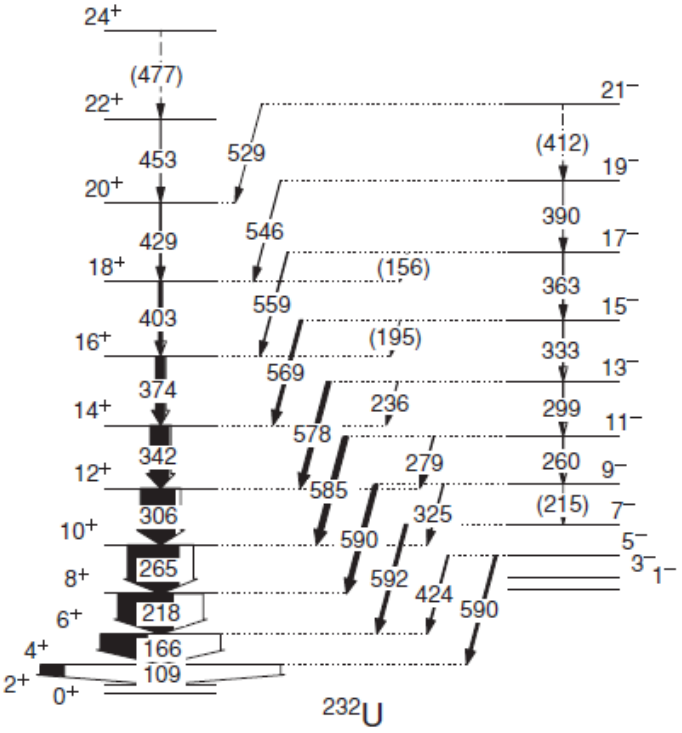

(a) *Level scheme for Uranium-232 showing E1 transitions connecting the negative-parity states to the positive-parity states [7]*

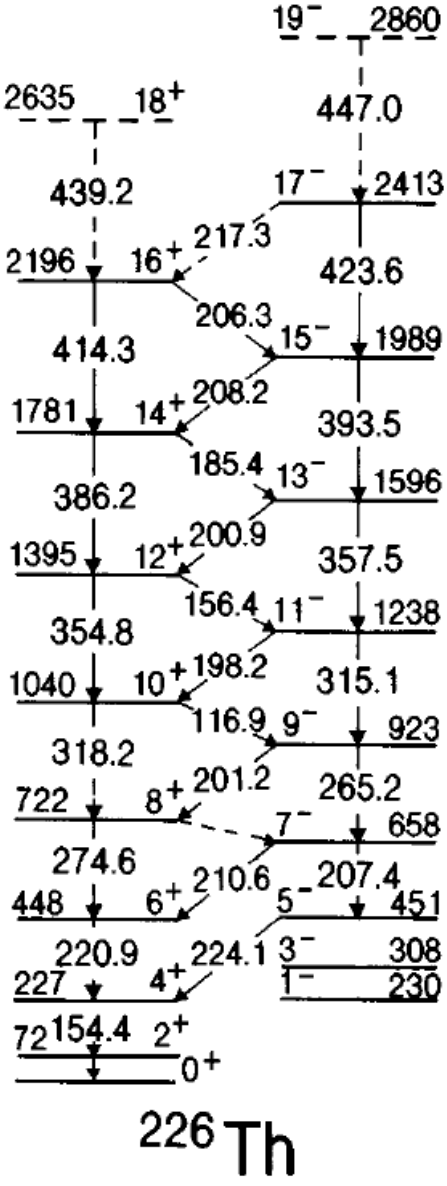

(b) *Level scheme for Thorium-226 showing alternating E1transitions connecting the negative-parity states and the positive-parity states. Level scheme taken from [13] (see also [6])*

Figure 2.14: *Level schemes showing E1 transitions connecting the negative-parity band to the positive-parity and vice versa in the case of Thorium-226 band.*

2.6.3 Branching ratios

The emission probability for E1 transitions is given by equation 2.10 with the reduced transition probability; $B(E1, I_i \rightarrow I_f)$ given by [13, 23]:

$$B(E1; I_i \rightarrow I_f) = \frac{3}{4\pi} D_0^2 \langle I_i 010 | I_f 0 \rangle^2 \tag{2.14}$$

The dipole moment D_0 can be determined experimentally from the ratio of the reduced E1 and E2 transition probabilities i.e, $B(E1)/B(E2)$, if the $B(E2)$ value is known. The ratio $B(E1)/B(E2)$ can be obtained from the relative intensities of the E2 to the E1 gamma-rays which is given by the branching ratio:

$$\lambda = \frac{T_2(E2)}{T_1(E1)} = \frac{i_{E2}}{i_{E1}} \tag{2.15}$$

where i_{E2} and i_{E1} are the gamma-ray intensities for E2 and E1 transitions, respectively. From equation 2.10, the reduced transition probabilities for E2 and E1 multipoles can be expressed by equation 2.16 and equation 2.17, respectively:

$$B(E2, I_i \rightarrow I_f) = \frac{1}{1.223 \times 10^9 E_{\gamma E2}^5} T(E2, I_i \rightarrow I_f) \tag{2.16}$$

$$B(E1, I_i \rightarrow I_f) = \frac{1}{1.578 \times 10^{15} E_{\gamma E1}^3} T(E1, I_i \rightarrow I_f) \tag{2.17}$$

Therefore, the branching ratio λ can be given by the expression:

$$\lambda = \frac{T_2(E2)}{T_1(E1)} = \frac{1.223 \times 10^9 B(E2) E_\gamma^5(E2)}{1.587 \times 10^{15} B(E1) E_\gamma^3(E1)} \tag{2.18}$$

and from equation 2.18 the ratio $B(E1)/B(E2)$ can be expressed as follows:

$$\frac{B(E1)}{B(E2)} = 7.7064 \times 10^{-7} \frac{E_\gamma^5(E2)}{E_\gamma^3(E1)} \frac{1}{\lambda} \tag{2.19}$$

2.7 Tetrahedral shapes

Another type of octupole deformation may exist in nuclei, which is the tetrahedral shape [3, 4]. A tetrahedral shape is a special case of an octupole deformation; it is a triaxial deformation defined by the coefficient α_{32} and the spherical harmonic Y_3^2. Figure 2.15 represents a nucleus having a tetrahedral shape with the arrows showing the three unequal axes x, y, and z. The nuclear radius of a tetrahedral shaped nucleus will be given by the equation 2.20. Note that, a tetrahedral shape is a pure octupole deformation, without any quadrupole deformation: i.e. it has $\alpha_{2\mu} = 0$

$$R(\theta, \phi) = R_0[1 + \alpha_{32} Y_3^2] \tag{2.20}$$

The tetrahedral shape is predicted to be stable around specific proton and neutron numbers [1, 3]. Figure 2.16 and figure 2.17 show the tetrahedral shell gaps corresponding to the proton and neutron numbers, respectively. These give rise to the regions on the nuclear chart, shown in figure 2.18, which should be favourable for the observation of tetrahedral states, including the mass 230 region. Potential energy surfaces for Uranium-230, and Thorium-232 as a function of α_{20}, and α_{32} coefficients, in figure 2.19, and figure 2.20 respectively show tetrahedral minima at $\alpha_{32} \approx 0.15$, and $\alpha_{20} = 0$ [4,26].

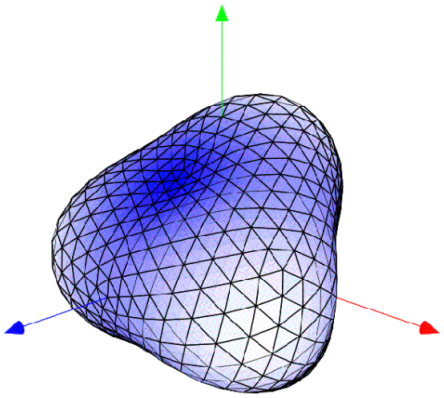

Figure 2.15: *A diagram how would a tetrahedral shape nucleus look like, the three different arrows show the non equal axes x,y and z.*

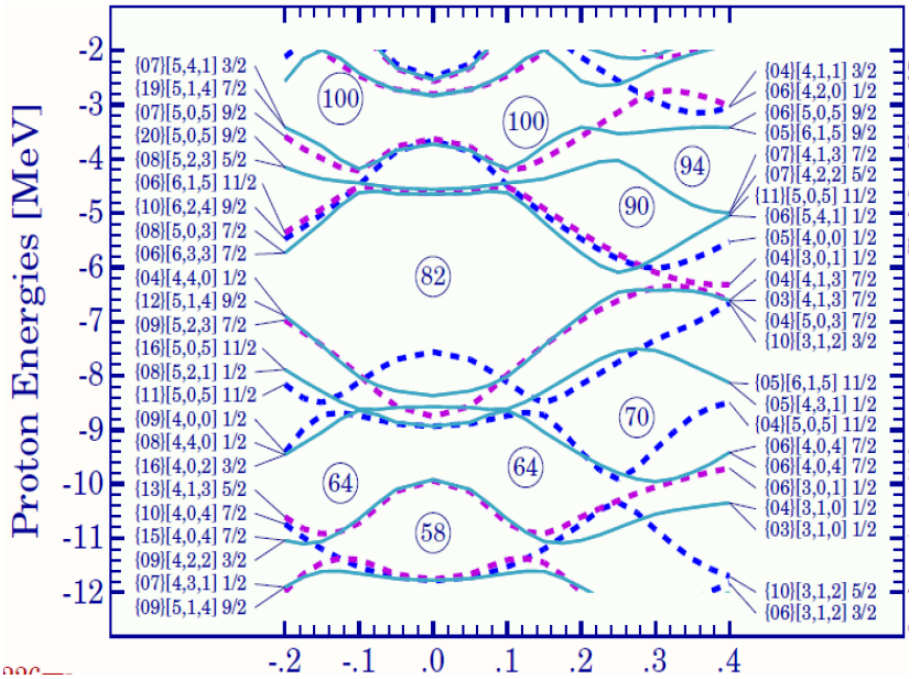

Figure 2.16: *Shell gaps for the protons numbers for a tetrahedral deformation [1].*

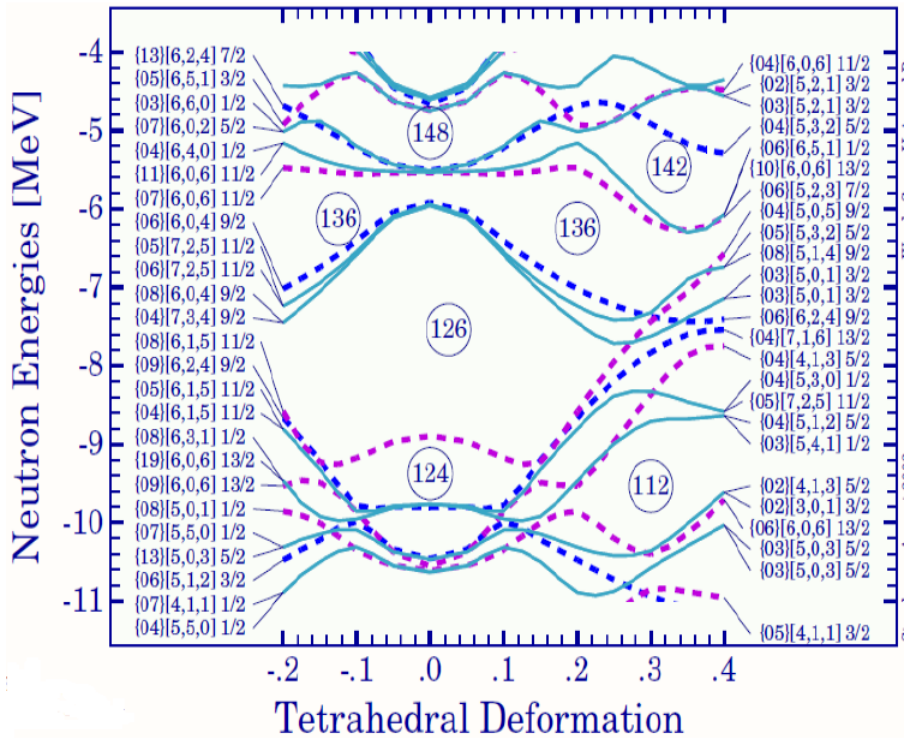

Figure 2.17: *Shell gaps for the neutron numbers for a tetrahedral deformation [1].*

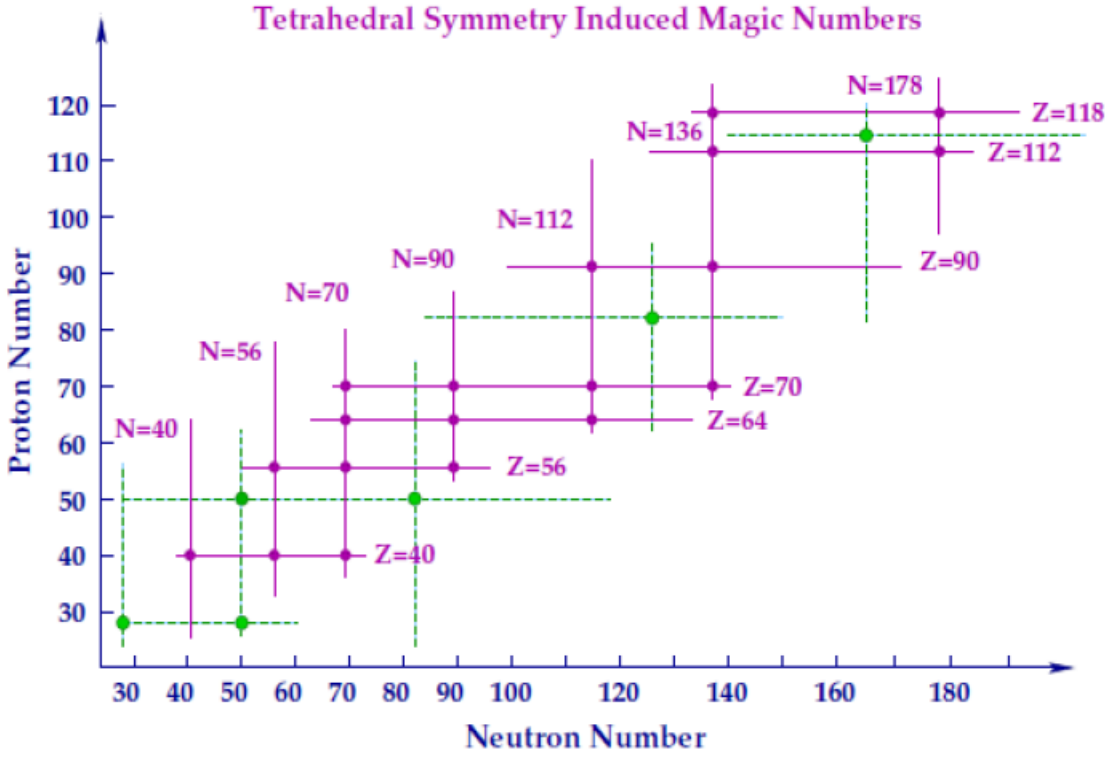

Figure 2.18: *The nuclear chart showing the predicted regions of tetrahedral shape. The purple lines indicate the tetrahedral shell closures and the green lines indicate the spherical shell closures [10].*

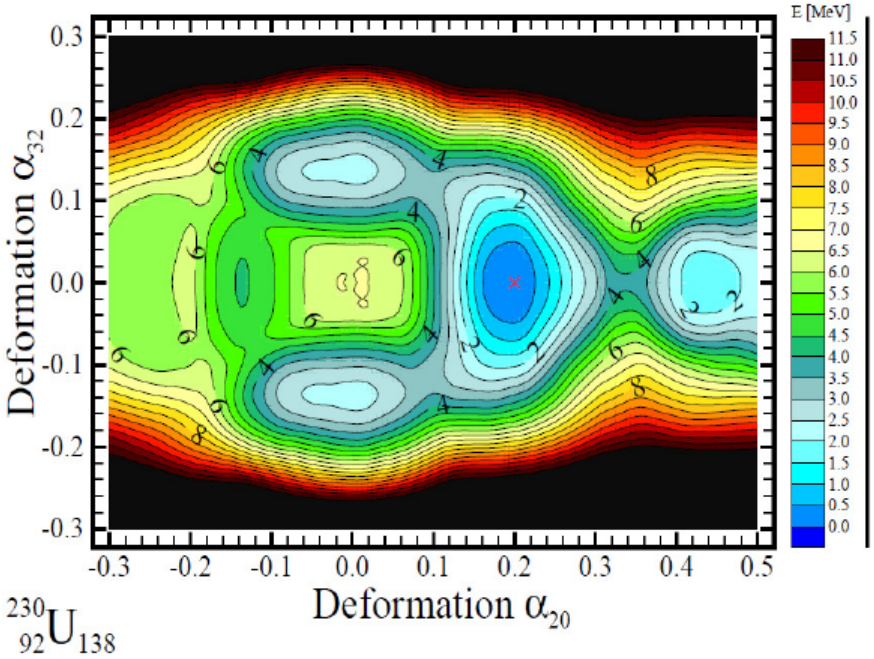

Figure 2.19: *Potential energy surface of Uranium-230 with a corresponding tetrahedral minimum at* $\alpha_{32} \approx 0.15$ *and* $\alpha_{20} = 0$ *[1].*

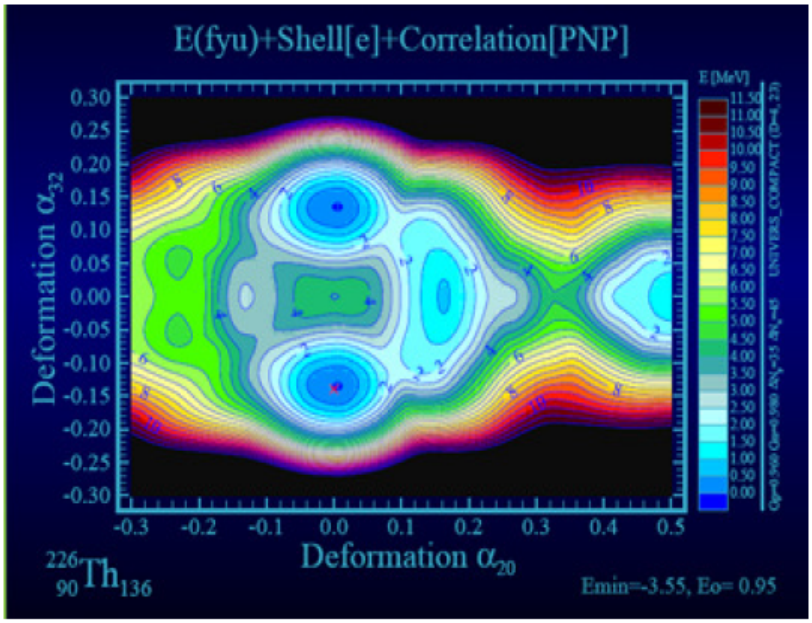

Figure 2.20: *Potential energy surface of Thorium-232 with a corresponding tetrahedral minimum at* $\alpha_{32} \approx 0.15$ *and* $\alpha_{20} = 0$ *[1].*

2.8 Tetrahedral bands

The tetrahedral shape is a pure octupole deformation, with no quadrupole moments (E2) (see equation 2.20). Therefore, for a rotating tetrahedral shape, no quadrupole radiation should be emitted. The first non-vanishing multipole moment is, $\lambda = 3$, and the expected multipole radiation should be of the octupole type (E3 transitions) [3, 14]. Therefore, a reliable indicator of a tetrahedral shape should be a rotational band connected by E3 transitions. However, due to the fact that for tetrahedral deformation, $\alpha_{2\mu}$ is equal to zero, rotational bands lacking quadrupole transitions have been considered to be a signature of tetrahedral shape.

It turns out that, there is another more possibility besides a tetrahedral deformation, that could explain missing E2 transitions; it is the relative intensities of the in-band E2 transitions to the inter-band E1 transitions. The relative intensities of the in-band E2 transitions to the inter-band E1 transitions can be given by:

$$\frac{i(E2)}{i(E1)} = \frac{E_\gamma^5(E2)}{E_\gamma^3(E1)} \frac{B(E2)}{B(E1)} \tag{2.21}$$

A lack of in-band E2 transitions implies that the ratio $i(E2)/i(E1)$ is approximately or equal to zero. This ratio can be zero if the $B(E2) = 0$ (tetrahedral case), or approximately zero if $E_\gamma^3(E1) \gg E_\gamma^5(E2)$ (octupole vibrational case) [27,28] where inter-band E1 transitions between the positive-parity states and the negative-parity states, compete with the in-band E2 transitions from the negative-parity states. The inter-band E1 transitions will take intensity from the in-band E2 transitions. Therefore, the states from the negative-parity band may prefer to decay via the inter-band E1 transitions which will result in a lack of in-band E2 transitions being observed within the negative-parity band. Figure 2.21 shows the level scheme for ^{230}U. Now a question directed to ^{230}U is; are the missing in-band E2 transitions in the low-lying negative-parity states because the reduced transition probabilities are equal to zero, which implies to the tetrahedral symmetry, or, alternatively is it because the inter-band E1 transitions are very large, which implies to an octupole vibration.

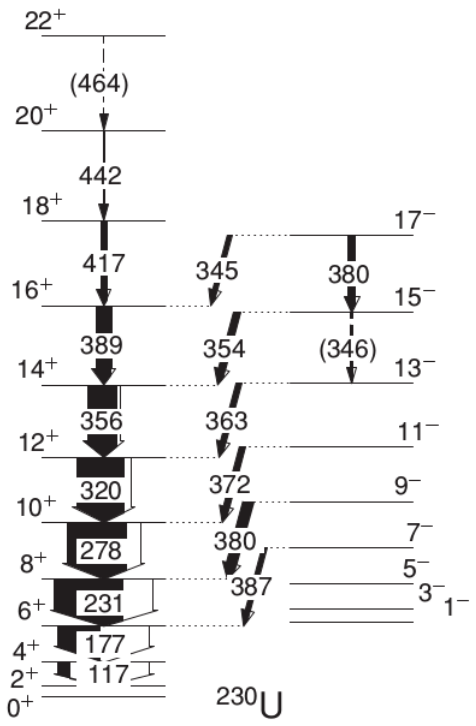

Figure 2.21: *Level scheme for ^{230}U showing the lack of E2 transitions between the low-lying negative-parity states [7].*

Chapter 3

Experimental Methods

Chapter 2 explored the theoretical framework of the study. The focus of the current chapter is on experimental methods covering the nuclear reaction, beam energy and target, AFRODITE gamma-ray detecting array, recoil detector, recoil detector's principle of operation, data acquisition system and electronics, and data acquisition system set up.

3.1 Nuclear reaction

At iThemba LABS, heavy nuclei such as uranium can be produced at high excitation energies by bombarding a heavy target nucleus with a lighter nucleus as a projectile. For this study, the experiment was performed with the nuclear reaction: ^{232}Th(α, 6n)^{230}U. Figure 3.1 shows a diagram of how a target nucleus interacts with a projectile nucleus in the process of a compound nuclear reaction. The first step shown in figure 3.1 is fusion. The projectile fuses with the target and forms a compound nucleus. The compound nucleus idea was put forward by Niels Bohr in 1936 [29]. For the projectile to fuse with the target it must have energy greater than the Coulomb barrier between the target and itself. The energy of the Coulomb barrier is given by the equation:

$$V_c = \frac{e^2}{4\pi\epsilon_0}\frac{Z_t Z_p}{R_t + R_p} \tag{3.1}$$

where e is the elementary charge, Z_t and Z_p are the atomic numbers of the target and the projectile respectively, R_t and R_p are the radii of the target and the projectile respectively, and $4\pi\epsilon_0$ is a natural

constant. When the projectile fuses with the target, the energy and momentum of the projectile are transferred into the nucleons of the target. The compound nucleus is formed in an excited state. The excitation energy of the compound nucleus is given by the equation 3.2:

$$E^* = \left[\frac{A_t}{A_{cn}}\right] E_p + Q \tag{3.2}$$

where A_t and A_{cn} are the atomic masses of the target and the compound nucleus respectively, and E_p is the energy of the projectile. The Q-value of the reaction is given by the expression:

$$Q = \Delta m c^2 \tag{3.3}$$

Here c is the speed of light, and Δm is defined as the mass defect; the difference between the masses of the initial and final states:

$$\Delta m = \sum m_{initial} - \sum m_{final} \tag{3.4}$$

The compound nucleus in the excited state has excess energy, and high angular momentum (it spins rapidly). Depending on the amount of excess energy and how close the compound nucleus is to the stability line, it can decay either by the evaporation of particles, or by fission if it is a very heavy nucleus, see step two in figure 3.1.

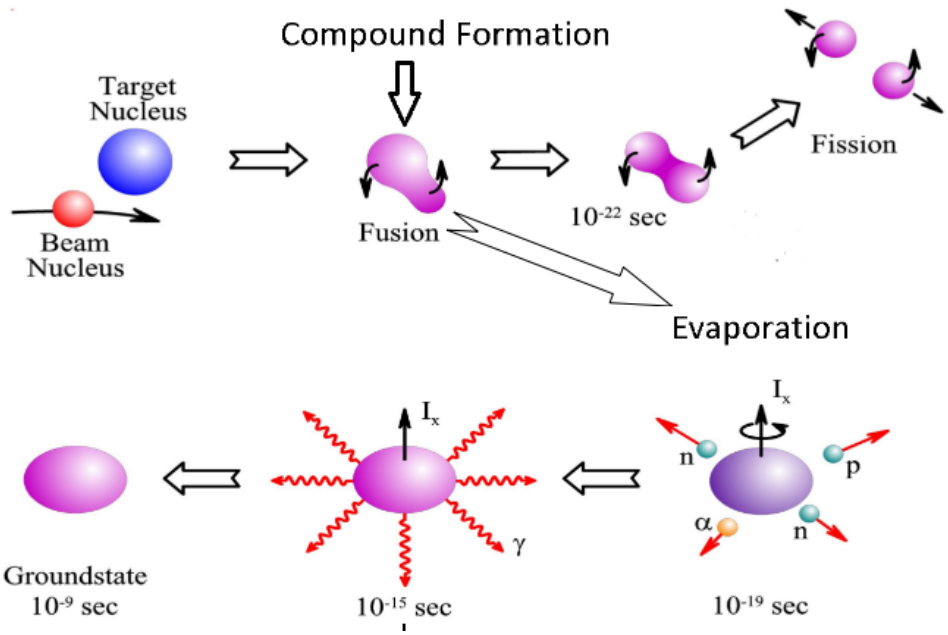

Figure 3.1: *A schematic representation of how a target nucleus interacts with a projectile nucleus and the different stages involved in a nuclear reaction [30].*

3.1.1 Fission

The fission process can be explained by adopting the liquid drop model. Heavy nuclei within the uranium mass region have many protons packed in the nucleus. These particles suffer from Coulomb repulsion. These repulsions weaken the binding energy per nucleon for the nucleus. This makes the nucleus unstable and decays by splitting into two fragments. Such a decay is called fission.

During the fission process, the nucleus elongates, it then elongates even further, until it reaches a scission point, where it breaks into two fragments. The two fragments fly-away opposite to each other with approximately 100 MeV of kinetic energy each. Thereafter they release internal energy through β-decay and gamma-ray emission. Figure 3.2 shows a typical diagram representing the fission process. The difference between the energy a nucleus would release during fission and the Coloumb barrier determines the height of the fission barrier. The height of the fission barrier and lifetime depends on the ratio Z^2/A. For spontaneous fission, the height of the fission barrier is zero and the ratio $Z^2/A > 47$ [22].

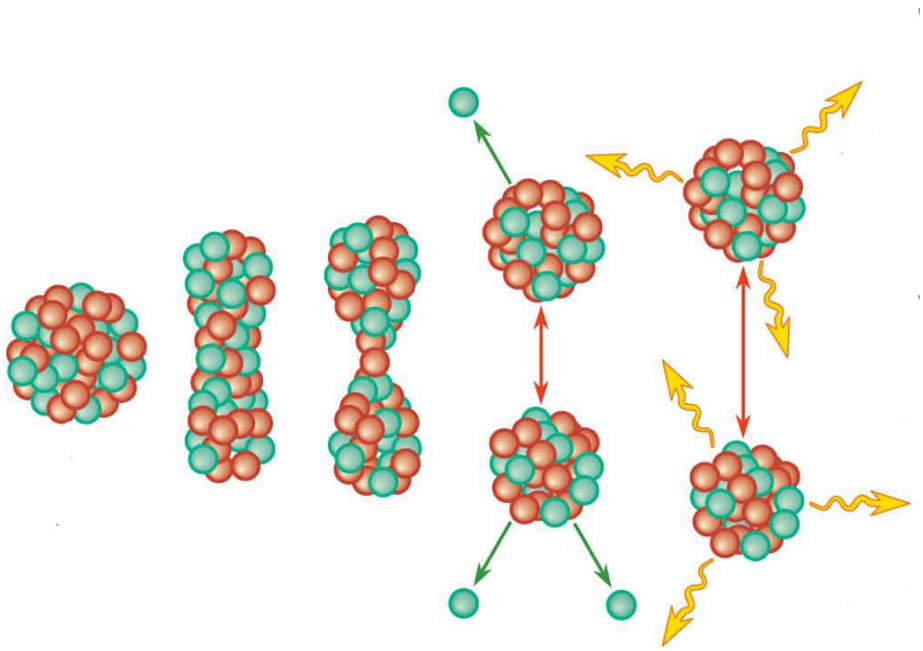

Figure 3.2: *A diagram showing the different stages a compound nucleus undergo during fission, the two fragments decay by first emitting particles and lastly by emitting gamma-rays* [31].

3.1.2 Evaporation

If the compound nucleus survives fission, it will decay through emitting particles such as neutrons, protons, and alphas. Neutrons are the first to be emitted; they have high emission probability compared to charged particles such as protons and alphas, which must overcome a Coulomb barrier. What remains after the particle emission is what is called a fusion-evaporation residue. The fusion-evaporation residue has insufficient energy to further emit particles. Therefore, it decays to the ground state by emitting gamma rays and conversion electrons. A schematic representation of the decaying of a compound nucleus from high energy and angular momentum states to lower energy and lower angular momentum states is shown in figure 3.3. The stage of gamma ray emission is the targeted stage of the reaction during the experiment. The gamma rays carry the information needed to study the particular nucleus of interest, which in this case is Uranium-230.

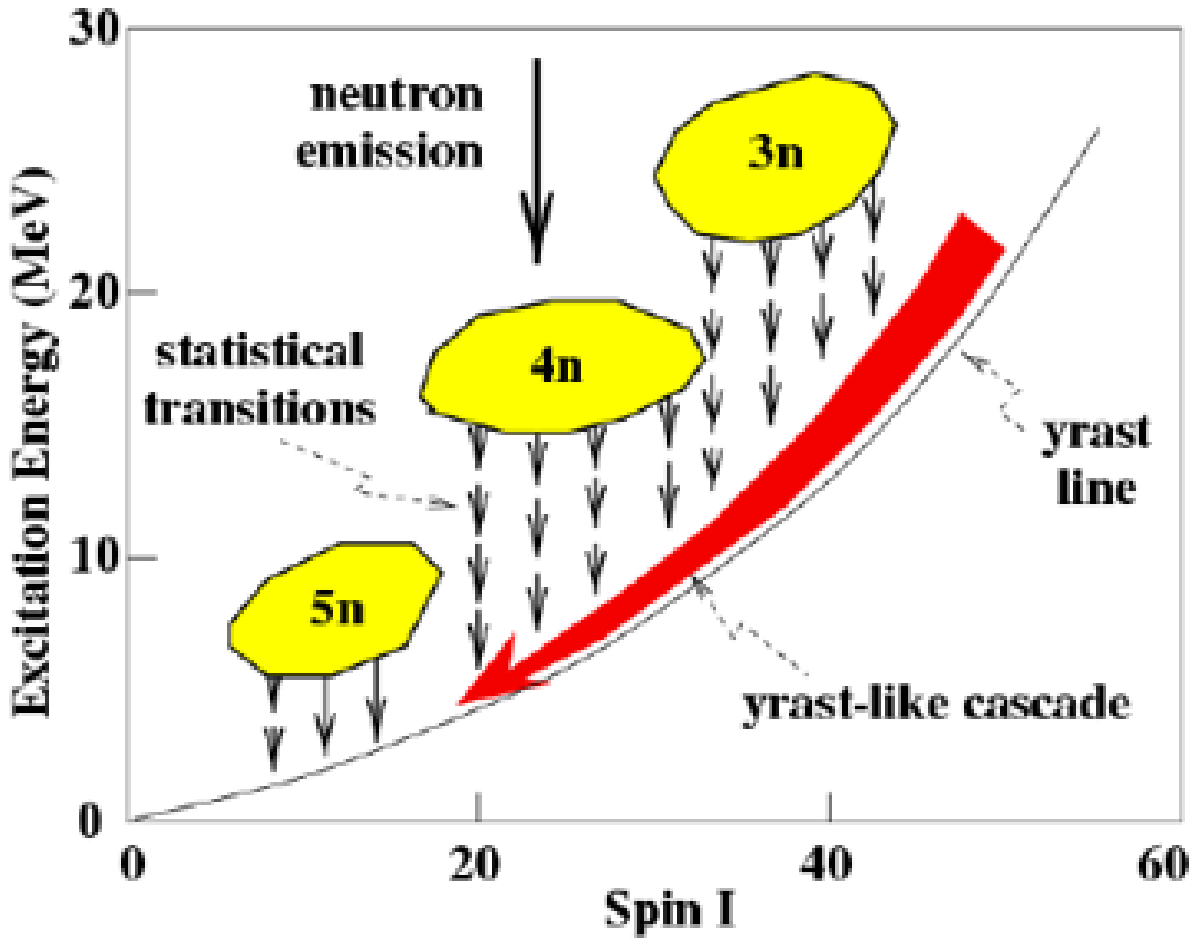

Figure 3.3: *A diagram representing the decaying of the compound nucleus from higher energy and higher angular momentum state ground-state [32].*

3.2 Beam energy

For the reaction performed in this experiment, the Thorium-232 target is a heavy nucleus and fission is expected. This is the challenge in studying the nucleus, particularly in producing it. A plot of the reaction cross-section is shown in figure 3.4. It was calculated using a Monte Carlo simulation; PACE4 (Projected Angular Momentum Coupled Evaporation) [33, 34]. The blue dots show experimental excitation functions for Uranium-230. This plot also aided in selecting the beam energy for the reaction. The plot shows that the beam energy for optimum cross-section for the reaction, ^{232}Th(α, 6n)^{230}U, ranges from between 60 to 65 MeV. A 63 MeV beam energy was selected for the experiment. The beam was provided by the accelerator group at iThemba LABS using the Separated Sector Cyclotron (SSC) facility. The target thickness used in this experiment was calculated with a Monte Carlo code, SRIM (Stopping and Range of Ions in Matter) [35]. The best target thickness allowing recoils to escape from the target was calculated to be 100 μg/cm^2.

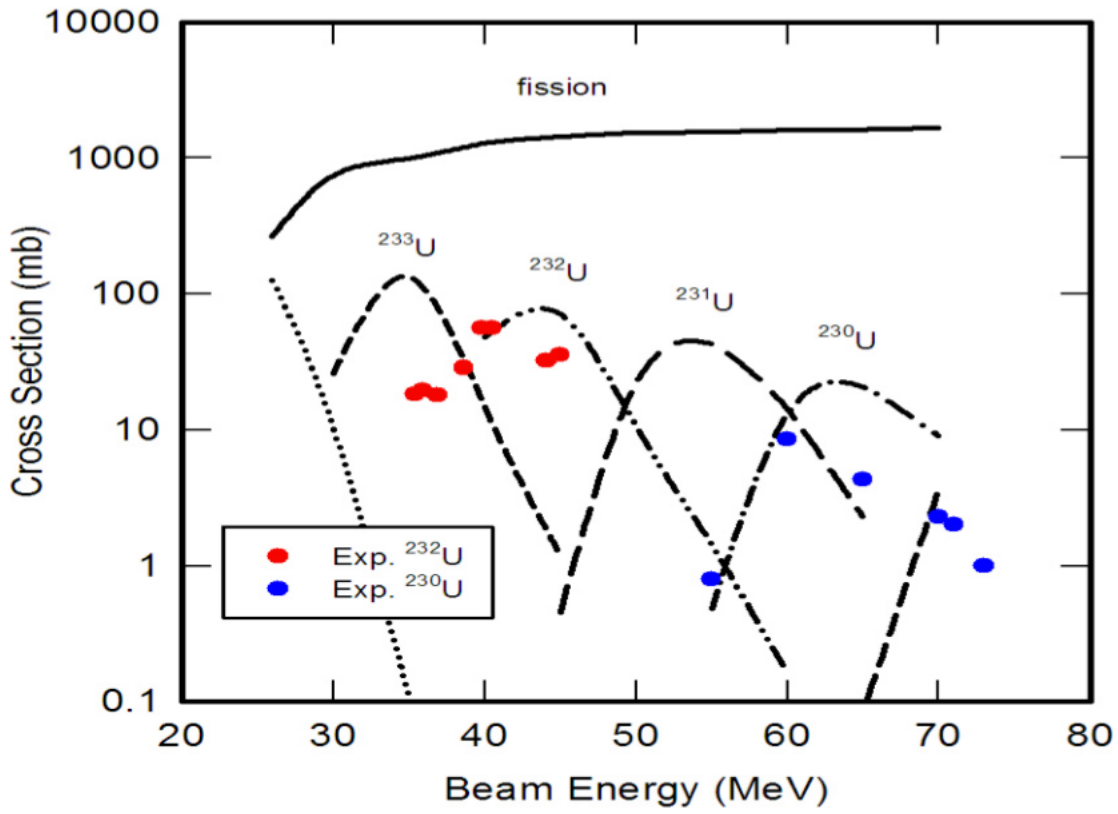

Figure 3.4: *Plot of cross-section vs beam energy for* ^{232}*Th(α,xn) reaction. Data for the plot is obtained from a PACE4 simulation [10].*

3.3 AFRODITE

The experiment was carried out with the AFRODITE (AFrican Omnipurpose Detector for Innovative Techniques and Experiments) array at iThemba LABS. The experiment was performed with the array having twelve High Purity Germanium (HPGe) detectors positioned at angles 90° and 135° of the array. A photograph of the AFRODITE array with the mounted clover detectors is shown in figure 3.5. For this work, AFRODITE was coupled with a recoil detector. The two faces of the support frame of the array at 0° and 180° with respect to the incoming beam direction were occupied by the beam pipe and the recoil detector chamber. The operation of the Recoil detector is explained in section 3.4.

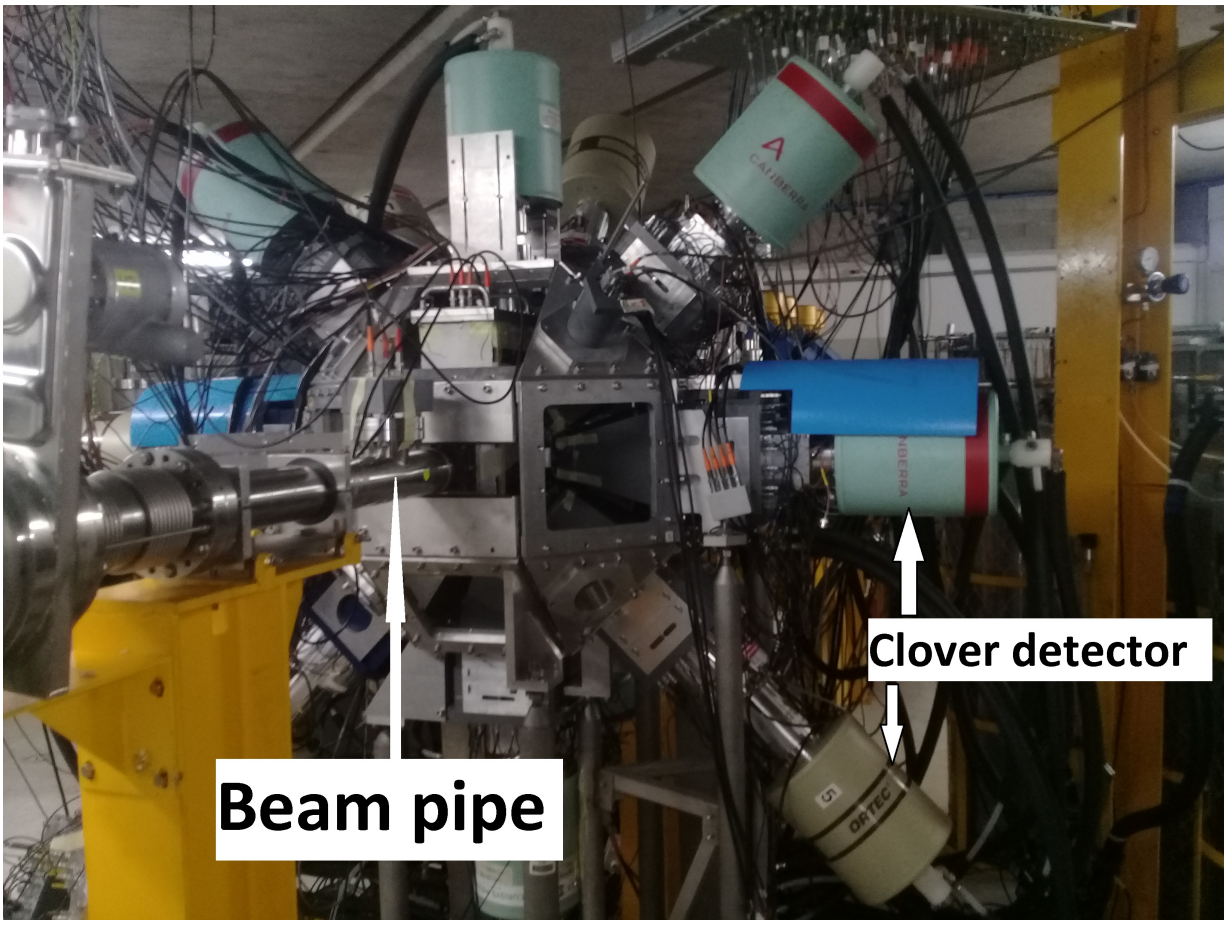

Figure 3.5: *A photograph showing an array of germanium detectors at iThemba LABS. Photograph taken at AFRODITE.*

At the center of the AFRODITE array, there is a target chamber which houses the target. The target is attached on a target frame, which is then inserted in the chamber. The target chamber is shown inside the open AFRODITE array in figure 3.6. During the experiment, the array was closed, surrounding the target chamber with every detector at 196 mm from the target.

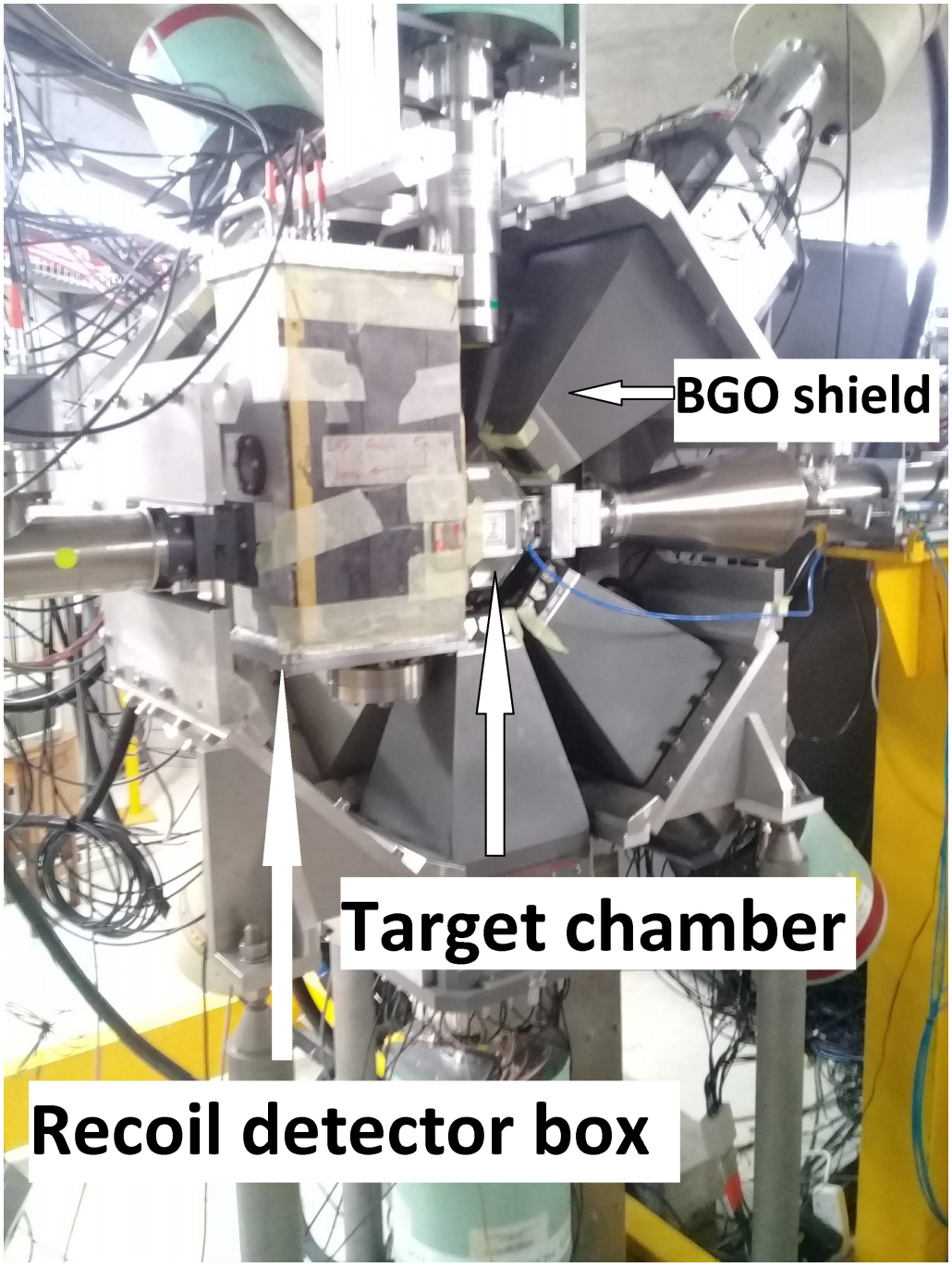

Figure 3.6: *A photograph showing an open array of germanium detectors with the target chamber at the center. Photograph taken at AFRODITE.*

3.3.1 Germanium Detectors

The detectors consist of a germanium (Ge) crystal with a p-region and an n-region. Between these two regions is what is called a depletion region. The depletion region determines the active volume of the detector. Detectors with a larger depletion region hence larger active volume have higher efficiency for gamma-ray spectroscopy. A reverse bias voltage can be applied to the detector to maximize the width of the depletion region. The width of the depletion region is defined by [36]:

$$d = \left[\frac{2\epsilon V}{eN}\right]^{1/2} \tag{3.5}$$

where V is the reverse bias voltage, and N is the impurity concentration in the Ge crystal. To improve the depletion region's width to few centimeters, the impurity concetration in the crystal is reduced down to 10^{10} atoms/cm^3. When a gamma-ray hits the crystal it creates an electron-hole pair in the depletion region, see figure 3.7. The detector is supplied with a high voltage (HV) to create an electric field between the depletion region to accelerate the electron-hole pairs towards the p-region and the n-region. The detector consists of an electrode to measure the magnitude of the charge carried by the electron-hole pair, the charge is proportional to the energy of the gamma-ray that created it.

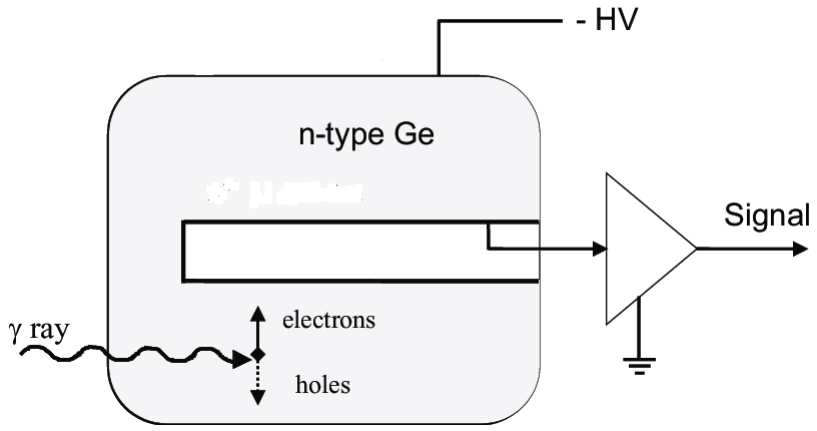

Figure 3.7: *A diagram showing a gamma-ray interacting with an n-type germanium detector. Electrons from the electron-hole pair are accelerated towards the electrode by the high negative voltage(-HV).*

The detectors are kept or operated at low temperatures because of their low band gap. The low-temperature operation reduces the reverse leakage current as this may bring in electric noise which can ruin the detector's energy resolution. Liquid Nitrogen (LN_2) is used as a cooling agent for the detectors; it has a temperature of -196 degrees Celsius (77 kelvin), this is low enough to maintain the detectors at optimum performance.

3.3.2 Clover detector

Each clover detectors consists of four n-type coaxial Ge crystals that are shaped and arranged like a four-leaf clover, which is how the name "clover detector" is derived [37]. The clover detectors were employed to detect and measure the gamma-ray energies during the experiment. Each gamma-ray can interact with the detector by one of the three different processes; Photo-electric effect, Pair production, and Compton scattering. In the photo-electric effect, the gamma-ray hits and deposits all of its energy on one crystal. In pair production, an electron and a positron annhilate and generate two gamma-rays that are detected by the detector. In Compton scattering, the gamma-ray hits a crystal, deposits a fraction of its energy when it scatters. If it scatters out of the crystal into another crystal where it deposits the remaining energy, the total energy of the gamma-ray can be recovered by adding the fraction of energy deposited to the first crystal to the fraction of the energy deposited to the second crystal. This addback method increases the photo-peak effiency of the detector. A photograph of a clover detector is shown in figure 3.8. A schematic representation with dimensions of the crystals of the clover detector is shown in figure 3.9, the spacing between any two adjacent crystals is 0.2 mm.

Specification of a clover detector

Clover detectors have an excellent energy resolution, and achieve a large peak-to-total (P/T) ratio by surrounding the detector with a bismuth germanate shield (BGO) which reduces the background detected by the germanium detector [38]. The energy resolution for each crystal, for high energy gamma-rays of 1.33 MeV can be good as 2.1 keV, and for low energy gamma-rays of 122 keV, 1.1 keV (full width at half maximum (FWHM)). These features and the following ones make the clover detector an essential and effective tool for gamma-ray spectroscopy. The other features are [38, 39]:

- High absorption efficiency.
- Excellent timing response.
- Good sensitivity to gamma rays.
- Distance between crystal surface and the target position $D_{tp} = 196$ mm.
- Distance between detector end-cap and crystal surface $D_{ec} = 20$ mm.
- Total opening angle $\Theta = 23.2^{o}$.
- Solid angle per detector $\Omega_{Ge} = 1.34\%$ of 4π (for a 0.2 mm distance between crystals).
- Photo-peak efficiency (for 1.33 MeV): $\epsilon_{ph}\ \Omega_{Ge} = 17.8{\times}10^{-4}$.
- Peak-to-total ratio (P/T) for 1.33 MeV$_{Ge}$ with suppression = 0.50.
- Add-back factor (for 1.33 MeV): 1.56.

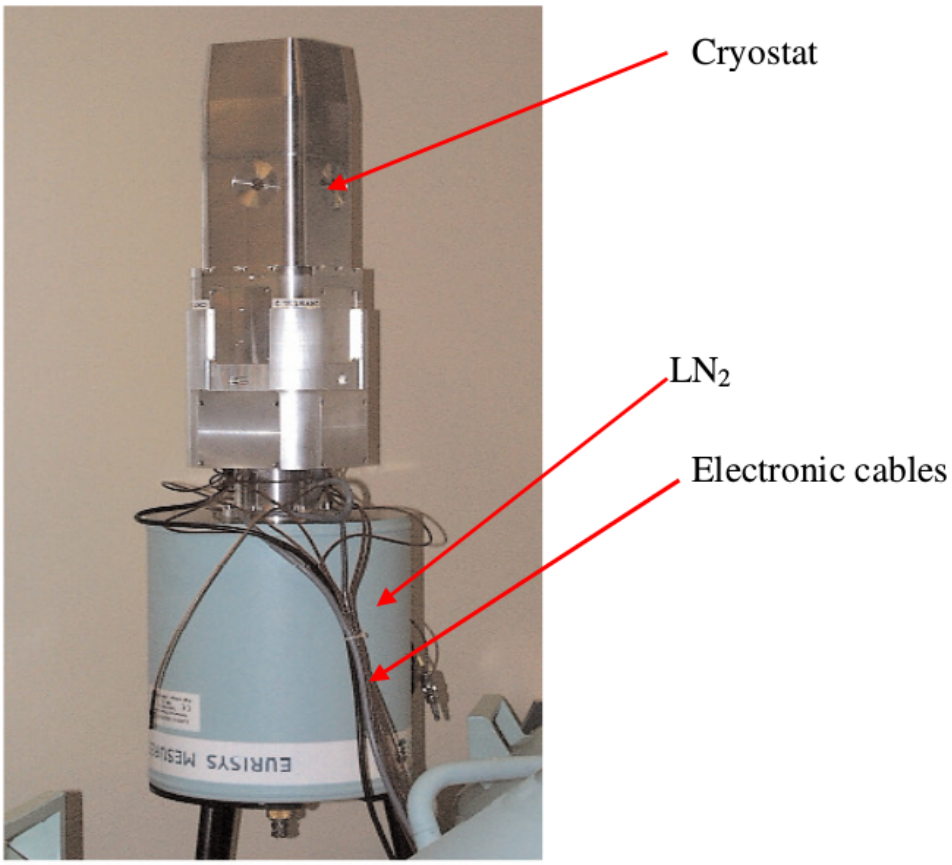

Figure 3.8: *Photograph of a CLOVER detector, showing the cryostat, the liquid nitrogen (LN_2) dewar and the electronics cable. Photograph taken from AFRODITE.*

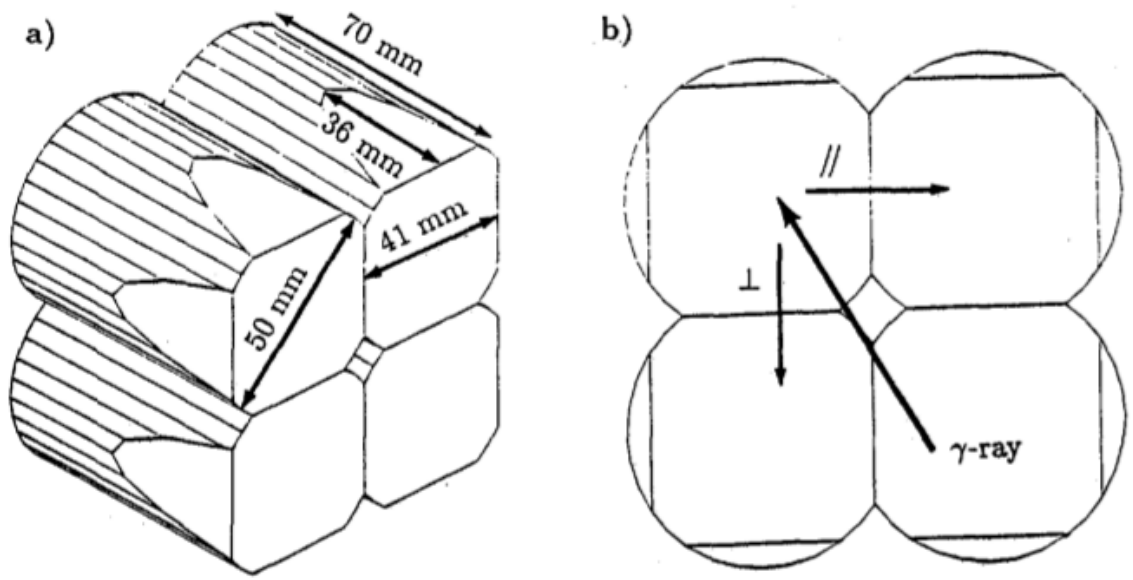

Figure 3.9: *Schematic view of the Clover detector. Crystal sizes are given in (a). In (b), the upper left crystal is used as a scatterer segment. The vertical (X.) and horizontal (⊥) coincidences with the adjacent segments are also show [38].*

3.4 Recoil Detector

Fission dominates in the nuclear reaction ^{232}Th + ^{4}He. AFRODITE alone was insufficient for the detection of gamma rays from the Uranium evaporation-residues as they are mostly concealed by the gamma-rays from fission. To circumvent this problem, AFRODITE was coupled with a recoil detector. Figure 3.6 shows the recoil detector box positioned in the AFRODITE beam line, behind the target chamber. Figure 3.10, shows different views of the recoil detector chamber mounted on the AFRODITE beam line. The Recoil detector suppresses the fission gamma-rays obscuring the evaporation-residues. In figure 3.11, two spectra from a previous study that used the recoil detector for the nuclear reaction ^{232}Th + ^{4}He at 42 MeV, are compared. In figure 3.11, spectrum (a) was obtained with AFRODITE alone, and spectrum (b) was obtained with AFRODITE coupled with the recoil detector. In spectrum (a), no peaks are visible corresponding to Uranium-232 evaporation-residues. The peaks are swamped by the fission gamma-rays, and by the high background with the strong 511 keV peak. In spectrum (b), the fission background has been suppressed by the recoil detector. This is evident from the dissapearance of the 511 keV peak and the appearance of peaks corresponding to Uranium-232 evaporation-residues. This clearly shows how significant the

recoil detector is in reducing the background for this type of nuclear reactions. Without the Recoil detector, it was going to be like searching for a needle in a haystack.

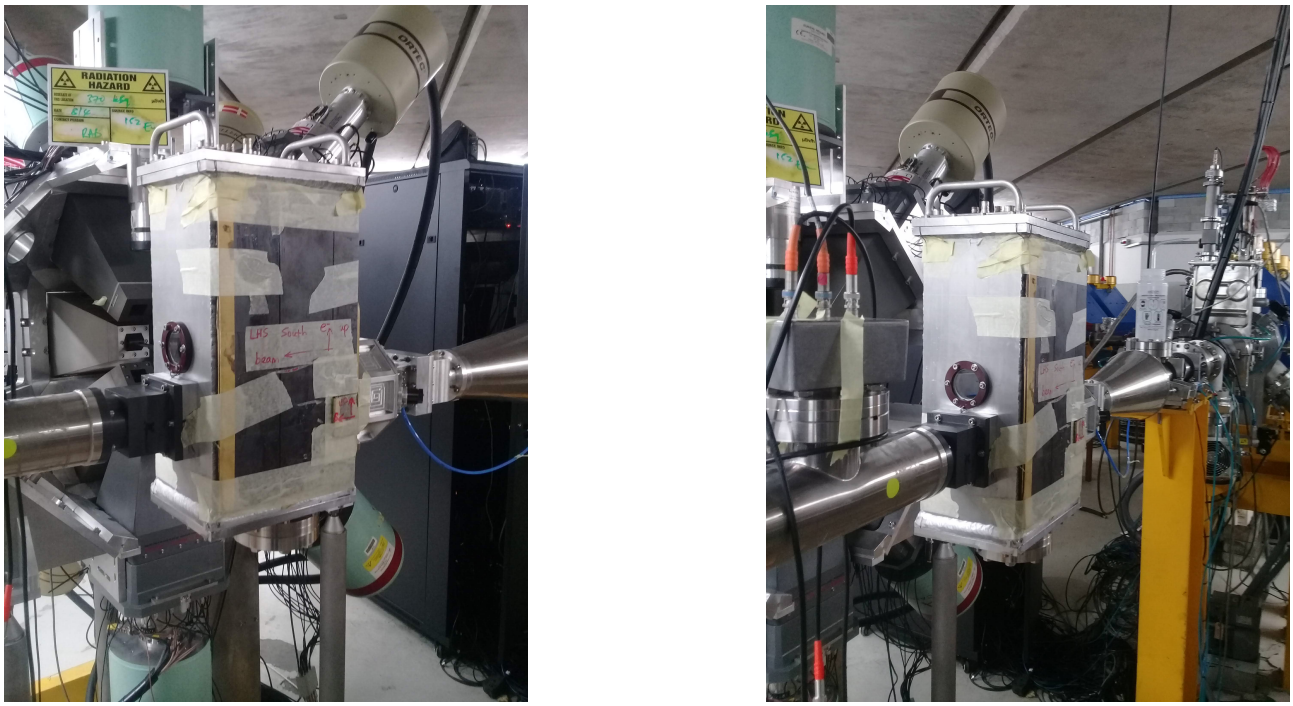

(a) *The side view of the recoil detector.* (b) *The back view of the recoil detector.*

Figure 3.10: *Different views of the recoil detector positioned on the AFRODITE beam line, photographs taken from AFRODITE.*

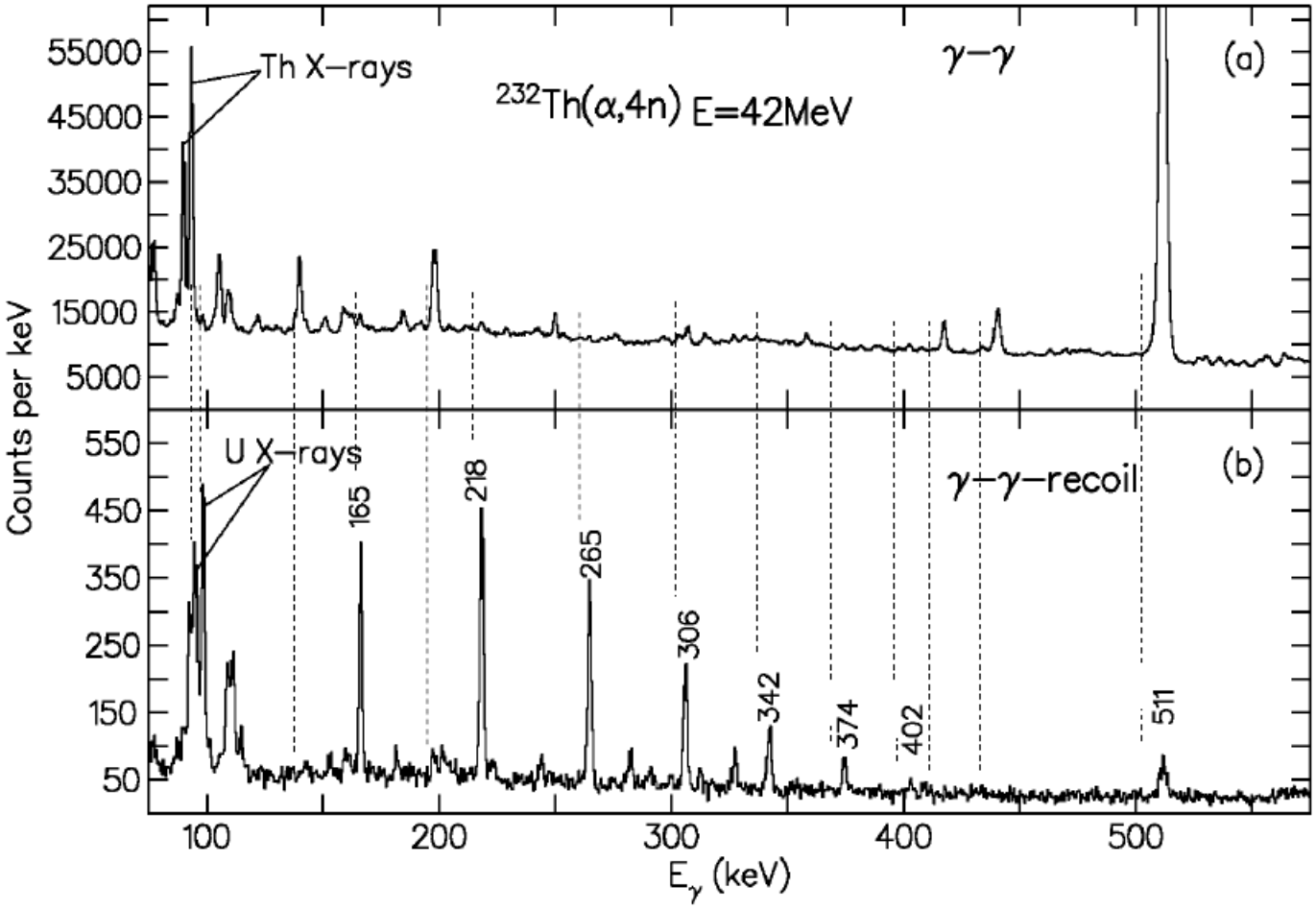

Figure 3.11: *Projection gamma ray spectra for Uranium-232 obatined with AFRODITE only (a) and with AFRODITE + recoil detector [10]* .

3.5 Recoil detector's principle of operation

The recoil detector is positioned behind target. When the beam hits the target, recoils and fission fragments are produced. These products reach the recoil detector at different times. The recoil detector consists of a thin foil of mylar coated with aluminium, and a Micro Channel Plate (MCP). The foil has a hole to allow the beam to pass through. Figure 3.12 shows a schematic front view, and side view of the recoil detector. Figure 3.13 shows a photograph of the recoil detector. When the reaction products, fission fragments, recoils, and scattered alphas from the beam hit the foil, electrons are released. A negative voltage is supplied to the foil, and the electrons are accelerated away from the foil by the electric field, and directed towards the MCP by a dipole magnetic field. Magnets were put on the sides of the recoil detector box to produce the magnetic field. The electrons are detected, and multiplied in the MCP and converted into an electric signal. The signal's amplitude, and the

time of detection, confirms which product has hit the foil. The number of electrons released from the foil is proportional to the specific energy loss - dE/dx of the product hitting the foil. The specific energy loss from the products is proportional to Z^2 [36]. Therefore, the alphas from the beam will produce few electrons due to low Z, compared to the recoils, and fission products that have high Z. This means there is some differentiation between the signals of the alphas, and recoils and the fission fragments using the signal amplitude. For the detailed design and assembling of the recoil detector used in this thesis work, see reference [10].

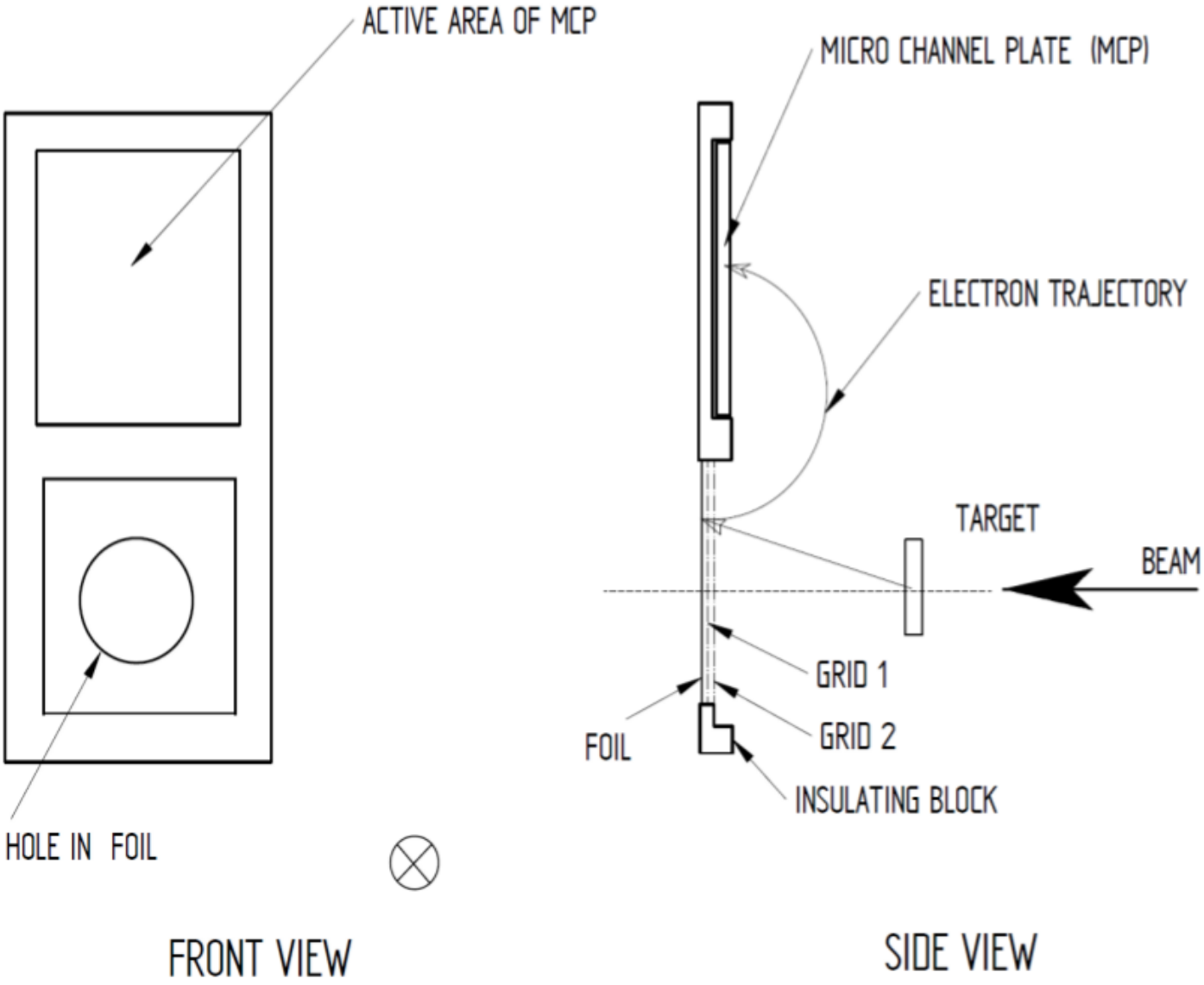

Figure 3.12: *The schematic front view and side view of the inside of the recoil detector* [7].

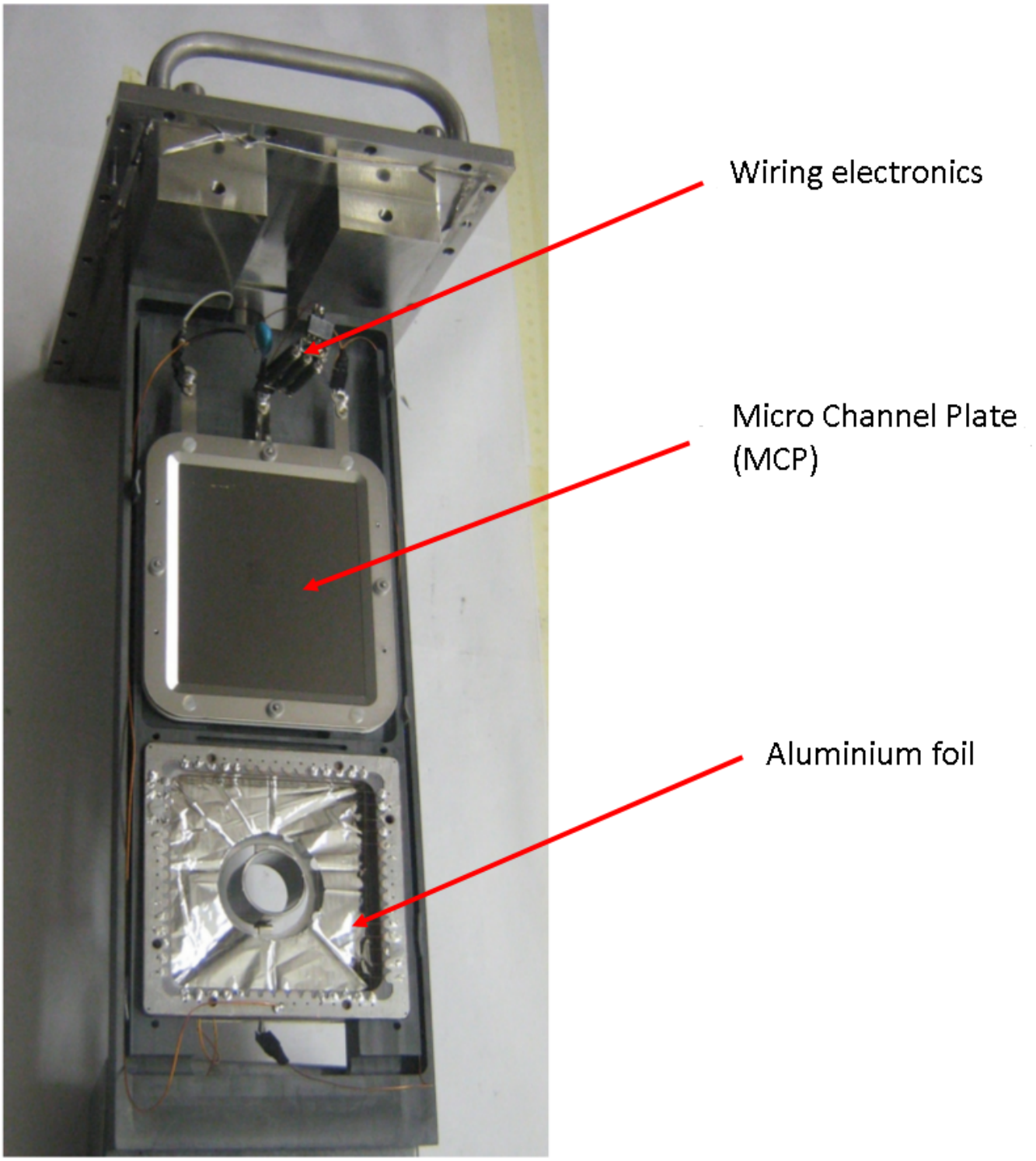

Figure 3.13: *A picture of the inside of the recoil detector, showing the MCP and the Al foil with a hole at the center.*

3.5.1 Time-of-flight method

The recoils and fission fragments have comparable signal amplitudes, but a time-of-flight method is effective in differentiating between them. Likewise, the reaction products and the alphas have different energies, and different velocities, so they reach the recoil detector at different times. The reaction, ^{232}Th(α, 6n), produces recoiling ^{230}U nuclei with a kinetic energy of about 1 MeV, and a speed of v/c $\sim$ 0.3%. The fission fragments have a kinetic energy of about 100 MeV, and a speed of v/c $\sim$ 5%, while the alphas have 63 MeV traveling at v/c $\sim$ 19%. With the target placed at a distance of 145 mm away from the foil, the time it takes the different particles to reach the foil are about 150 ns for ^{230}U, 10 ns for the fission fragments, and 3 ns for the alphas from the scattered beam. With this time-of-flight method, the recoils can be separated from the fission fragments.

3.5.2 Micro Channel Plate

A Micro Channel Plate (MCP) is a device that operates in a similar way to a photo-multiplier tube. The MCP consists of many small tubes called channels which are arranged into a honeycomb-like structure [40]. Figure 3.14 shows a schematic diagram of an MCP and a side view of a channel showing its principle of operation. A voltage V_D is applied at the ends of every channel, thereby creating an electric field across the channels. When charged particles, like electrons in this case, enter the channel, they are accelerated by the electric field towards the other end where they will be detected and converted into an electric signal. The electrons move in a zigzag path inside the channels hitting the walls of the channels and releasing secondary electrons. The secondary electrons will further release other secondary electrons; this is repeated up to the end of the channel. The avalanche electrons at the end of each channel are converted into a voltage signal, which is displayed as the output of the MCP on an oscilloscope. The MCP can detect about 10^7 electrons per second. With this rate limitation, continuous hitting of the foil with the beam will saturate the MCP. Therefore, the hole in the foil was made to allow the beam to pass through without hitting it. Figure 3.15 shows the dimensions of the MCP used for the recoil detector. Its physical and electrical specifications are listed in table 3.1.

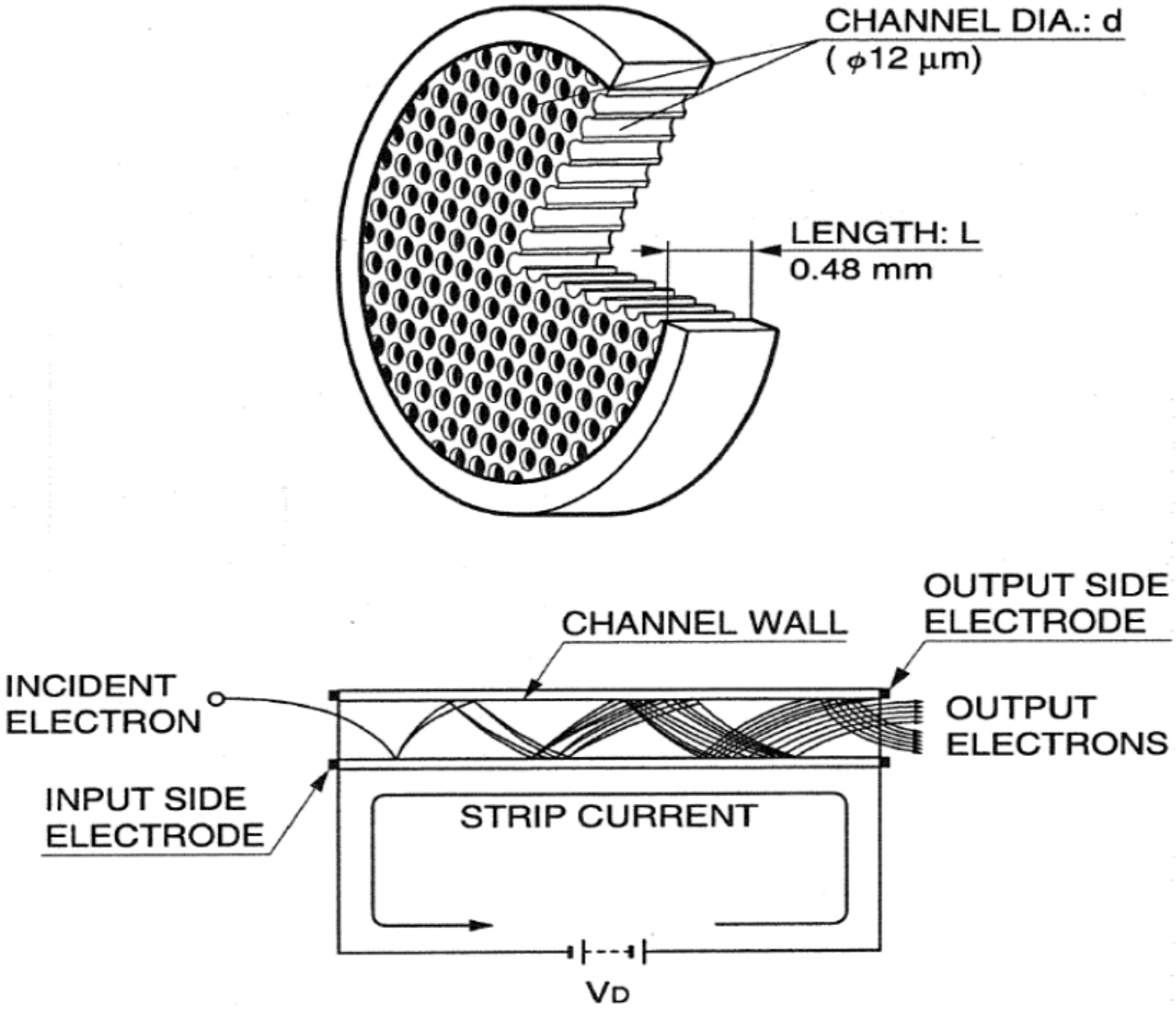

Figure 3.14: *Schematic construction showing channels of the MCP (upper portion) and operating principle of a single channel (lower portion) [10].*

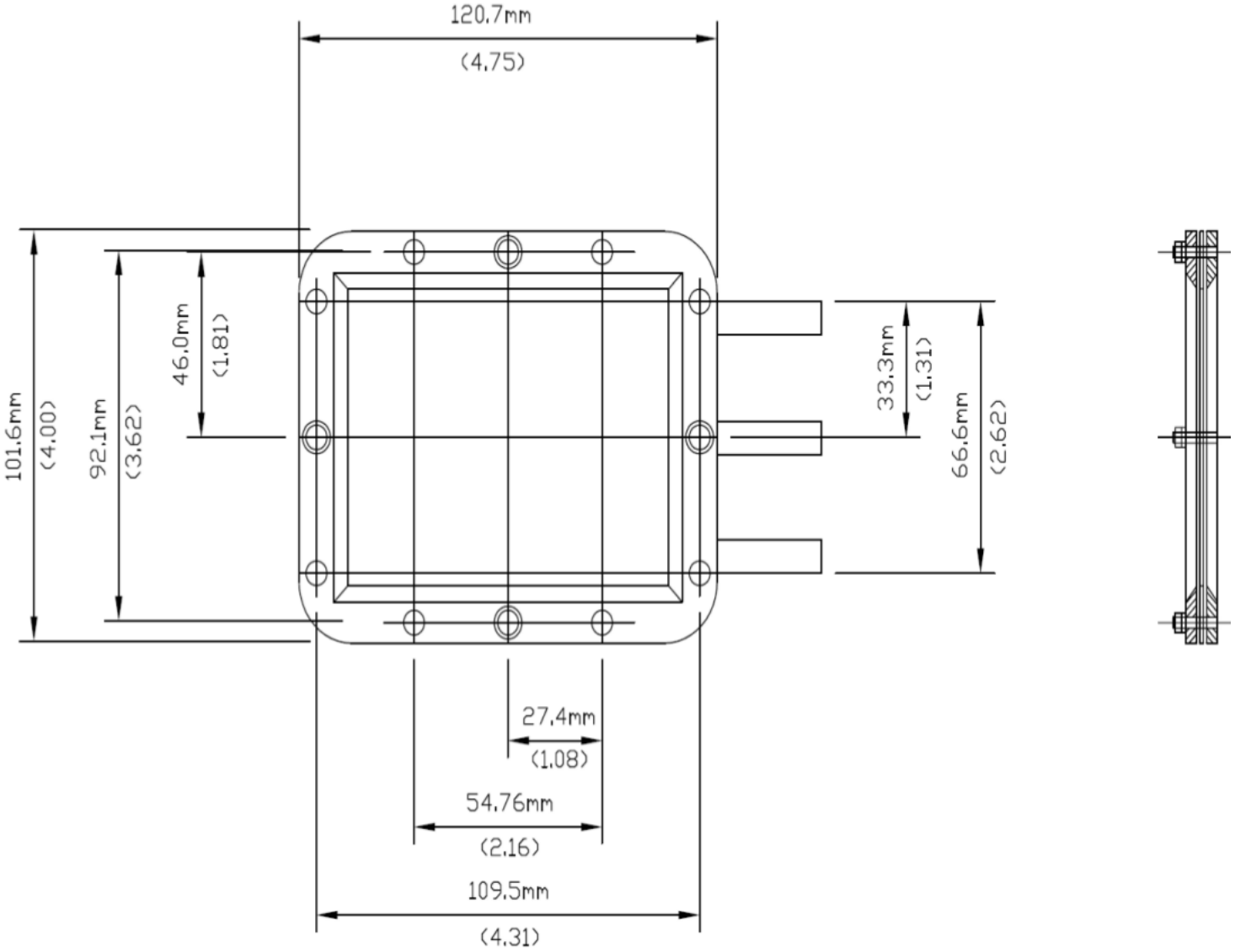

Figure 3.15: *Dimensions of the MCP used in the recoil detector* [10].

Table 3.1: *MCP features [10].*

Physical and Electrical features of the MCP	Specification
Dimensions	75 mm × 93 mm
Center to Center Spacing	32 μm Nominal
Pore Size	25 μm Nominal
Bias Angle	$8^o \pm 1^o$
Open Area Ratio	45 % Minimum
Electron Gain at 2kV	$4{\times}10^6$
Bias Current Range at 2kV	75-300 μA
Resistance 7-27 MΩ	
Pulse Height Distribution at 2kV	175% Maximum
Linear Output Current Density (μAcm^{-2})	10% of Bias Current Density

The MCP has stages with gains as shown in figure 3.16. Each stage cannot gain more than 10^4 but the gain can be improved by a chevron arrangement; where two MCP stages are used. The chevron arrangement is shown in figure 3.17. The chevron arrangement increases the gain and reduces the electrical noise. In figure 3.16, the MCP's different stages show that the maximum applied voltage for a single stage is 1 kV, 2 kV for a double stage, and for a triple-stage it is 3 kV. The gain increases exponentially with the increment of 1 kV from a previous stage to the next. The MCP for the recoil detector used in the experiment for this thesis work, was set such that a signal of amplitude 50 mV, with a width of 5 ns, at an impedance of 50 Ω is produced when 50 electrons released from an aluminium foil of thickness 10 μg/cm^2 by a Uranium nucleus. The gain required for the recoil detector was estimated using Ohm's law ($V = IR$), and the current definition ($I = \Delta Q/\Delta t$). The instantaneous current was calculated to be:

$$I = \frac{50 \times 10^{-3} V}{50\Omega} = 1 \times 10^{-3} A \tag{3.6}$$

and the charge was calculated to be:

$$\begin{aligned} \Delta Q &= 1 \times 10^{-3} A \times 5 \times 10^{-9} s = 5 \times 10^{-12} C \\ \therefore 5 \times 10^{-12} C &= 31 \times 10^{6} e^{-} \end{aligned} \tag{3.7}$$

These calculations imply that 50 detected electrons on the MCP should be multiplied to 31×10^6 electrons. This gain of 10^6 can be achieved with a two-stage MCP. Efficiency of the MCP as a function of electron energy is shown in figure 3.18. The maximum efficiency of 70% electron detection is expected from electrons having an energy of 0.5 keV. About 50% efficiency is expected from electrons having an energy of 1.6 keV released from the foil.

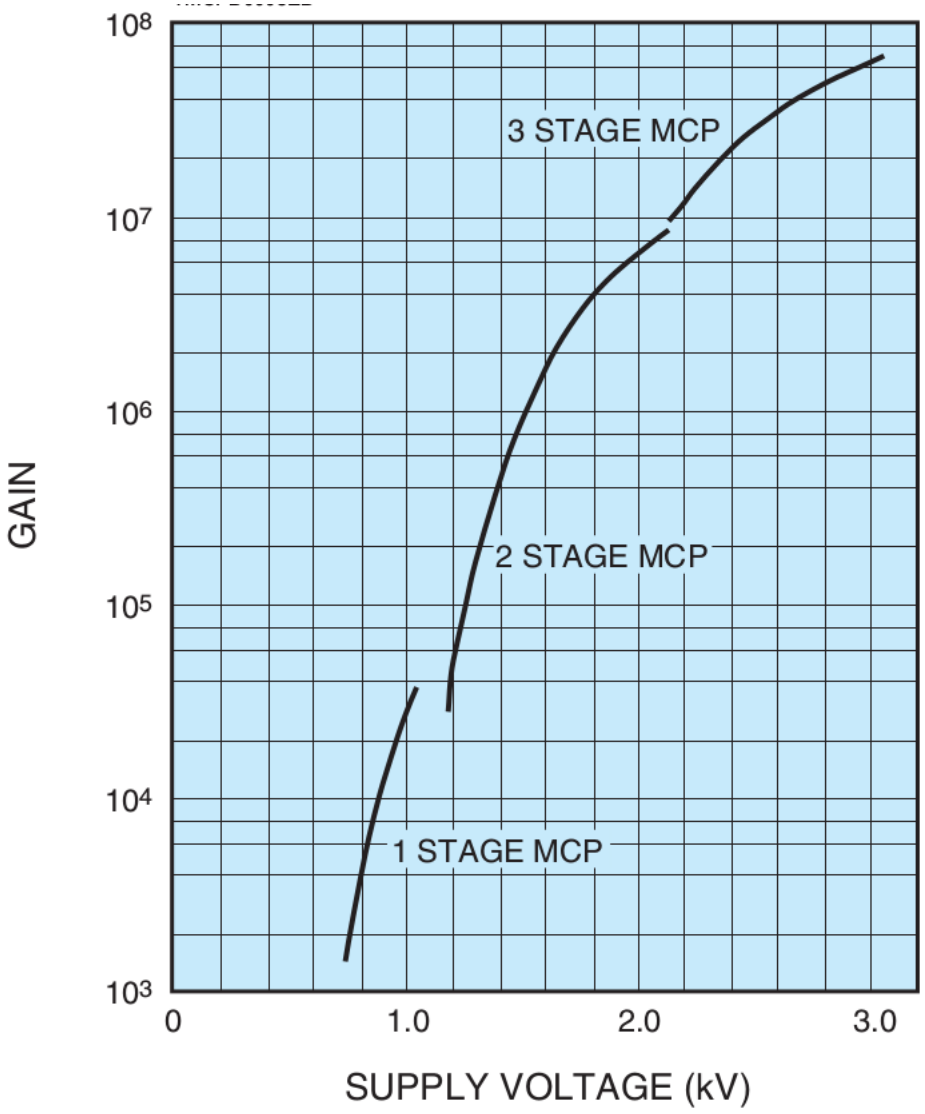

Figure 3.16: *Different stages of the MCP and their gains [40].*

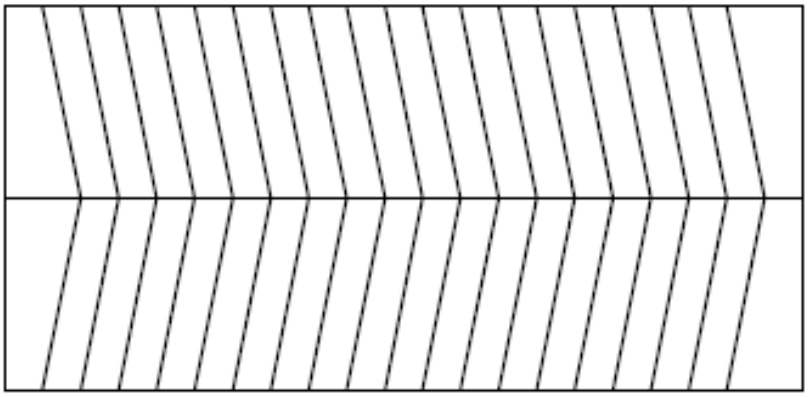

Figure 3.17: *Chevron arrangement of a two-stage MCP [10].*

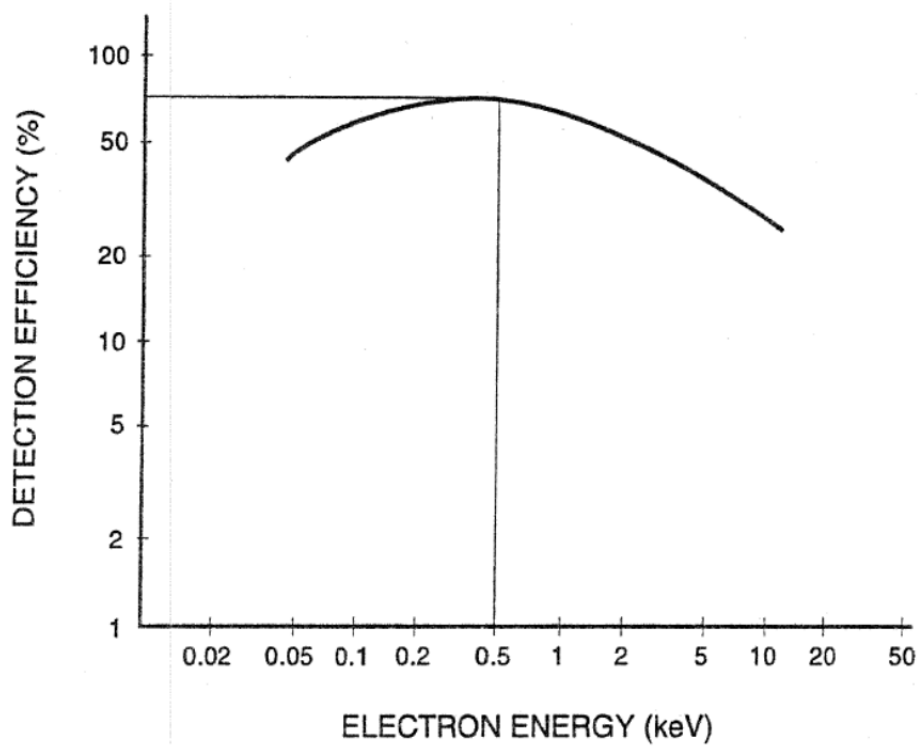

Figure 3.18: *The MCP's efficiency as a function of electron energy* [32].

3.5.3 Working condition of the MCP

The MCP requires a vacuum pressure less than 10^{-6} mbar. A high voltage of 2000 V can only be applied to the MCP if this desired vacuum is achieved. If not, it might result in damage to the MCP caused by sparking in the channels. Vacuum pumps need to be oil-free to avoid contaminating the MCP channels. The pumping of the system was controlled mechanically since the suction power of the pumps might damage or break the target. A fore pump was used to pump down the chamber to vacuum pressures of 10^{-1} mbar. After 10^{-1} mbar was achieved, a turbo pump was turned on to further pump down the chamber to orders of 10^{-6} mbar. It took two days to pump the system down into the desired vacuum pressure of 1.2×10^{-6} mbar.

3.5.4 Recoil detector testing

After the vacuum pressure requirements were achieved, the recoil detector was tested with room background radiation randomly hitting the Al foil, and releasing electrons. The high voltage was slowly applied up to 2000 V. A negative voltage of 300 V was applied to the foil, to create an electric field to accelerate the electrons. During the test, the output signal from the MCP was connected and monitored on an oscilloscope. Pulses were first observed at voltages between 1800 - 1900 volts, which is close to the MCP bias voltage of 2000 V. Figure 3.19 shows a photograph of an observed pulse from the oscilloscope. To confirm that the signals indeed came from the MCP, the foil voltage was dropped, in doing so, the signal slowly faded away until it disappeared, and only reappearing if the foil voltage was increased.

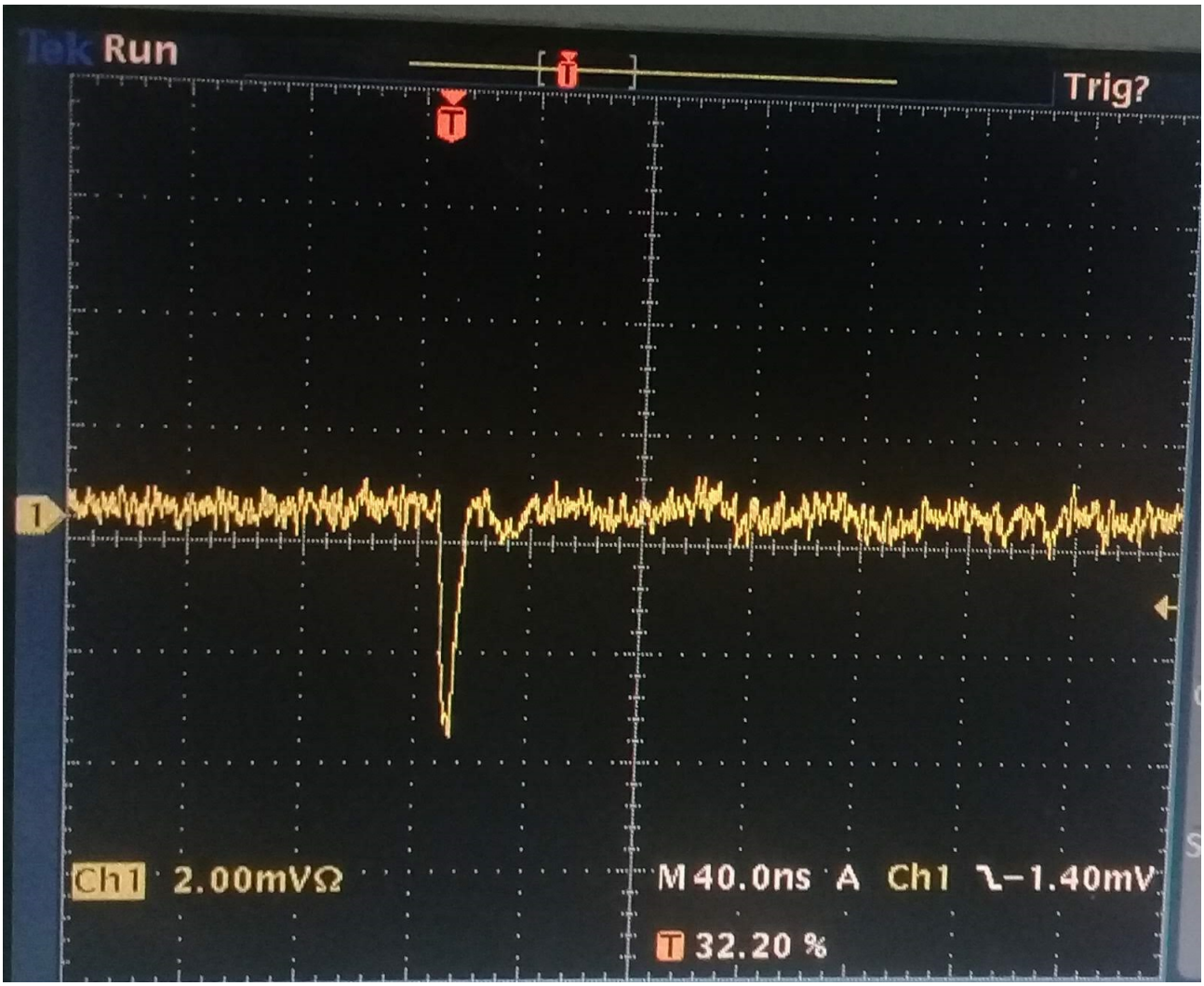

Figure 3.19: *A photograph of an oscilloscope showing the signal from the MCP.*

3.5.5 Recoil detector signal processing

A signal processing diagram of the recoil detector is shown in figure 3.20 with a corresponding timing diagram shown in figure 3.21. The MCP signal is amplified through an ORTEC 574 timing amplifier, before being split into two. The location of the split signal is shown at **A** in figure 3.20 and its time relation is shown labeled **A** on 3.21. The one split signal is passed through a delay, and then goes to an input of a 16 channel Pixie-16 XIA digital Analog-to-Digital Converter (ADC), where it is digitized. The other signal is fed into an ORTEC 934 Constant Fraction Discriminator (CFD) **C**. The CFD converts any signal that exceeds a low-level threshold, which is set to reject noise, into a fast logic pulse.

Because of the rate limitations of the XIA ADC, it is necessary to gate the ADC with a signal indicating the detection of a recoil, since the MCP fires on nearly every beam pulse when it detects scattered beam. Recoils are distinguished from scattered beam by their time-of-flight. The time of arrival for the recoils is shown delayed with respect to the prompt (scattered beam) signal in figure 3.21 **B**. To time the recoils, the RF signal from the cyclotron is used as a reference. After stretching and delaying the RF signal, a gating signal is produced, **C**, that gates the recoil signal through the LeCroy 755 coincidence module to produce a master gate (MG) **D**. The master gate is then used to gate the XIA module after being translated into a Transistor-transistor logic TTL logic signal. To measure the time-of-flight of the recoils it is also necessary to record the time of the nearest RF signal using the XIA ADC. Unfortunately the RF rate ($\approx$ 3.6 MHz) is also too high for the ADC. Therefore, the RF timing signals **F** are also gated, by a stretched master gate **E**, using a 755 module, before being presented to the input of the XIA ADC.

Signals from the clover detectors and Bismuth Germanate (BGO) Compton suppression shields are presented as an input to other XIA ADCs. The rest of process is controlled by the digital data acquisition system.

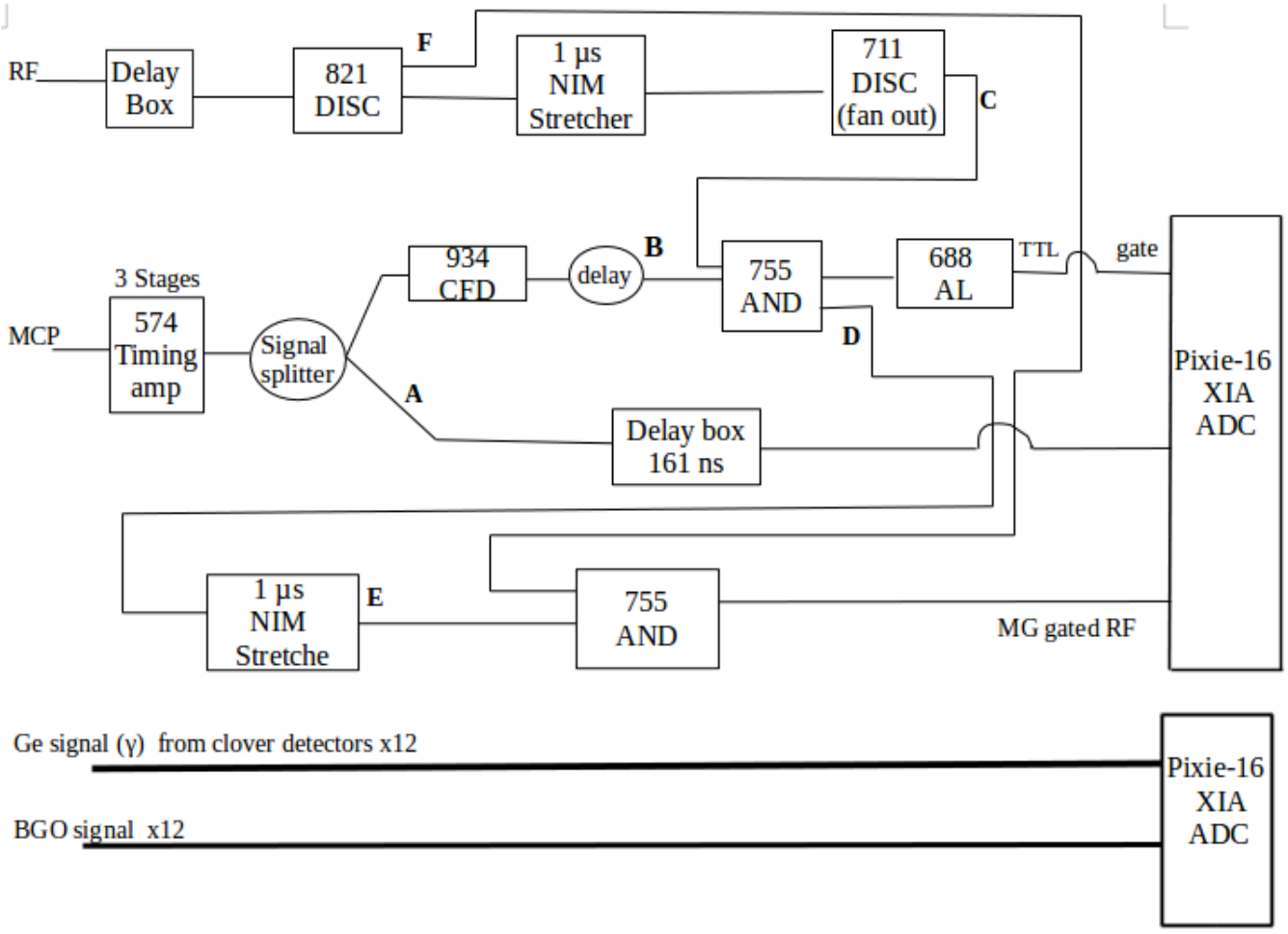

Figure 3.20: *A circuit diagram of the recoil detector electronics.*

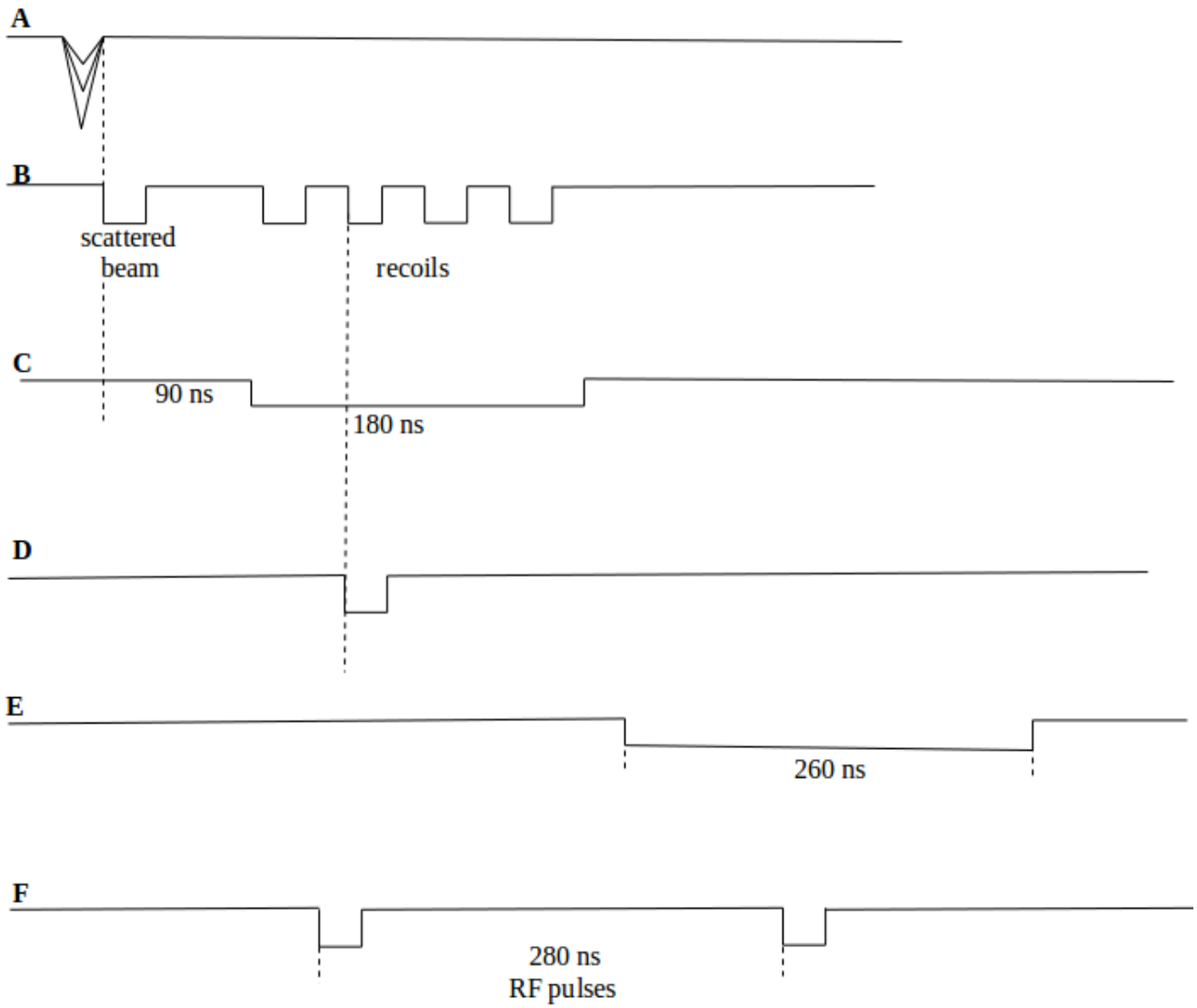

Figure 3.21: *Timing diagram of the recoil detector signal.*

3.6 Data Acquisition System and Digital ADCs

A gamma-ray of energy E_γ is said to be detected if it interacts with the detector crystal, and releases electric charge Q. The charge is converted to electric pulses that contain information about the gamma-ray such as the energy, resolution, time distribution, etc. The pulses are sent to a data acquisition system where they are eventually displayed as a spectrum. Data for this thesis work was collected using MIDAS (Multi Instance Data Acquisition System) a digital data acquisition system used at iThemba LABS. The digital data acquisition system has a front-end system consisting of XIA crate, and Pixie-16 modules, connected to a server computer which runs the modules, and the data acquisition system. Figure 3.22 shows a picture of the side view and front view a Pixie-16. The data acquisition system has a control part on the server computer which runs the merge, filter, event-builder, online sort, storage, and graphical user interface. Data is read from the merge, and output to TapeServer. The TapeServer stores data locally on a disc, network, tape, etc. The stored data was sorted with MIDAS MTsort with the following input handlers; EurogamDisk for online sort, and TDRDisk for offline sort.

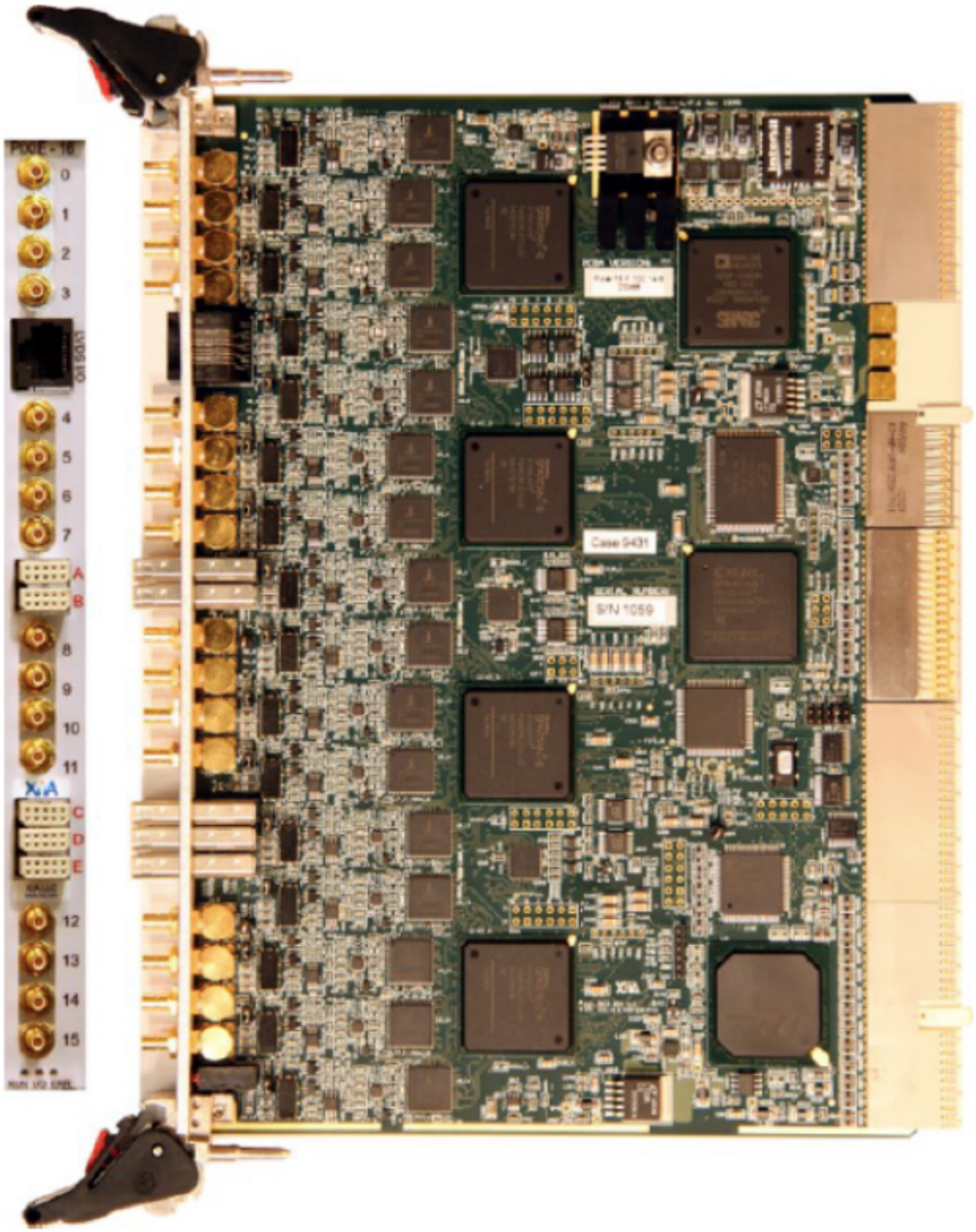

Figure 3.22: *Picture of the front (left) and side view (right) of a Pixie-16 module [41].*

3.6.1 Pixie-16 XIA Operation

In figure 3.23, an HPGe detector **D**, operated with a sensitive preamplifier **A**, is shown. The detector is connected to the input of preamplifier with feedbacks capacitor $\mathbf{C}_f$, and resistor $\mathbf{R}_f$. The detector is biased with voltage V. Figure 3.24 shows the output signal of the preamplifier as a step of amplitude V_x after a gamma-ray of energy E_γ interacted with the detector. The charge released when the gamma-ray of energy E_γ is detected, is given by:

$$Q = E_\gamma/\epsilon \tag{3.8}$$

and ϵ is a material constant. When Q is integrated onto C_f, the applied voltage V_x can be calculated as follows:

$$V_x = Q/C \implies V_x = E_\gamma/\epsilon C \tag{3.9}$$

Therefore, to measure E_γ requires the measurement of V_x in the presence of a preamplifier noise σ, see figure 3.24.

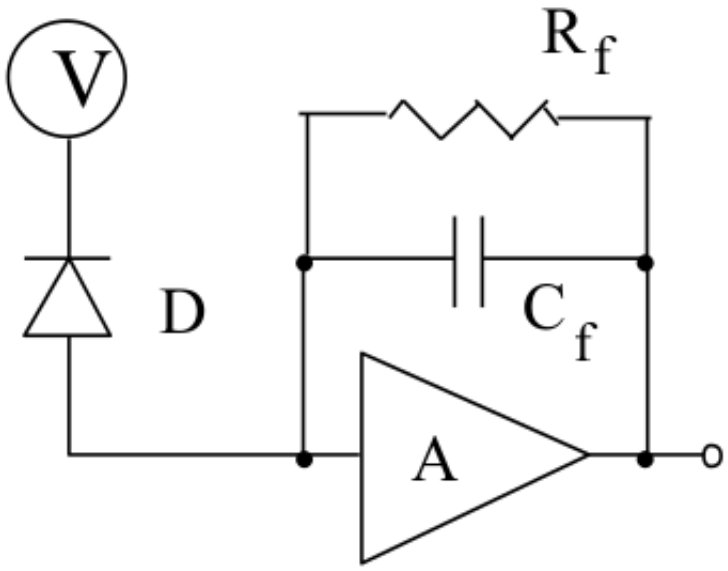

Figure 3.23: *A detector **D** biased with voltage source **V** is connected onto a charge sensitive preamplifier **A** with RC feedback, figure taken from [41].*

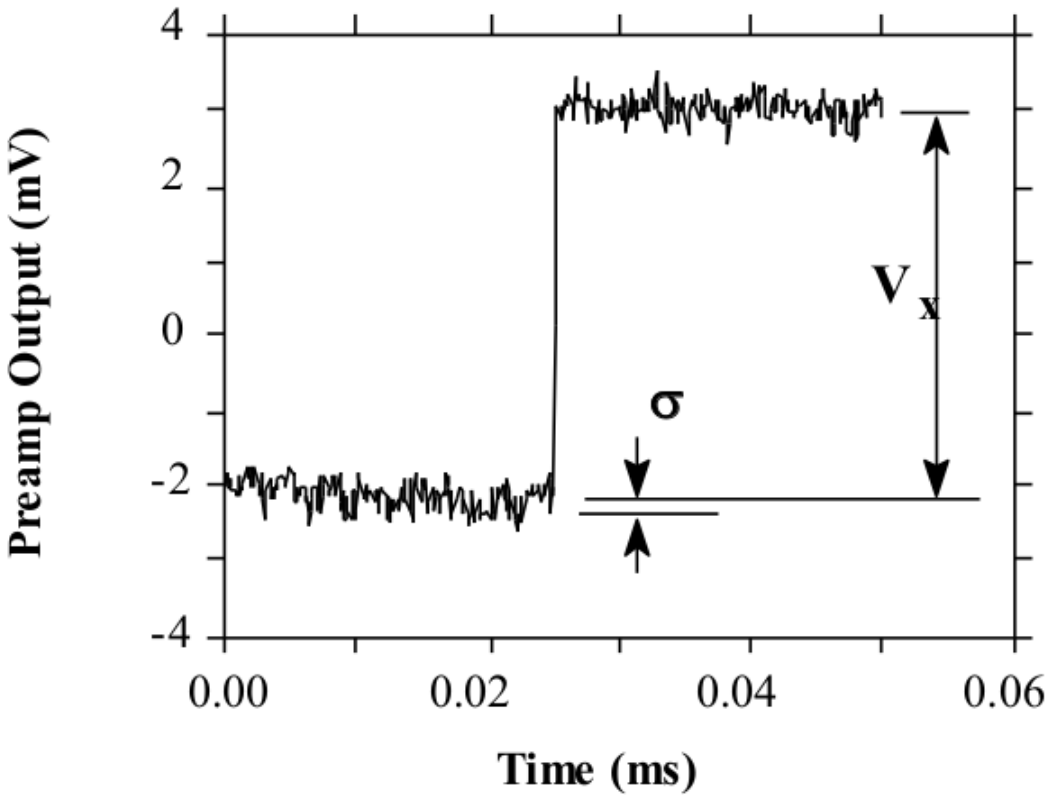

Figure 3.24: *Output signal on absorption of gamma-ray, figure taken from [41].*

Noise in electrical measurements can be reduced with filtering. After filtering, the signal is digitized and is no longer continous, but has discrete values as shown in figure 3.25. To determine V_x from this data set, the points before the steps are averaged and subrtacted from the averaged points after the step [41]. The averages of the points before and after the step are calculated from the regions labeled "Length" on figure 3.25, and V_x is obtained as follows:

$$V_{x,k} = \sum_{i(after-gap)} W_i V_i - \sum_{i(before-gap)} W_i V_i \tag{3.10}$$

Where W_i are the weighting values which determine the type of average being calculated. If larger weighting values are used for data close to the step, and smaller weighting values are used for data far from the step, equation 3.10 produces cusp-like filters. For weighting values that are constant, equation 3.10 produces triangular or trapezoidal filters [41].

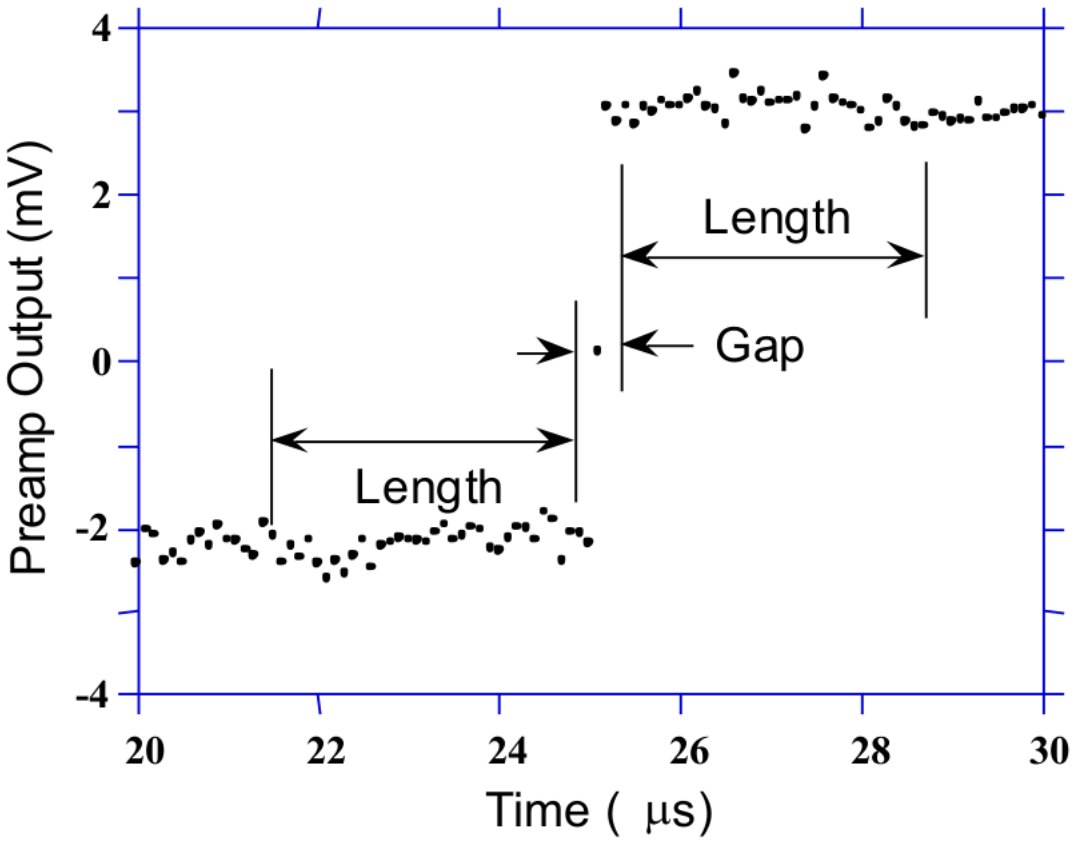

Figure 3.25: *Digitized version of the data of Figure 3.24 in the step region, figure taken from [41].*

The trapezoidal filtering is implemented in a Pixie 16 module. Figure 3.26 shows the trapezoidal filter with length, L = 1 μs, and Gap, G = 0.4 μs. The trapezoid has a rise time equal to L, a flattop

equal to G, a decay time equal to L, and basewidth equal 2L+G. The basewidth is a measure of the filter's noise reduction properties.

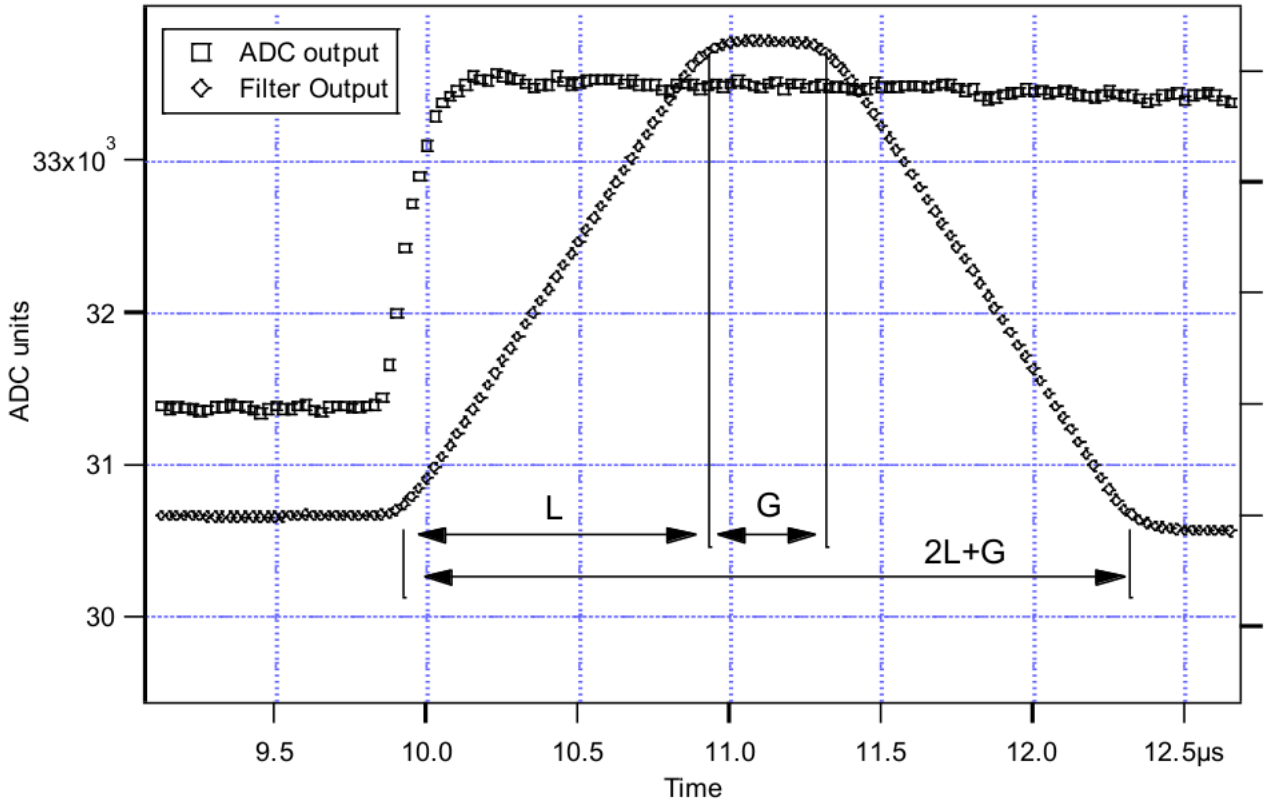

Figure 3.26: *Trapezoidal filtering of a preamplifier, figure taken from [41].*

One advantage of the trapezoidal filter pulse over analog filtered pulse, is the sharp termination of the trapezoidal pulse on completion of the basewidth 2L+G which gives the digital filter a definite rate advantage in pileup-free throughput.

Figure 3.27, shows a gamma-ray event over a long-time period, and it also shows the treatment of the preamplifier noise by the filters in regions where no gamma-ray pulses are present. As may be seen from figure 3.27, the filter reduces both the amplitude fluctuations and their high frequency content. This region is called the baseline, it establishes the reference level from which the gamma-ray peak amplitude V_x is to be measured. The fluctuations at the baseline produce an electronic noise, σ_e, a number which depends on the rise time of the filter used. The gamma-ray peaks contributes an additional noise called Fano noise, σ_f to the system. The total noise, σ_t, in measuring V_x, is given

by the square rooT of the sum of the electronic noise and Fano noise:

$$\sigma_t = \sqrt{\sigma_e + \sigma_f} \tag{3.11}$$

The electronic noise comes from the preamplifier and the amplifier, and the Fano noise comes from the detector material.

The slope of the preamplifier is not often zero for an RC feedback preamplifier. All steps decay exponentially to the DC level of the preamplifier. During the decays, the baselines are not obviously zero. The filter output during the exponential decay after the pulse is below the initial level, and the flat top region is sloped downwards, see figure 3.27. The decay constant τ, can be used to map back the baselines to the DC level. Even if the the pulse overlaps on the falling slope of the previous pulse, the use of τ allows the gamma-ray energies to be computed with high precision [41].

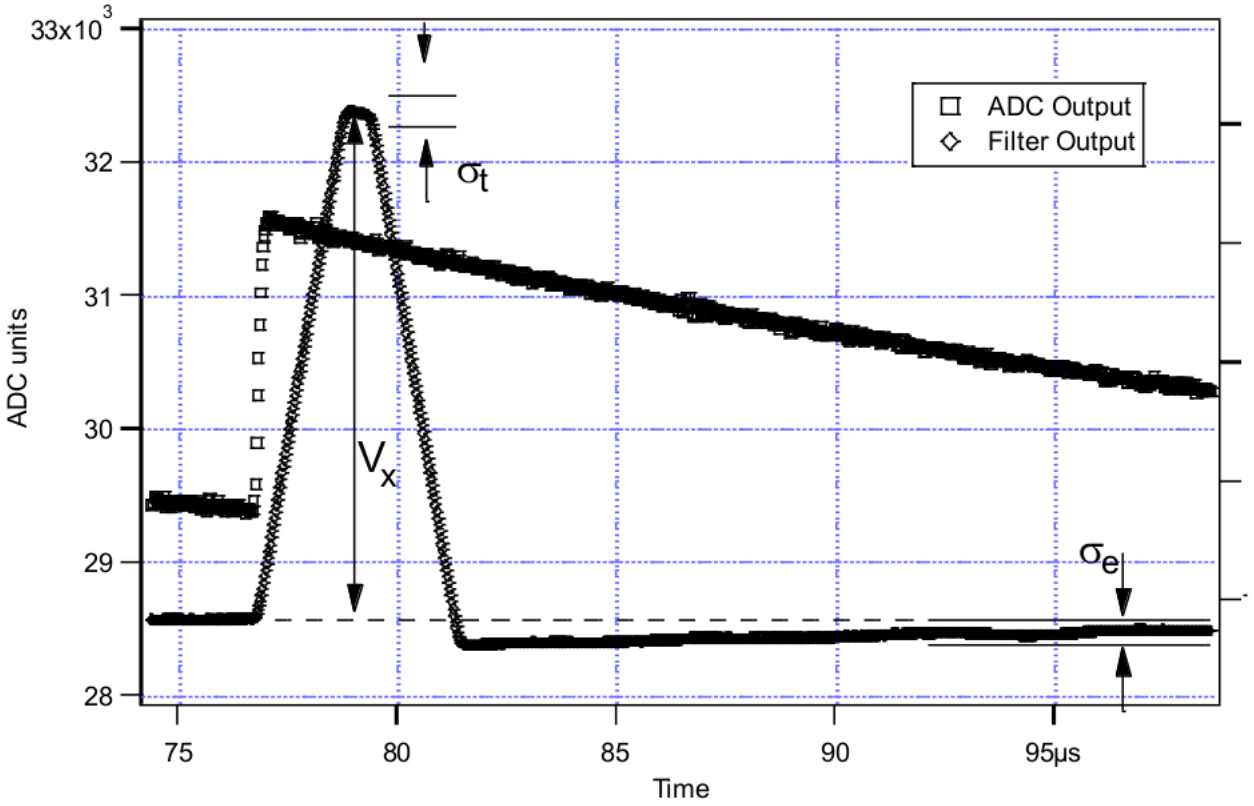

Figure 3.27: *A gamma-ray event over a long time period, and the treatment of the preamplifier noise by the filters in regions where no gamma-ray pulses are present, figure taken from [41].*

3.6.2 Pixie-16 Set Up

The Pixie-16 module communicates with the server computer through a PCI interface. The operation of the Pixie-16 is controlled by a variety of parameters. Before the experiment started, and the collecting of data, the parameters were optimized. Figure 3.28 shows the Pixie-16 data acquisition parameters window. The main parameters optimized were: Trigger Threshold, Decay Constant (τ), and Energy Risetime. The trigger threshold should not be set too low or too high. If it is set too low, it will allow unwanted events to be detected. If it is too high, low energy gamma-rays could be rejected. Therefore, the trigger threshold should be set just above the detector's noise level. The parameter for energy computation is the decay time (τ) of the signal. At high count rates, pulses overlap. With the assumption that pulses have a single decay constant, τ is used to compute the correct energy of the overlapping pulse on the decaying tail of the first pulse. The energy rise time is varied to get a better resolution.

A ^{152}Eu source was used for the optimization of the parameters. After every ten thousand counts from the source, the acquisition was stopped, and the peaks were fitted to get the full width at half maximum (FWHM) to calculate the detector's resolution. For the ^{152}Eu source, the resolution at higher energies was expected to be above 2.1 keV (for this experiment the resolution at higher energies was checked on the 1408 keV peak), and for peaks at lower energies, it was expected to be within 1.1 keV (the resolution at lower energies was checked on the 121 keV peak). Parameters that gave an optimum performance for each detector were saved, and then used for in-beam data collecting.

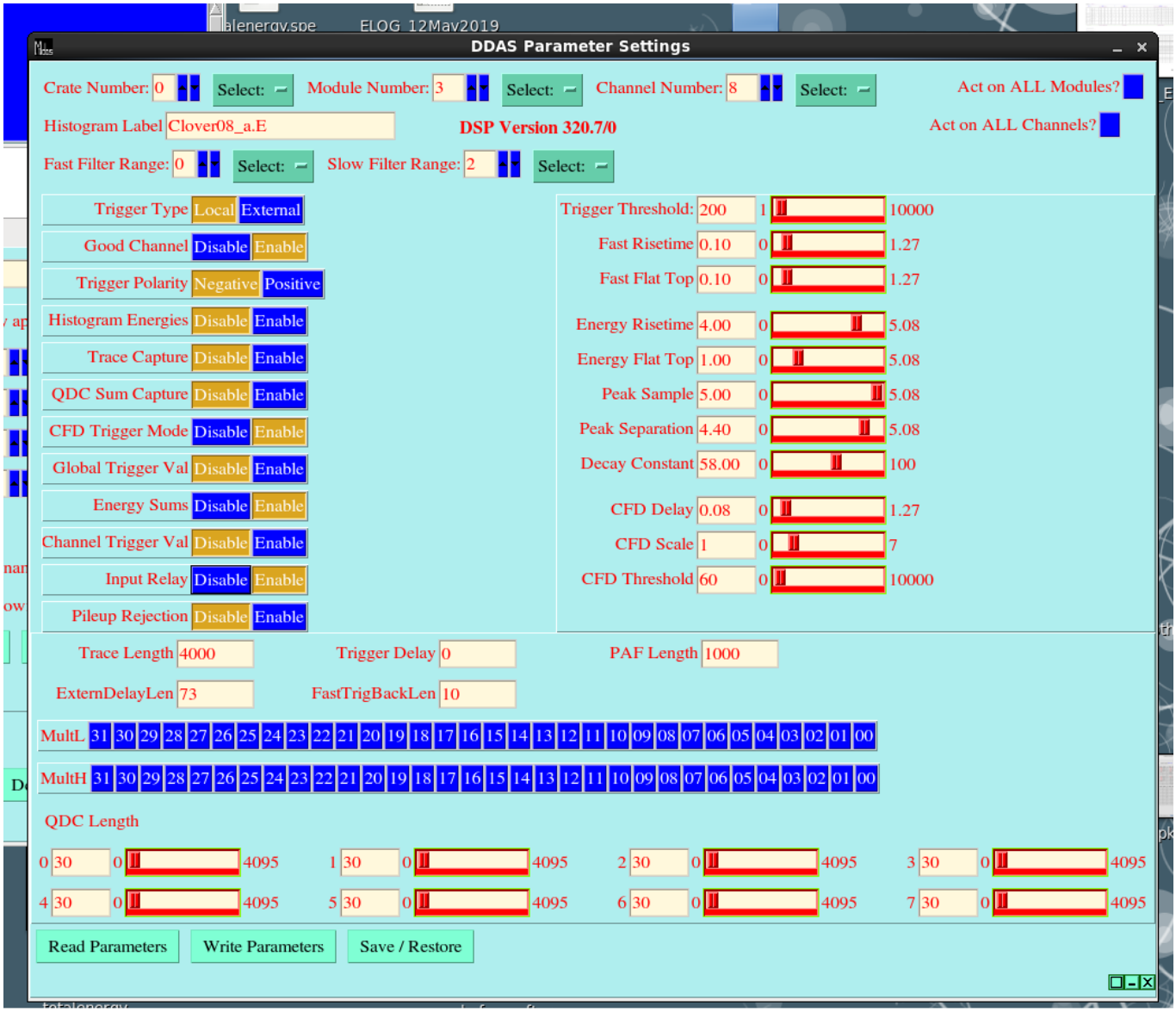

Figure 3.28: *A screenshot of the parameter setting window on MIDAS.*

Chapter 4

Data analysis

This chapter explains the energy and efficiency calibrations of the clover detectors, the steps taken in analysing the experimental data, and the significance of the recoil detector on background suppression.

4.1 Energy calibration

Energy calibration of the clover detectors was done with a ^{152}Eu source. The source was positioned in the center of the array, and the data collected for 30 minutes. The saved spectra were then converted into a GF3 file [42]. Thereafter, an auto-calibration in GF3 was performed. The auto-calibration finds the centroids of the photo-peaks; those that failed to be fitted automatically were fitted manually. GF3 performs the energy calibration by determining the relationship between the channels, and gamma-ray energies in a form of a quadratic equation:

$$E = a + bx + cx^2 \tag{4.1}$$

where a, b, and c are calibration coefficients later used for aligning the peaks, and are unique for each clover detector crystal, and x is the channel number. The energy dispersion for the calibrated detector was set to be half a keV per channel (i.e, $E = 0.5x$). Figure 4.1 shows the ^{152}Eu source spectrum used for the energy calibration.

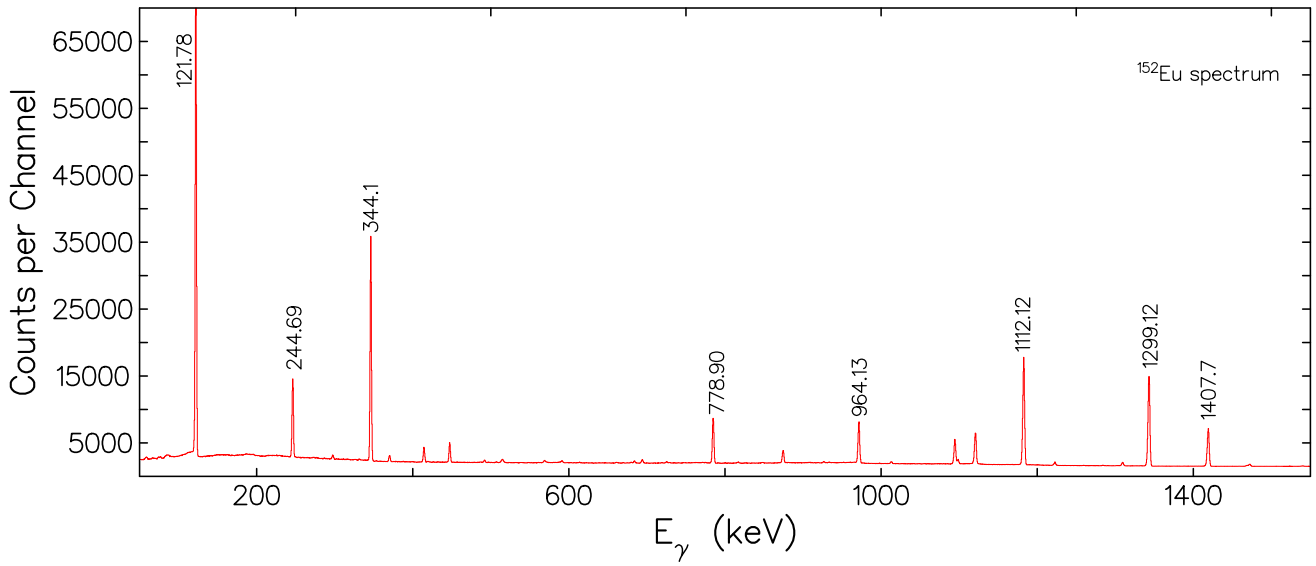

Figure 4.1: *Gamma-ray energy spectrum of* ^{152}*Eu source, used for energy calibrations.*

4.2 Efficiency calibration

The efficiency calibration was carried after the last run of the experiment using ^{152}Eu and ^{133}Ba sources. Each source was placed in the target position, to ensure gamma-rays would be absorbed as they were during the experiment. The data collected for each source was saved and later sorted to get the addback total energies of all the spectra from the clover detectors. The efficiency curve for the clover detectors is shown in figure 4.2. The clovers have highest efficiency near 50 keV , which decreases as the energy increases. The decrease in efficiency is caused by the decrease in cross-section of the photoelectric effect and Compton scattering as a function of gamma-ray energy. All the steps for efficiency calibration were performed with EFFIT package from RADWARE [42]. The efficiency curve is obtained from equation 4.2

$$eff = exp[(A + Bx + Cx^2)^{-G} + (D + Ey + Fy^2)^{-G}]^{-1/G} \tag{4.2}$$

where $A+Bx+Cx^2$ describes the efficiency at low energies, and $D+Ey+Fy^2$ describes the efficiency at high energies. G is an interaction parameter between the low energy region, and the high energy region; it determines the efficiency in the turnover region. The parameters x, and y are determined from the equations [42]:

$$x = log\left[\frac{E_\gamma}{100}\right] \tag{4.3}$$

and

$$y = log\left[\frac{E_\gamma}{1000}\right] \tag{4.4}$$

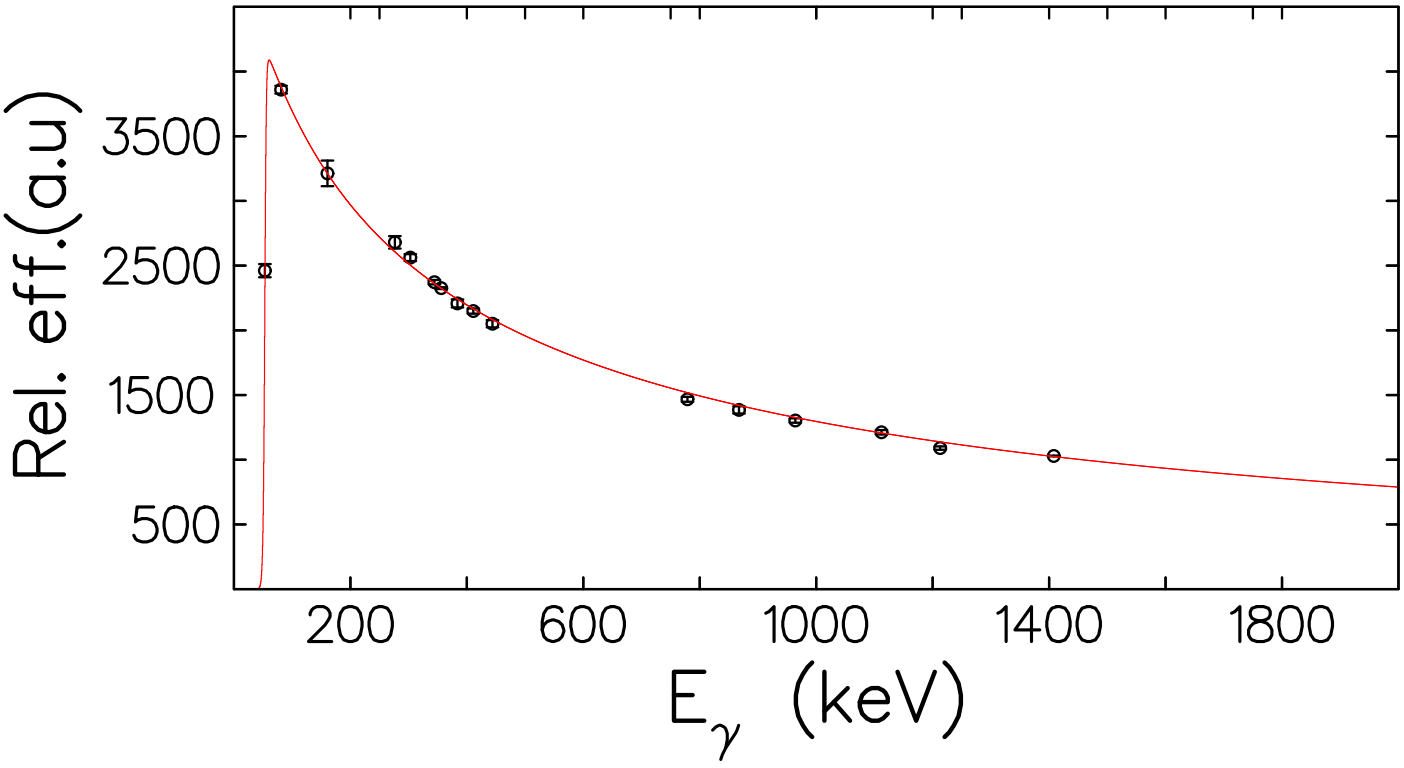

Figure 4.2: *The relative efficiency for clover detectors measured with* ^{152}Eu *and* ^{133}Ba *sources mounted at the target position.*

4.3 Data Analysis

The collected in-beam data was stored on disk for offline sorting. Due to numerous changes throughout the experiment, including beam changes affecting the RF timing, shifts in the gain of the recoil detector MCP signal, shifts in the RF energy signal, and the need to accurately gain match the clover data in the absence of strong peaks, the data needed to be carefully checked on a run-by-run basis.

4.3.1 Gain-matching

During the experiment, there were shifts in the energy calibrations of the clover crystals, which were caused by temperature variations during the run of the experiment. These shifts disrupt the gain matching, and result in misaligned peaks in clover spectra. The shifts were corrected relative to an accurately calibrated spectrum from the beginning of the experiment before any shifts occurred. A strong peak at 140 keV, produced by neutrons striking the Ge crystal of the clover detectors, the target X-rays, and the 511 keV peak were used as references from the first runs at the beginning of the experiment. The shifted spectra were manually fitted in GF3 to extract their centroids, and new gain-matching coefficients were calculated as follows:

$$\begin{aligned} X'_1 &= A + BX_1 \\ X'_2 &= A + BX_2 \end{aligned} \tag{4.5}$$

$$\begin{aligned} a' &= B \times a + A \\ b' &= B \times b \\ c' &= B \times c \end{aligned} \tag{4.6}$$

where X' is the unshifted centroid (correct centroid for the peak), X is the shifted centroid (centroid to be corrected), and (a', b', and c') are the new gain-matching coefficients. One must be consistent in choosing the peaks for gain-matching. After the gain-matching was done, the data was pre-sorted to have all the peak centroids from all the clover detectors aligned.

4.3.2 Recoil detector background suppression

After all the peaks from the clover detectors where aligned, it was necessary to optimize the background suppression with the Recoil detector before the data was sorted into a gamma-gamma matrix. The gamma-rays detected in the clover detectors must coincide with the detection of recoils from the Recoil detector to ensure that indeed the gamma-rays came from the recoils. Time and energy conditions for the Recoil detector MCP, and the clover detectors, were set for making the gamma-gamma coincidence matrix.

Energy and time gating had to be optimized to minimize the background in the gamma-ray energy spectrum of the clovers. In figure 4.3, a clover-RF time spectrum is shown. This spectrum was generated by calculating the time difference between the clover detectors and the RF-signal. The prompt-peak is the tallest peak in the spectrum; it is produced from prompt gamma-rays, while the other peaks come from gamma-rays produced in other beam pulses. A gate was set on the prompt peak to select only the prompt gamma-rays; the gate must not be too wide to avoid the next beam pulse, and it must not be too narrow so as not to cut out some of the coincidence gamma-rays. The time difference between any two successive peaks on the spectrum is 282 ns, which corresponds to the RF period.

A spectrum of MCP time, recorded in coincidence with prompt gamma-rays, is shown in figure 4.4. This spectrum shows the time it took for different particles to reach the MCP. Recoils are expected to reach the recoil detector within the set time gate. There is a spread in the times due to the evaporation of neutrons, energy loss in the target and the solid angle of the detecting foil. Figure 4.5 shows an MCP energy spectrum gated by the prompt gamma-rays. This spectrum shows the measured energies of the recoils detected by the Recoil detector MCP. However, there are many particles such as electrons, scattered beam, and fission fragments that can be detected by the MCP, hence the MCP energy gate was carefully selected to reduce the background and other contaminants in the clover energy gamma-ray spectrum.

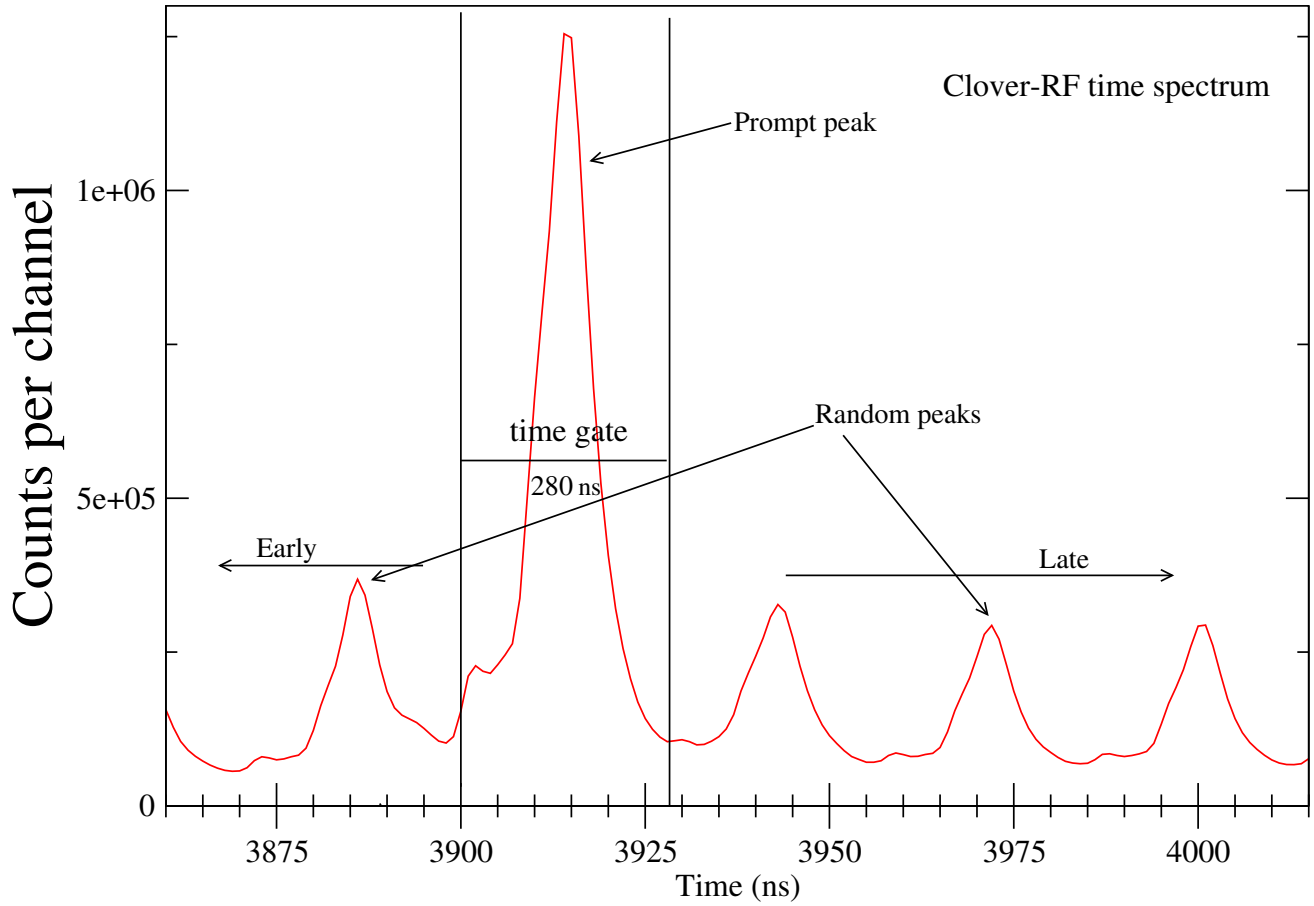

Figure 4.3: *A clover-RF time spectrum showing the time gates for the clover detectors, each channel is 10 ns. The time window; which is the time difference between the two limits is 280 ns.* .

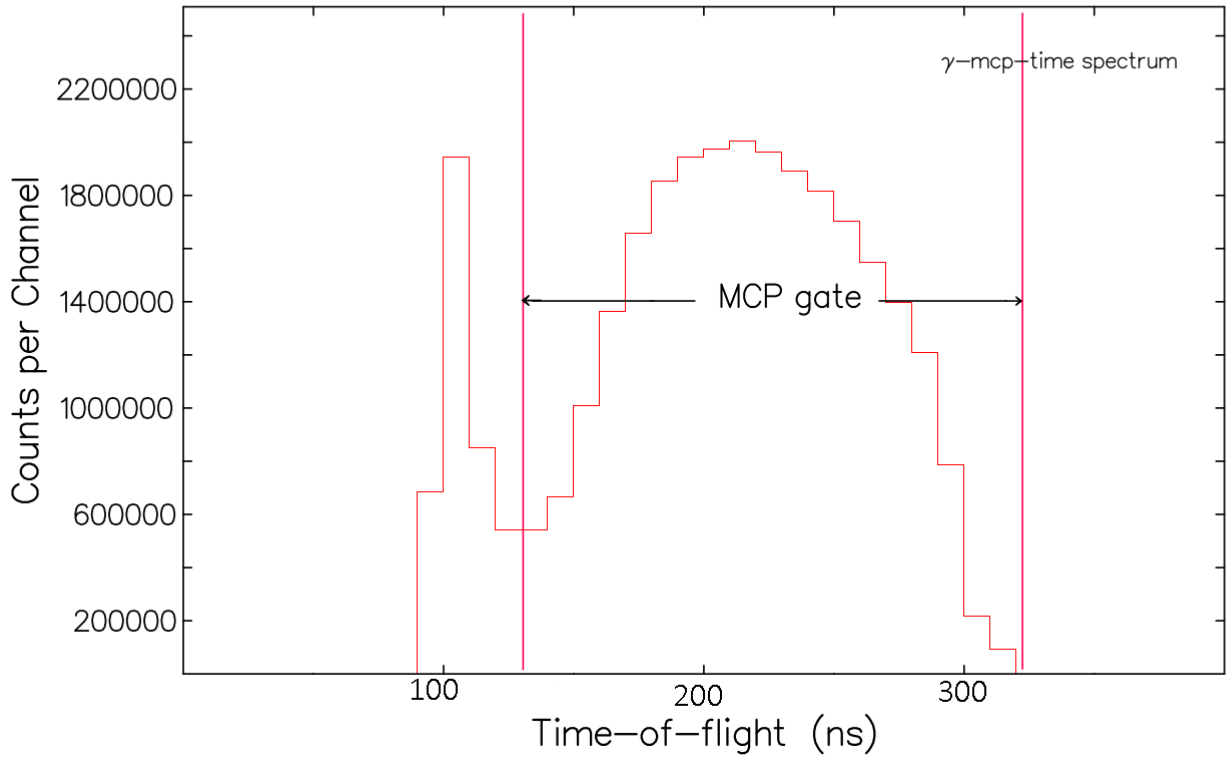

Figure 4.4: *MCP time spectrum of the recoil detector. This spectrum shows the time-of-flight for the recoils to reach the recoil detector.*

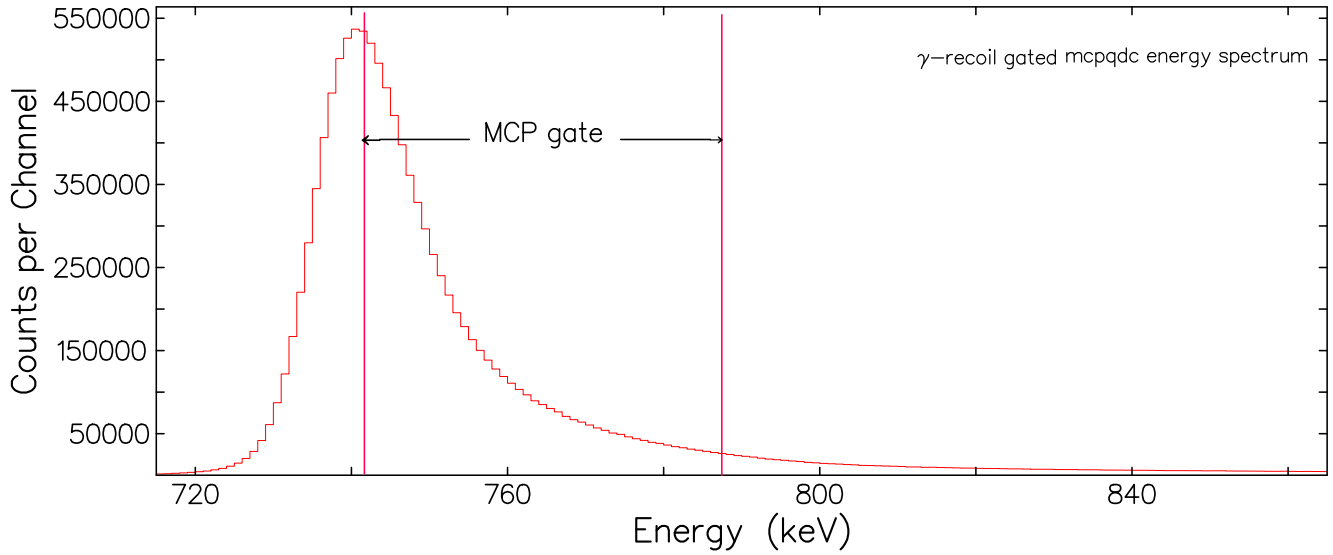

Figure 4.5: *A gamma-recoil gated MCP energy spectrum. The region between the gates shows the energies of the recoils.*

In figure 4.6, spectrum (a) shows a clover gamma-ray energy spectrum obtained with AFRODITE alone (this spectrum is obtained with no MCP energy and time gating). Spectrum (b) shows a clover recoil-gated gamma-ray energy spectrum (this spectrum is obtained when AFRODITE is gated by the Recoil detector). Comparing the two spectra, the significance of the recoil detector is obvious. In spectrum (a), there is a high background contribution to the clover energy spectrum, this can be seen from the strong 511 peak, and the lack of uranium peaks. In spectrum (b), the background is suppressed, this can be seen from the disappearance of the 140 keV, and 198 keV peaks, and the reduction of the 511 keV peak. The 140 keV peak is due to neutrons interacting with the Ge crystal, the 198 keV peak is an Al gamma-ray from the target frame when is hit by neutrons, and the 511 keV peak is from electron-positron annihilation. With the background suppressed by the recoil detector in spectrum (b), Uranium lines and other byproducts of the reaction are visible. Figure 4.7 shows the clover recoil-gated energy spectrum with the labeled peaks, and their associated reaction products.

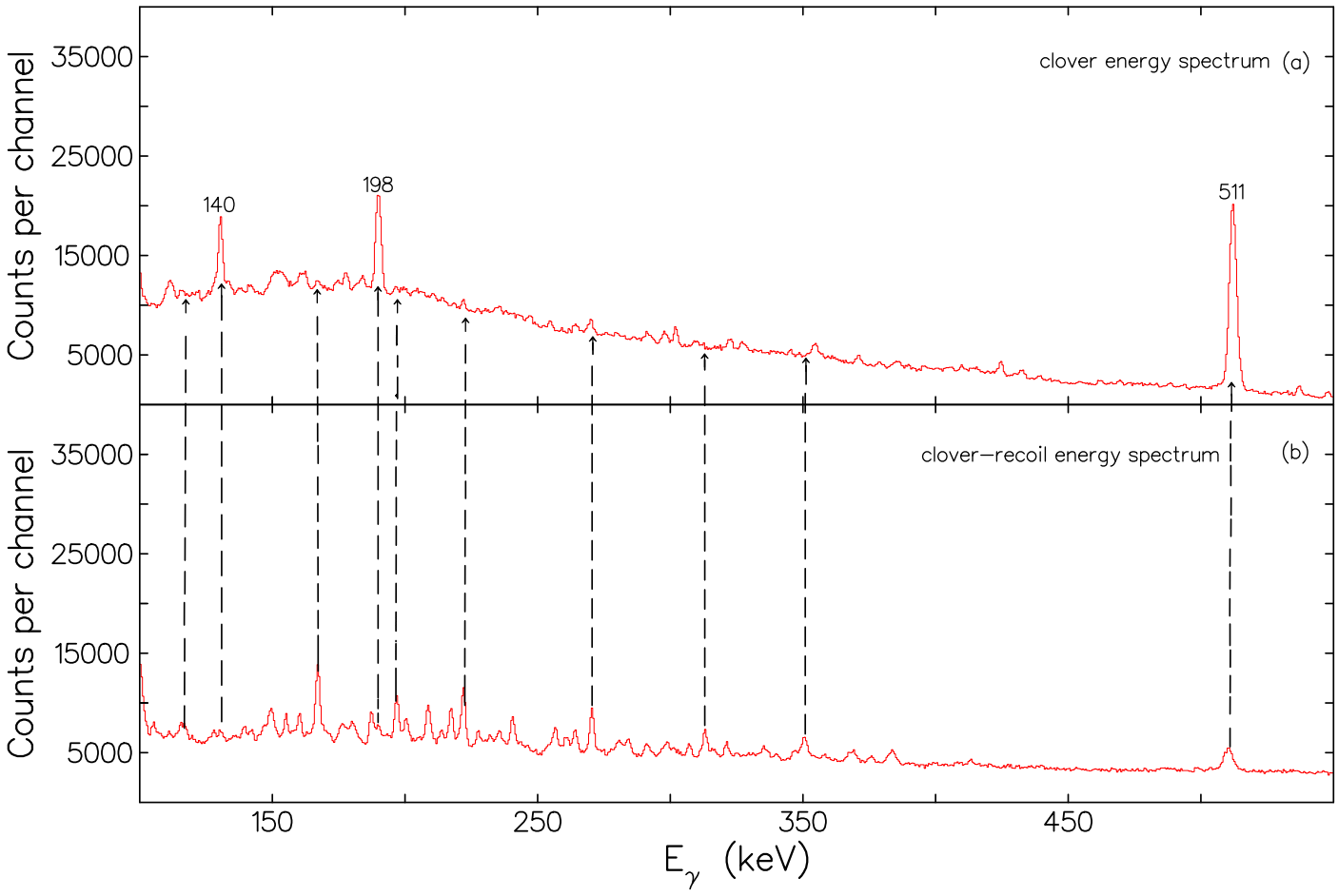

Figure 4.6: *Clover energy spectrum obtained from AFRODITE only (a), and clover-recoil energy spectrum from AFRODITE gated by the Recoil detector (b). The dashed lines map the positions for the invisible Uranium lines on the clover energy spectrum, high background on (a) obscure these lines.*

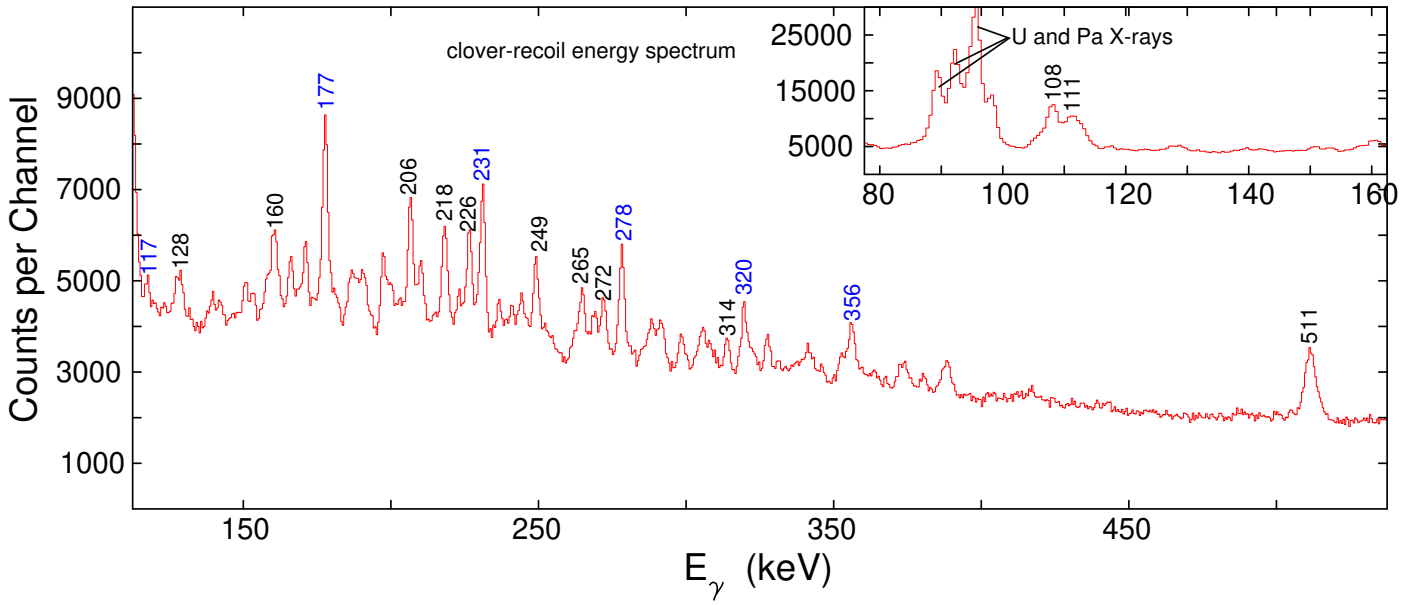

Figure 4.7: *Clover-recoil energy spectrum with labeled peaks, the blue labeled peaks correspond to Uranium-230 and the other peaks correspond to other nuclei produced (Th-228, Pa-231, and U-232). The observed X–rays corresponding to this spectrum are shown in the insert.*

With the gates set on the MCP time and energy spectra, the data was sorted into a γ-γ-recoil matrix (a γ-γ matrix made up of gamma-rays that were detected in coincidence with a recoil). Only gamma-rays falling within the prompt time window contributed to building the γ-γ-recoil coincidence matrix. To make sure that only gamma-rays in the prompt-peak contributed to the matrix, a random subtraction was done by producing a matrix from the random-peaks and subtracted it from the matrix produced from the prompt-peak.

Chapter 5

Results and Discussion

This chapter presents and discusses the results in the context of the aim of the study obtained after the data analysis from the previous chapter. The results include level schemes produced from the experimental data and the discussion gives an understading of the results and findings in the context of the aim.

5.1 Level scheme construction

A RADWARE program called ESCL8R [42] was used to aid the construction of the level scheme from the recoil-γ-γ matrix. The program requires the energy calibration file, efficiency calibration file, projection spectrum and background spectrum files from the matrix. The energy and efficiency calibration files were created in GF3 with the packages, ENCAL, and EFFIT respectively [42].

5.1.1 Uranium-230 level scheme

A level scheme for the nucleus ^{230}U produced from this thesis work is shown in figure 5.1. The ground state band transitions, and the negative-parity band transitions for ^{230}U from the observed gamma-rays are shown. The ground state band had been populated up to the 22^+ state. Unfortunately, no new transitions have been added to the ground state band compared to the previous work (figure 1.2).

The negative-parity band had already been observed with E1 transitions connecting it to the ground state band. The present objective was to observe the in-band E2 transitions in the low-lying states of the negative-parity band. However, no new in-band E2 transitions were observed from these states. But, two new states, 19^-, and 21^- have been tentatively added to the negative-parity band of the level scheme. These new added states in the negative-parity band were placed with two new tentative inter-band E1 transitions connecting them to the ground state band, see figure 5.1.

The new tentative inter-band E1 transitions linking the states, (19^-), and (21^-), to the ground state band have 336 keV and 327 keV energies, respectively. In addition to the newly added states, the 19^- state has also been observed decaying to the 17^- state through a tentative in-band E2 transition of 406 keV energy. Spectra showing these newly identified tentative inter-band E1 transitions and the in-band E2 transition from the negative-parity band are given in figure 5.2. In figure 5.2 (a), a gate set on 231 kev clearly shows the previously established 364, 373, and 380 keV E1 transitions depopulating the negative parity band. To see the new E1 transtions more clearly, a sum of gates from the 231 keV line up to 389 keV transition in the ground state band is shown in figure 5.2 spectrum (b). The 356 keV gate was left out of this sum as transitions near the 356 keV appear in the bands of ^{231}Pa (see figure 5.3 in section 5.1.2). The new transitions of 327 and 336 keV are lying at energies consistent with an extrapolation of gamma-ray energies from the previously established E1 transitions, as indicated on the figure 5.2 (b). The 406 keV line from the decay of the 19^- state is also weak; it is almost covered by the background. The new transitions remain tentative because statistics in individual gates are poor, so their placement cannot be precisely determined.

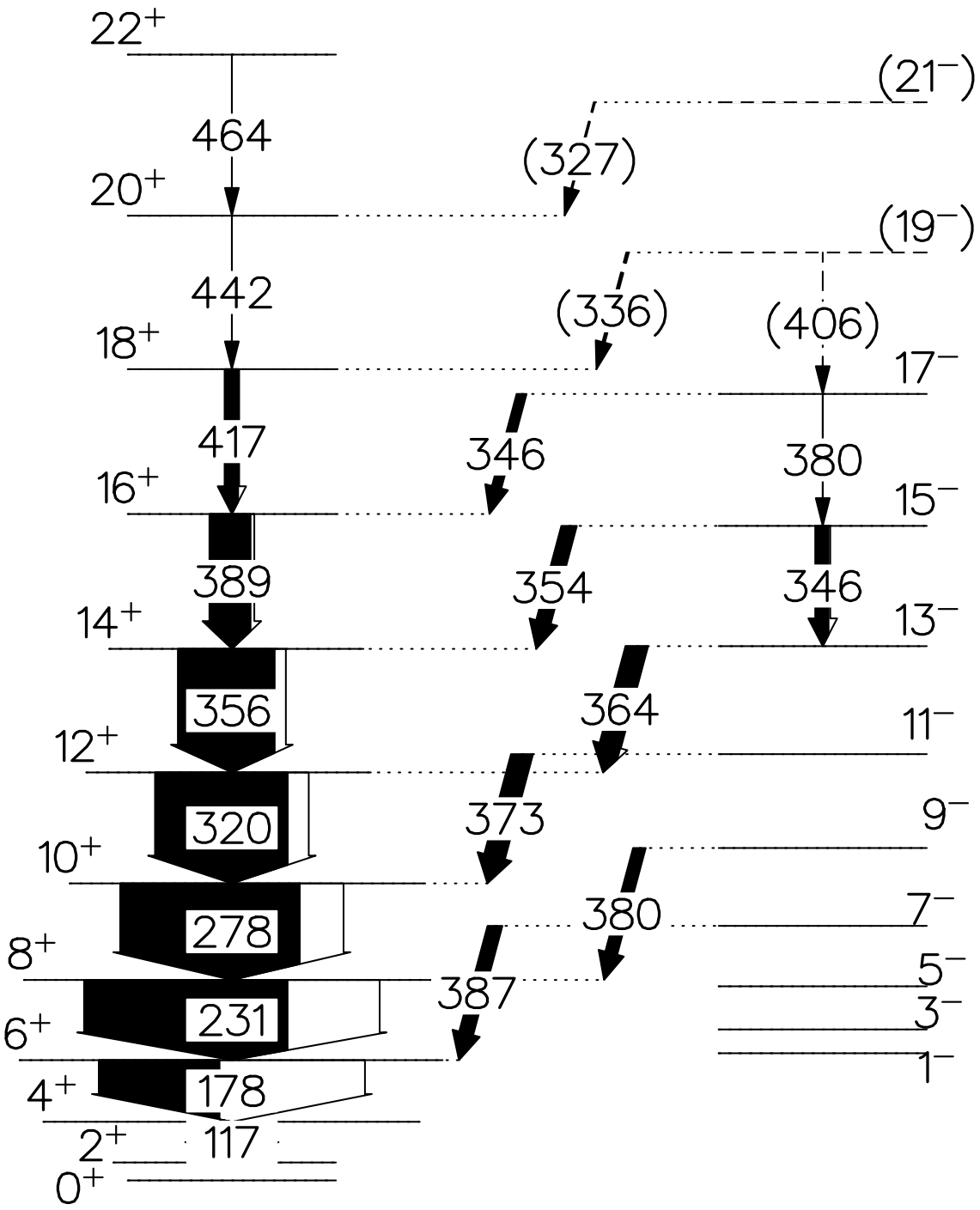

Figure 5.1: *A partial level scheme for* ^{230}U *showing gamma-ray transition observed in the present work.*

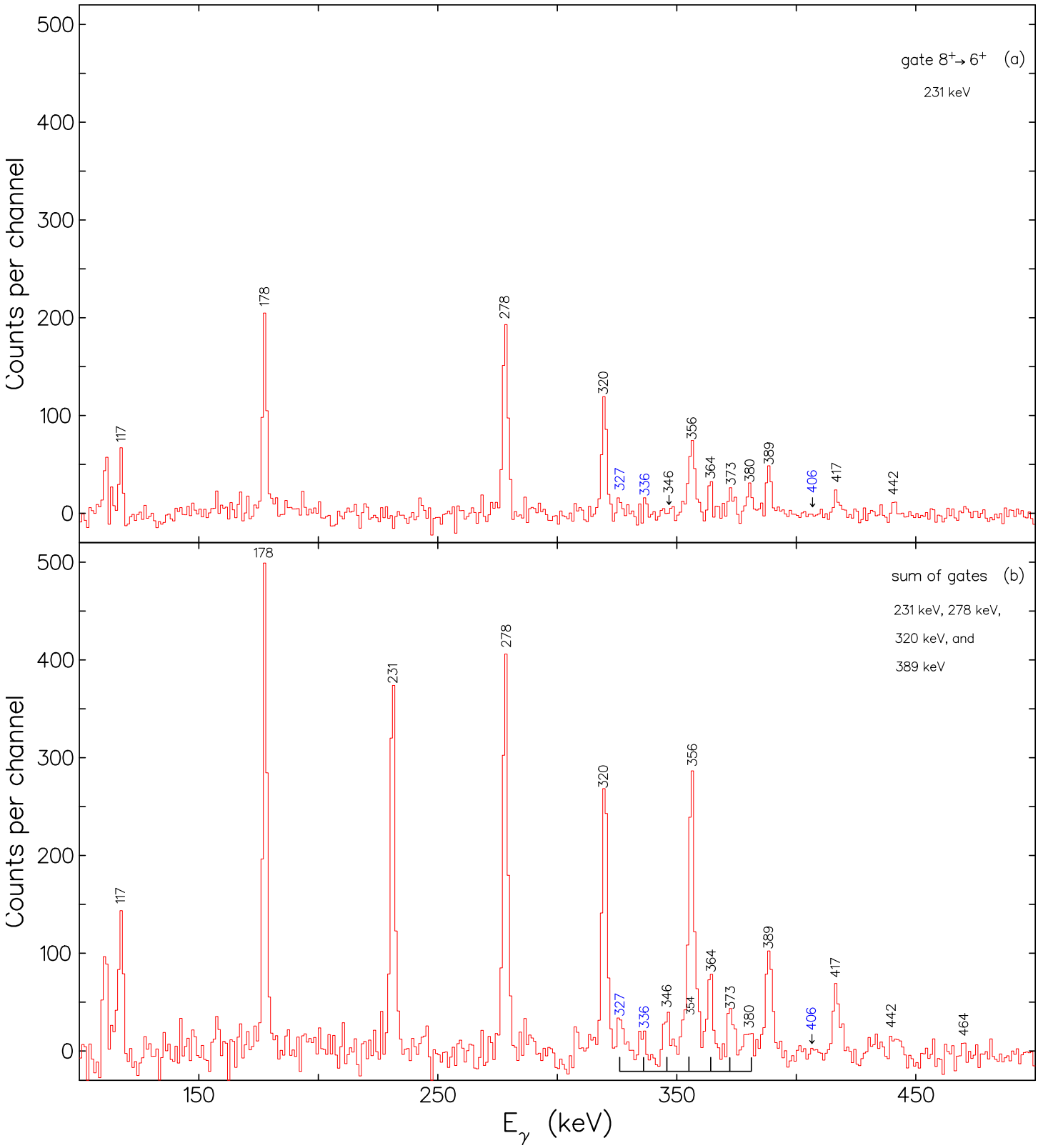

Figure 5.2: *Coincidence projection spectra for the sum of gates: 231 keV, 278 keV, 320 keV, and 389 keV from the ground state band in (a) and 231 keV gate in (b), showing peaks for the observed transitions in the ground state and negative-parity bands of* ^{230}U. *The new transitions observed in this work are labeled in blue, and the other transitions labeled in black were observed from another work [6, 7].*

5.1.2 Other nuclei populated in the experiment

The level schemes obtained when analysing the data shows that not only the nucleus of interest was populated during the experiment. These nuclei were detected by the recoil detector. Their level schemes are shown in figure 5.3 and figure 5.4. Some of these reaction products were not predicted by the fusion-evaporation code PACE4 simulation (see figure 3.4 and table C.1). The population of these nuclei has been explained by transfer reactions [43], which are outside the scope of PACE4. The most strongly populated of these was ^{231}Pa, and the other nucleus was ^{232}U.

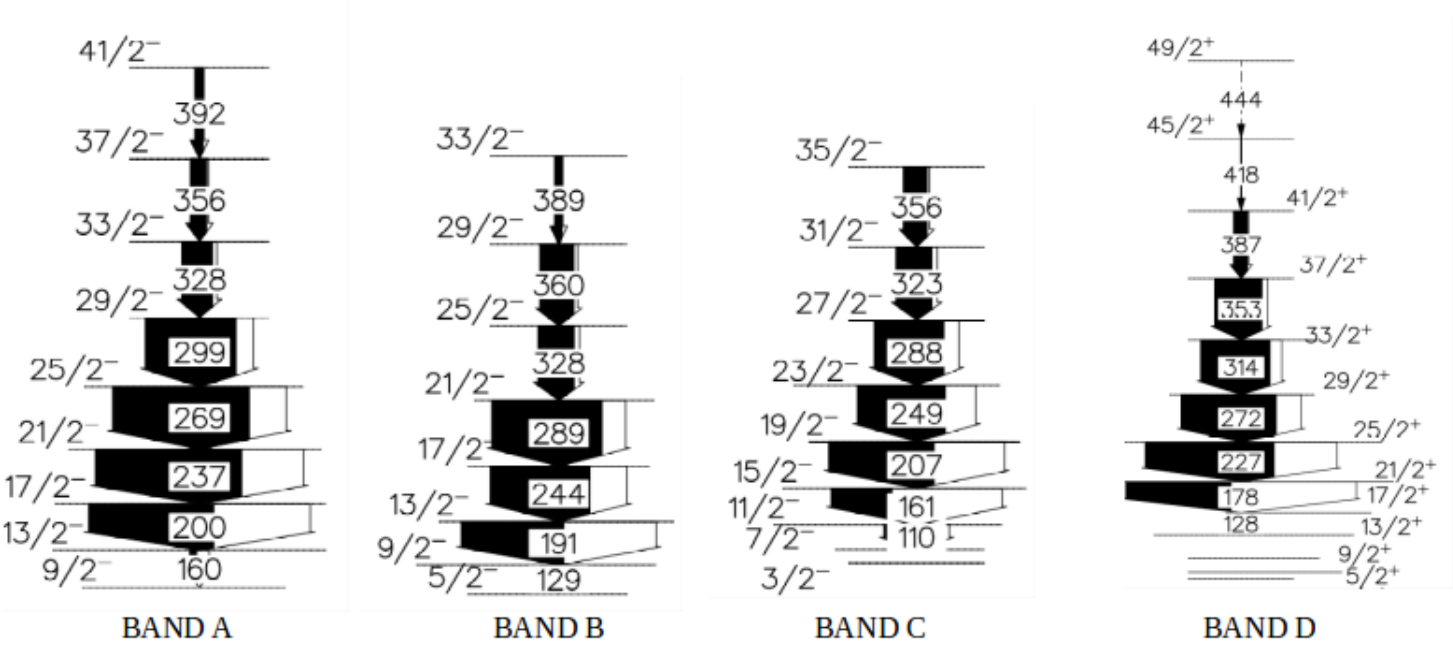

Figure 5.3: *Partial level schemes of ^{231}Pa observed via unexpected transfer which are outside the scope of PACE4.*

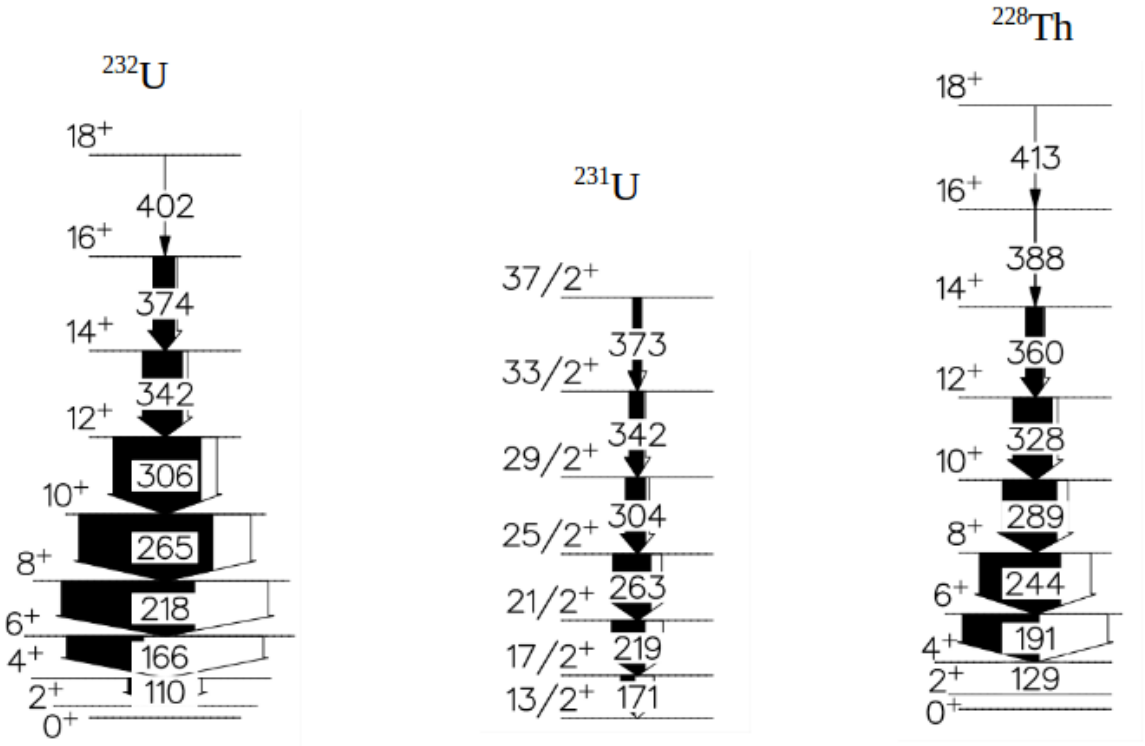

Figure 5.4: *Partial level schemes of* ^{232}*U (left),* ^{231}*U (middle), and* ^{228}*Th (right) observed in the reaction of* ^{232}*Th +* α *at 63 MeV.*

5.2 Discussion

Measurements of quadrupole moments for ^{230}U should be used as a test for the possible existence of tetrahedral shape in ^{230}U. However, this becomes a challenge since the nucleus is weakly populated due to a small production cross-section, precluding lifetime measurements. Therefore, with assumptions about quadrupole moments, intrinsic dipole moments D_0 and energies of the negative-parity band for ^{230}U are compared with neighbouring nuclei to see what conclusions can be drawn.

In a previous study [44], it was observed that the energies for the negative-parity bands for N = 138 isotones, ^{230}U, ^{226}Ra, and ^{228}Th are very similar, when compared by aligning the energies of the 1^- states of the negative-parity bands. The corresponding energies of the negative-parity bands are the same within a few keV. Figure 5.5 and figure 5.6 shows the comparison between the corresponding energies of these bands. The new transition, 406.4 keV in ^{230}U, identified from this thesis work, is also within a few keV when compared to 404.4 keV from ^{226}Ra. But it is also significant to notice

the large energies of the inter-band E1 transitons in ^{230}U when compared to those of ^{226}Ra.

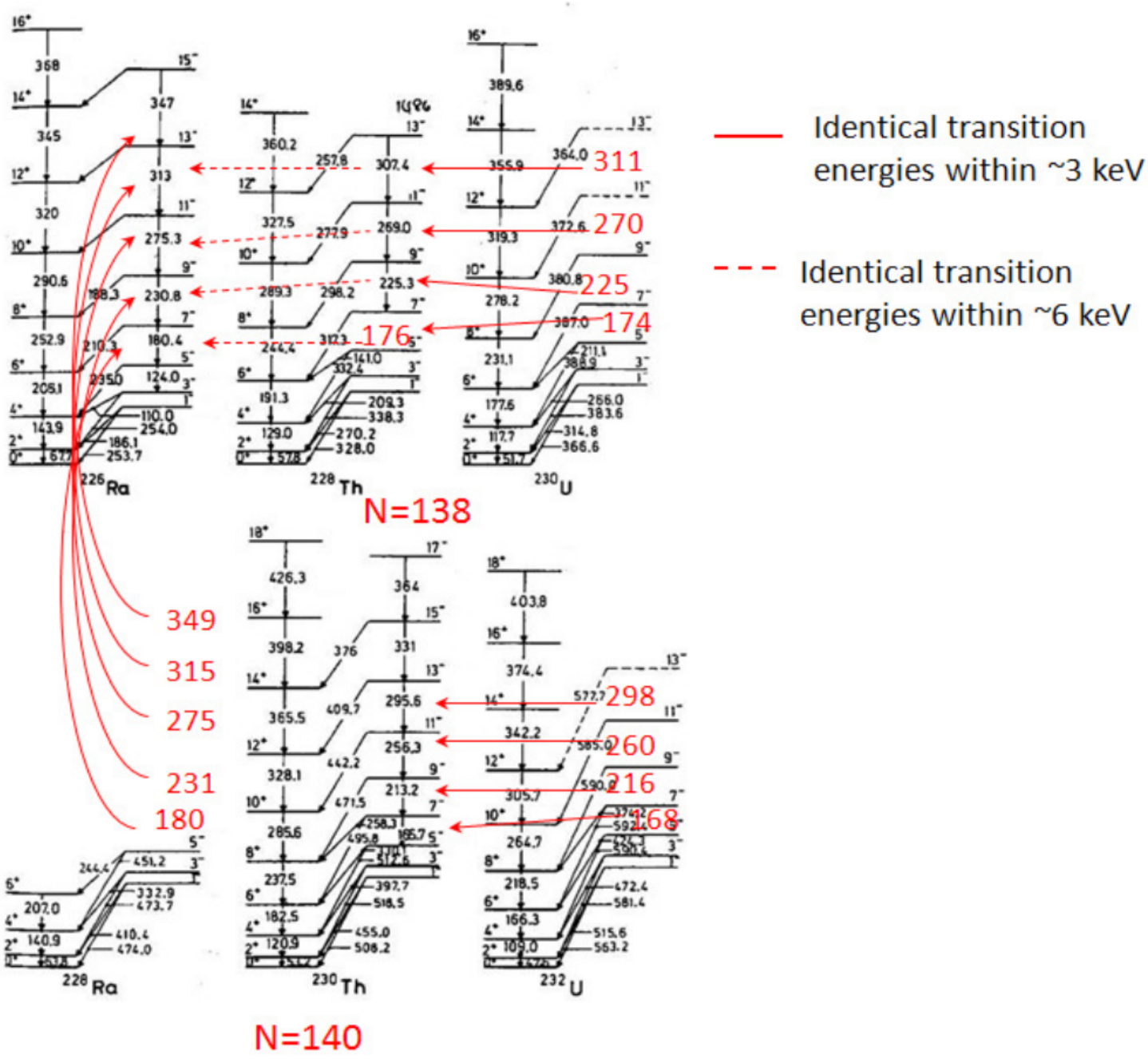

Figure 5.5: *Comparing the transition energies for $N = 138$ and $N = 140$ isostones. Level schemes taken from [6, 44]. The figure is taken from [45].*

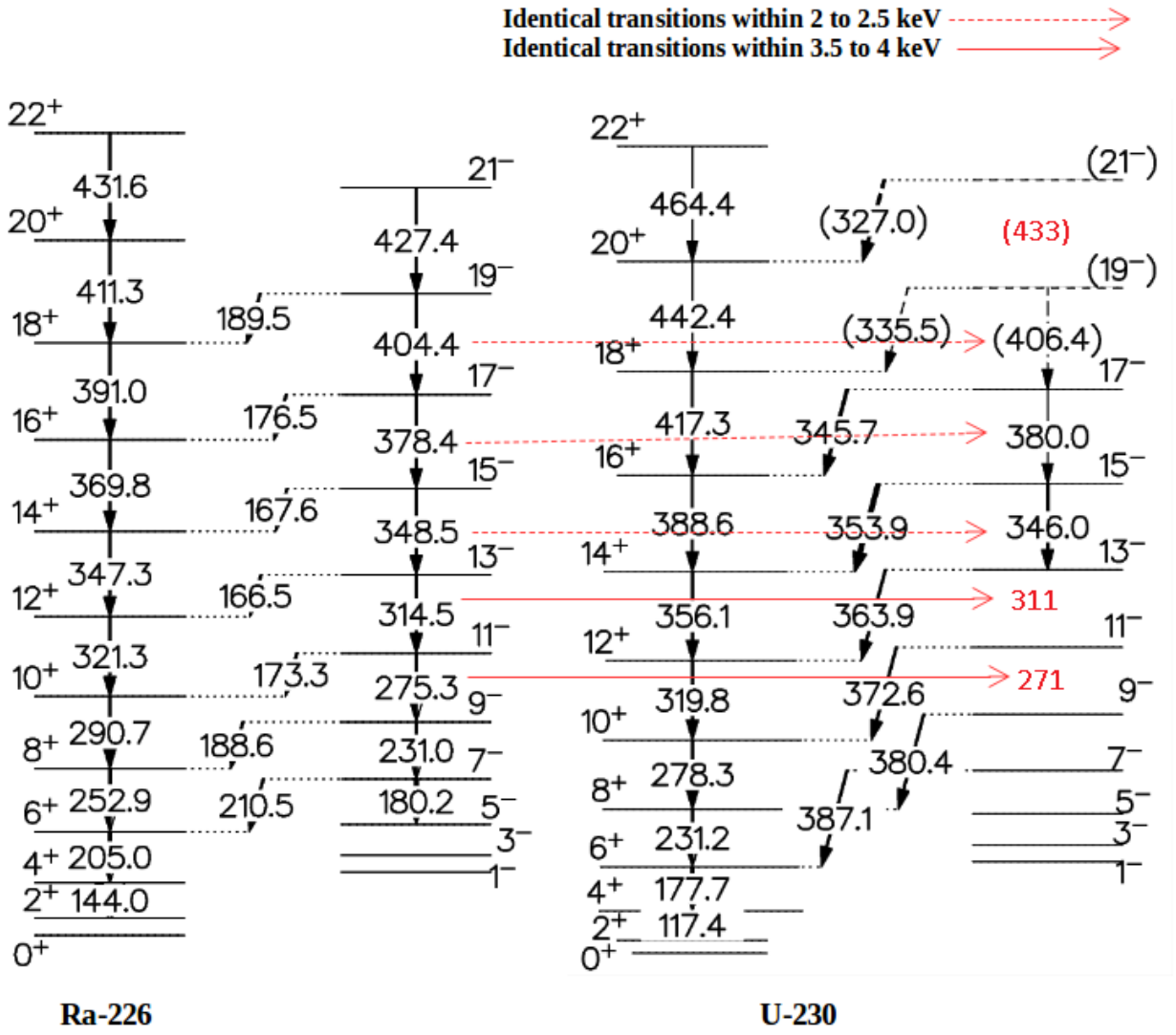

Figure 5.6: *Comparing the transition energies for ^{230}U, and ^{226}Ra nuclei by aligning the energies of the 1^- state of the negative-parity bands. Data for ^{226}Ra taken from [14].*

Figure 5.7 shows the energies of the negative-parity bands less a rigid rotor, for ^{230}U, ^{226}Ra, and ^{228}Th. The negative-parity band for ^{230}U, shows a similar behaviour with the other negative-parity bands for ^{226}Ra, and ^{228}Th, except at spin $> 15\ \hbar$ for ^{228}Th. The band of ^{226}Ra has been established as exhibiting static octupole deformation [21], and the band for ^{228}Th appears to be an octupole vibrations [6, 20]. Therefore, even without observing the in-band E2 transitions in between the low-lying negative-parity states for ^{230}U, the strong structural similarities of the negative parity band in ^{230}U to the case pure octupole deformation in ^{226}Ra, implies an octupole deformation or vibration rather than tetrahedral deformation.

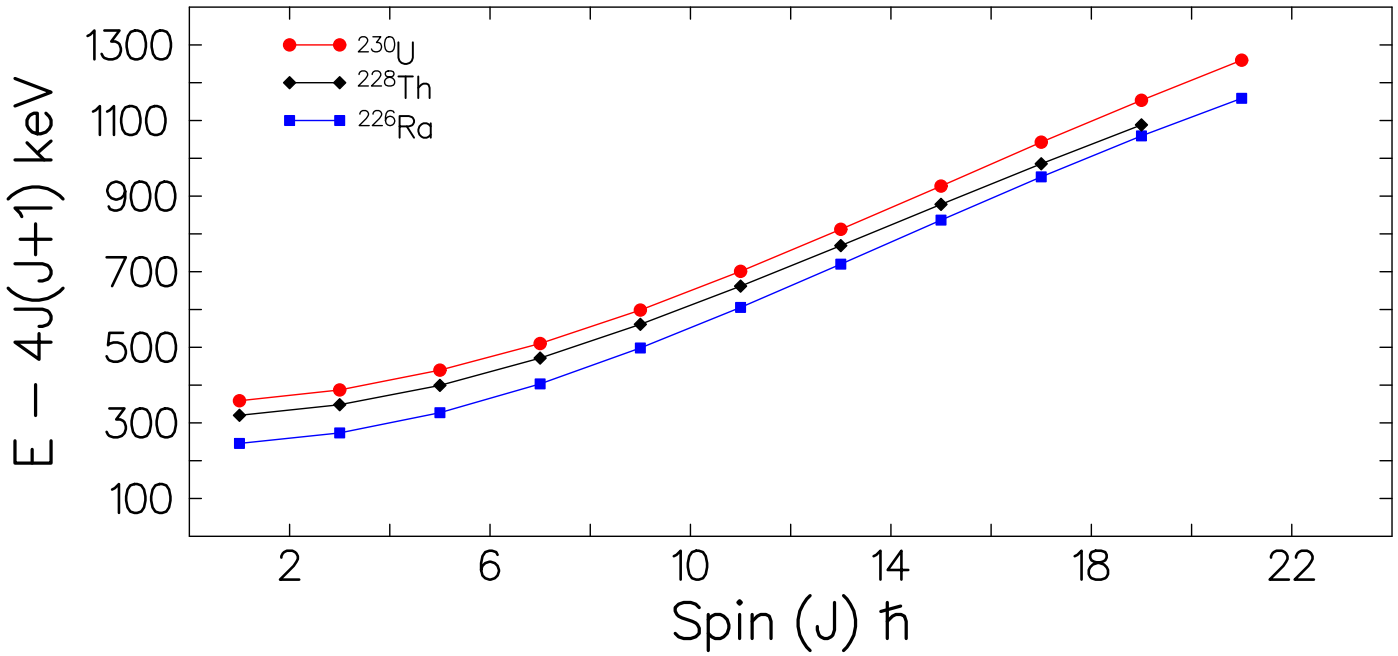

Figure 5.7: *Comparison of the excitation energies of the negative-parity bands for* ^{230}U*,* ^{226}Ra*, and* ^{228}Th*. A rigid rotor reference has been subtracted. The energies for* ^{226}Ra *and* ^{228}Th *are taken from [6, 21, 44].*

Figure 5.8 shows the energies, less a rigid rotor for the ground state bands and negative-parity bands for the isotones ^{230}U, ^{228}Th, and ^{226}Ra. In ^{226}Ra with the increasing spin, the ground and negative-parity bands merge to form a band of alternating parity [21]. The appearance of alternating parity rotational bands is one of the characteristic of static octupole deformation [13, 19]. In ^{228}Th with increasing spin, the bands do not merge but rather appear to cross each other. For ^{230}U, the negative-parity band stays much higher above the ground state band. This makes the population of the negative-parity band less favourable through fusion-evaporation reactions. This might also explain why it is difficult to observe the in-band E2 transitions. With almost the same in-band E2 transition energies as ^{226}Ra, the in-band E2 transition rates could be expected to remain the same. However, the inter-band E1 energies for ^{230}U are larger than those of ^{226}Ra, meaning that the inter-band E1 transition rates for ^{230}U would increase, since $E^3_\gamma(E1)$ would increase relative to $E^5_\gamma(E2)$. Therefore, if $E^3_\gamma(E1) \gg E^5_\gamma(E2)$ and the transition rate for the $(E1)$ is also high, the band will decay through the inter-band E1 transtions. This is the case for an octupole vibration, and it will result in a lack of in-band E2 transitions being observed between the low-lying negative parity states.

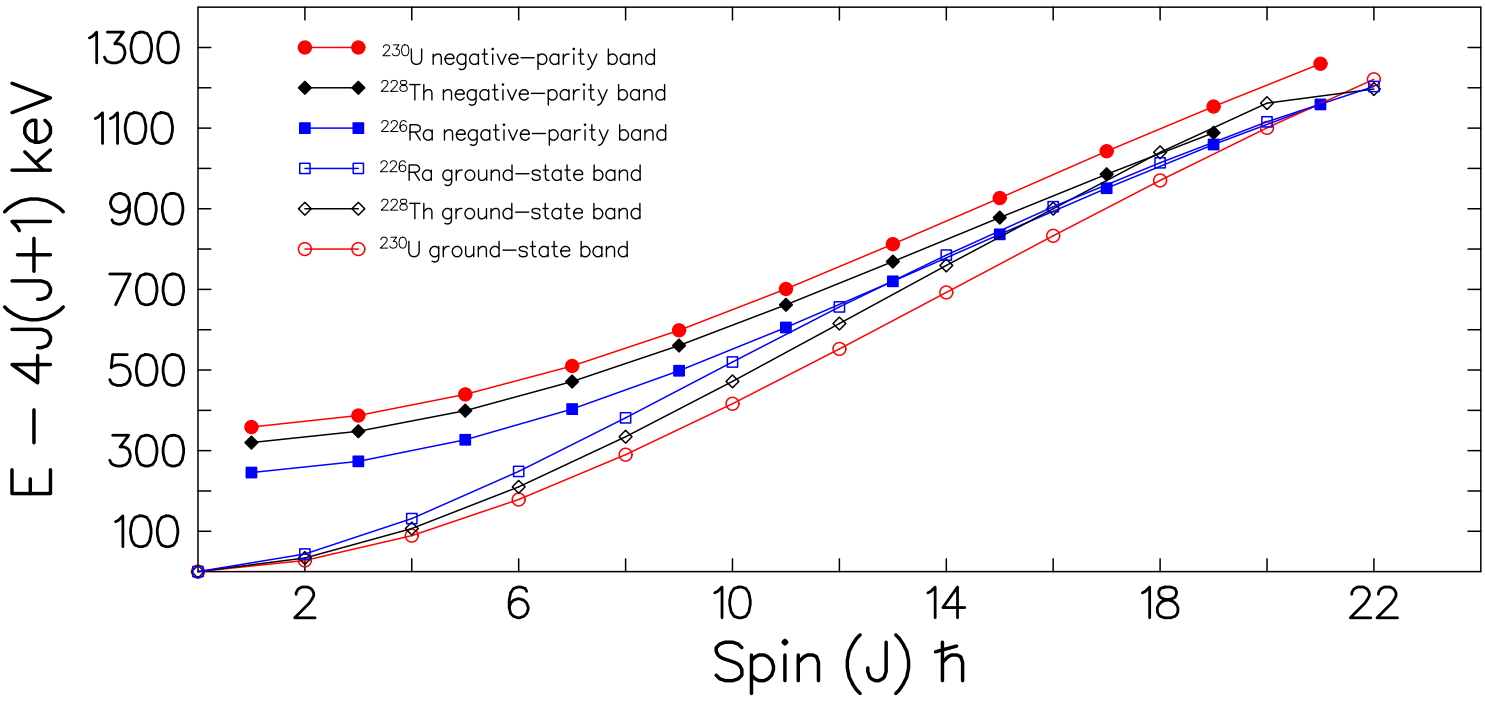

Figure 5.8: *Comparison of the excitation energies of negative-parity bands and ground state bands for* ^{230}U *and* ^{226}Ra*. A rigid rotor reference has been subtracted. The energies for* ^{226}Ra *are taken [21].*

To further establish the structural similarities from the systematics of Ra, Th, and U nuclei, intrinsic electric dipole moments for ^{230}U were calculated and compared to aforementioned nuclei. The intrinsic dipole moments for ^{230}U were calculated from the $B(E1)/B(E2)$ branching ratios using the strong-coupling limit of the rotational model [23].

$$D_0 = \left[\frac{5(I-1)B(E1; I \rightarrow I-1)}{8(2I-1)B(E2; I \rightarrow I-2)}\right]^{1/2} Q_0 \tag{5.1}$$

The $B(E1)/B(E2)$ branching ratios were calculated from the measured gamma-ray energies and intensities using equation 2.19. The magnitudes of the calculated intrinsic electric dipole moments and $B(E1)/B(E2)$ ratios are listed in table 5.1. The values for the intrinsic dipole moments were calculated using the measured $Q_0 = 1000\ fm^2$ for the ground band [7]. Figure 5.9 shows a plot of the magnitude of the intrinsic dipole moments $|D_0|$ averaged over $I > 7$ values for Uranium isotopes, plotted against neutron numbers. The value of $|D_0|$ for ^{230}U obtained from this work is plotted in red. The value does not agree well with the values from previous measurements [6,7], it is larger and has a bigger uncertainty. But what is evident from figure 5.9 is that, the nuclei known and suspected to be stable octupole-deformed, have large intrinsic dipole moments. These nuclei have $N < 138$. Nuclei

associated with octupole vibration have small intrinsic dipole moments and have $N > 140$. The nucleus ^{230}U lies in the transition region and close to the octupole vibrators, thereby it is expected to demonstrtate much more of an octupole vibrational character. A similar behaviour is also observed for nuclei in the systematics [7]. Despite adding no new bands to the existing level scheme, the band of interest was populated with modest addition of two nuclear levels and a tentative in-band E2 transition connecting these new levels. In addition, the obtained results have been explained in the context of a systematic comparison.

Table 5.1: *Intrinsic dipole moments and $B(E1)/B(E2)$ ratios for ^{230}U.*

spin ($\hbar$)	$\frac{B(E1;I\rightarrow I-1)}{B(E2;I\rightarrow I-2)}$ fm^{-2}	$\lvert D_0\rvert$ $e.fm$
15	1.417×10^{-7}	0.199(15)
17	2.729×10^{-7}	0.288(12)
19	1.858×10^{-7}	0.238(20)
Average		0.242(45)

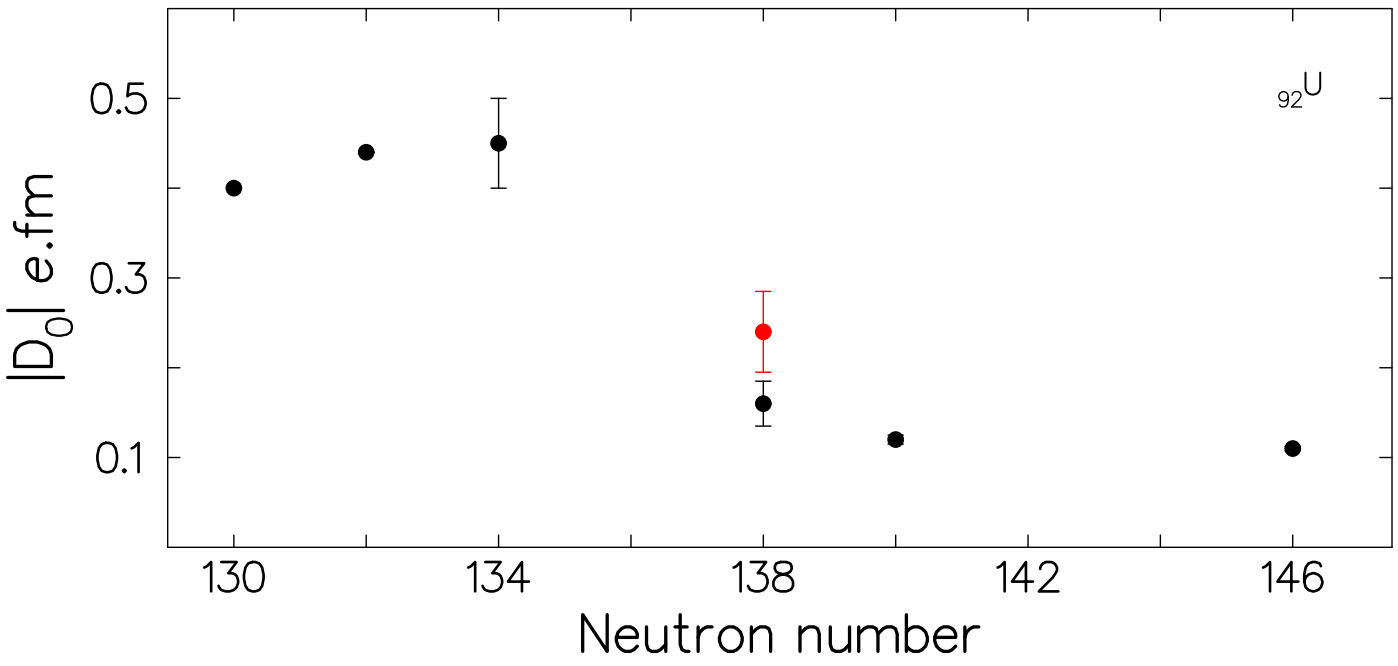

Figure 5.9: *Instrinsic dipole moments of ^{222}U, ^{224}U, ^{226}U, ^{230}U, ^{232}U, and ^{238}U vs neutron number. The value for $|D_0|$ obtain from this thesis work is marked with red. The other values are taken from [23] (^{222}U, ^{224}U, and ^{226}U), [7](^{230}U,and ^{232}U), [46](^{238}U).*

Chapter 6

Summary and Conclusion

In this study the nucleus of ^{230}U has been investigated in an attempt to observe more E2 transitions within its negative-parity band. The nucleus was described in terms of octupole vibrations yet it was still missing E2 transitions from its low-lying negative-parity states [7, 18].

The ^{230}U nucleus has been populated from the nuclear reaction ^{232}Th + ^{4}He, through the reaction channel (α, 6n) at 63 MeV beam energy, at iThemba LABS. The emitted gamma-rays from the evaporation-residues were detected and measured with AFRODITE coupled with a recoil detector. The recoil detector uses a time-of-flight method to separate fusion-evaporation residues from fission fragments that contributes to high background in the reaction ^{232}Th + ^{4}He. The use of the recoil detector was succesful in reducing the background. The study was intended to observe in-band E2 transitions in the low-lying negative-parity states as this would provide a clearer and better understanding whether they belong to the tetrahedral symmetry hypothesis, or are actually octupole vibrations as some studies suspect or suggest [7, 18, 28]. No in-band E2 transitions were observed in the low-lying negative-parity states, but two new states, 19^{-} and 21^{-} have tentatively been added on top of the negative-parity band. These states were observed with E1 transitions connecting them to the positive-parity band. Only one new tentative in-band E2 transition of 406 keV could be observed in the negative-parity band of ^{230}U. The energies of the observed states and transitions were compared with the energies of the octupole deformed neighboring nuclei, ^{226}Ra, ^{228}Th. The energies were found to be the same within a few keV as was first noticed by Zeyen *et al.,* [44].

Intrinsic dipole moments $|D_0|$, and $B(E2)/B(E1)$ ratios were calculated using the energies and intensities of the measured gamma-rays and the Q_0 of the $2^+ \rightarrow 0^+$ transition. The intrinsic dipole moments were also compared to the systematics of neighbouring nuclei as a function of neutron number. In the systematics, close similarities were also noticed in the behaviour of $|D_0|$ as it was noticed by Ntshangase *et al.,* [7], when the neutron number is varied. Therefore, with the fact that the energies and $|D_0|$ of ^{230}U are still comparable to the systematics, it is suggested that the low-lying negative-parity states for ^{230}U could be octupole vibrational in nature even without observing the in-band E2 transitions. And again, from the expression 2.21, it is suggested that for ^{230}U, $B(E1)$ might be much greater than $B(E2)$ which will result to the in-band E2 transitions not being observed from the low-lying negative-parity states. In this regard, despite the elusive in-band E2 transitions, through a systematic comparison of dipole moments (and other observables) of neighbouring nuclei, the main conclusion of this work is that the low-lying negative-parity states for ^{230}U could be octupole vibrational in nature.

Appendix A

Gamma-ray intensities for ^{230}U

Table A.1: *The intensity of the measured gamma-rays in* ^{230}U.

Energies (keV)	I_i^π	I_f^π	Type	Intensity(error)
117	4^+	2^+	E2	10(1)
178	6^+	4^+	E2	232(49)
231	8^+	6^+	E2	391(28)
278	10^+	8^+	E2	345(20)
320	12^+	10^+	E2	255(15)
356	14^+	12^+	E2	186(12)
389	16^+	14^+	E2	79(8)
417	18^+	16^+	E2	26(6)
442	20^+	18^+	E2	17(10)
346	15^+	13^+	E2	20(10)
380	17^+	15^+	E2	17(12)
406	19^+	17^+	E2	11(6)
387	7^-	6^-	E1	27(21)
380	9^-	8^+	E1	23(6)
373	11^-	10^+	E1	40(9)
364	13^-	12^+	E1	41(7)
354	15^-	14^+	E1	28(12)
346	17^-	16^+	E1	20(7)
336	19^-	18^+	E1	13(12)
327	21^-	20^+	E1	8(6)

The intensities of the measured gamma-rays in ^{230}U are listed in table A.1. To obtain the gamma-ray intensities, the peaks were fitted in GF3. The equation A.1 was used to calculate the intensities.

$$I_\gamma = N/\varepsilon \tag{A.1}$$

where N is the counts for the area of the gamma-ray peak from the GF3 fit, and ε is the efficiency of the clover detector.

Appendix B

Reduced transition probability and Weisskopf estimates

The relation between the reduced transition probability $B(\sigma\lambda)$ and the nuclear matrix element is given by:

$$B(\sigma\lambda, I_i \to I_f) = \sum_{\mu K_f} | < I_f K_f | \hat{\mathbf{O}}_\lambda | I_i K_i > |^2 \tag{B.1}$$

From the Wigner-Eckart theorem, the matrix element can be factorized

$$< I_f K_f | \hat{\mathbf{O}}_\lambda | I_i K_i >= (I_i K_f | I_f K_f) < I_i || \hat{\mathbf{O}}_\lambda || I_i > \tag{B.2}$$

where $(I_i K_f | I_f K_f)$ is a Clebsch-Gordan coefficient. Using the orthonomality of the Clebsch-Gordan the reduced transition probability can be expressed as:

$$B(\sigma\lambda, I_i \to I_f) = \frac{1}{2I_i + 1} | < I_f \| \hat{\mathbf{O}}_\lambda \| I_i > |^2 \tag{B.3}$$

The power carried away by the electric or magnetic radiation will be given by:

$$P(\sigma L) = \frac{2(L+1)c}{\varepsilon_0 L[(2L+1)!!]^2}\left[\frac{\omega}{c}\right]^{2L+2} B(\sigma L) \tag{B.4}$$

From equation B.4, the probability per unit time for gamma-ray emission will be given by:

$$T(\sigma L) = \frac{P(\sigma L)}{\hbar\omega} = \frac{2(L+1)}{\varepsilon_0 L\hbar[(2L+1)!!]^2}\left[\frac{\omega}{c}\right]^{2L+1} B(\sigma L) \tag{B.5}$$

Assuming that the gamma-ray emission is from the initial state to the final state is due to a transition of a single proton, the electric and magnetic transition rates can be estimated with the fomulae B.6 and B.7 respectively:

$$T(EL) = \frac{8\pi(L+1)}{\hbar L((2L+1)!!)^2}\left(\frac{e^2}{4\pi\varepsilon_0\hbar c}\right)\left[\frac{E_\gamma}{\hbar c}\right]^{2L+1}\left(\frac{3}{L+3}\right)^2 cR^{2L} \tag{B.6}$$

, and

$$T(ML) = \left(\mu_p - \frac{1}{L+1}\right)^2\left(\frac{se^2}{4\pi\varepsilon_0\hbar c}\right)\left(\frac{\hbar}{m_p c}\right)^2\left[\frac{E_\gamma}{\hbar c}\right]^{2L+1}\left(\frac{3}{L+3}\right)^2 cR^{2L-2} \tag{B.7}$$

where m_p is the mass of the proton, and μ_p is the magnetic moment. Estimates for lower multipole orders can be made if, let $R = R_0 A^{1/3}$ and the term $\left(\mu_p - \frac{1}{L+1}\right)$ to be equal to 10 [22]. These estimates are known as Weisskopf estimates and are listed in table.

Table B.1: *Weisskopf estimates for lower multipole orders [22].*

λ(E1)=$1.0\times10^{14}A^{2/3}E^3$	λ(M1)=$5.6\times10^{13}E^3$
λ(E2)=$7.3\times10^{7}A^{4/3}E^5$	λ(M2)=$3.5\times10^{7}A^{2/3}E^5$
λ(E3)=$34\times A^2E^7$	λ(M3)=$16A^{4/3}E^7$
λ(E4)=$1.1\times10^{-5}A^{8/3}E^9$	λ(M4)=$4.5\times10^{-6}A^2E^9$

Parity selection rule for magnetic transition equation B.6 and electric transition equation B.7 [22].

$$\pi(ML) = (-1)^{L+1} \tag{B.8}$$

$$\pi(ML) = (-1)^{L} \tag{B.9}$$

Appendix C

PACE4 simulation for the reaction

Table C.1: *Reaction* $^{232}Th(\alpha, xn)$ *cross-section calculations from PACE4 at 63 MeV.*

1.Yields of residual nuclei

Z	N	A	events	percent	x-section(mb)
92	139	**231 U**	2	0.2%	3.84
92	138	**230 U**	13	1.3%	25
90	138	**228 Th**	1	0.1%	1.92
Total fission			984	98.4%	1.89e+03
TOTAL			1000	100%	1.92e+03

Bibliography

[1] J. Dudek *et al.,* Phys. Rev. Lett. 88, No.25, 252502 (2002).

[2] N. Schunck *et al.,* Phys. Rev. C **69**, 061305 (2004).

[3] J. Dudek *et al.,* Phys. Pol. B **38**, 1389 (2007).

[4] J. Dudek *et al.,* Phys. Rev. Lett. **97**, 072501 (2006).

[5] M.Jentschel *et al.,* Phys. Rev. Lett. **104**, 222502(2010).

[6] B. Ackermann *et al.,* Nucl. Phys. A **559**, 61 (1993).

[7] S. S. Ntshangase *et al.,* Phys. Rev. C **82**, 041305 (2010).

[8] J.Lilley. *Nuclear Physics Principle and Applications.* Wiley, 2001: page 54-58.

[9] E. Lawrie. Introduction to Nuclear Physics Notes (2018).

[10] S.S Ntshangase, PhD thesis, University of Cape Town (2011).

[11] B. Hadinia, MSc thesis, Stockholm University (2006).

[12] https://nscl.msu.edu/news/science/news-S43.html.

[13] P. A. Butler and W. Nazarewicz, Rev. Mod. Phys. **68**, 349 (1996).

[14] P. A. Butler, J. Phys. G: Nucl. Part. Phys. **43** 073002 (2016).

[15] X. Wang *et al.*, Phys. Rev. Lett. **102**, 122501 (2009).

[16] M. P. Carpenter, R. V. F. Janssens, S. Zhu, and S. Frauendorf, J. Phys.: Conf. Ser. **312**, 092006 (2011).

[17] L. M. Robledo, and R. R. Rodriguez-Guzman, J. Phys. G: Nucl. Part. Phys. **39**, 105103 (2012).

[18] P. A. Butler, Proc. R. Soc. A **476**, 20200202 (2020).

[19] I. Ahmad and P.Butler, Annu. Rev. Nucl. Part. Sci. **43**, 71 (1996).

[20] J. F. C. Cocks *et al.,* Nucl. Phys. A **645**, 61 (1999).

[21] H. J. Wollersheim et al., Nucl. Phys. A 556, 261 (1993).

[22] K. S. Krane, *Introductory Nuclear Physics*, John Wiley and Sons, Inc., New York (1988).

[23] P. A. Butler and W. Nazarewicz, Nucl. Phys. A **533**, 249 (1991).

[24] E. Garrote, J.L.Egido, and L.M. Robledo, Phys. Lett. B **B410**, 86 (1997).

[25] E. Garrote, J.L.Egido and L.M. Robledo, Phys. Lett. **80**, 4398 (1998).

[26] X. Li and J. Dudek, Phys. Rev. C **94** R1250 (1994).

[27] R. A. Bark *et al.,* Phys. Rev. Lett. **104**, 022501 (2010).

[28] D Curien, J Dudek, and K Mazurek, J. Phys.: Conf. Ser. **205**, 012034 (2010).

[29] N. Bohr, Nature 137, 344 (1936).

[30] Gamma Sphere Online Booklet.

[31] https://www.britannica.com/science/nuclear-fission/The-stages-of-fission.

[32] S.S. Ntshangase, Nuclear Reaction Notes, University of Zululand (2017).

[33] A. Gavron, Phys. Rev. C21, 230 (1980).

[34] A. Gavron, Computational Nuclear Physics 2, Nuclear Reactions, Spinger-Verlag New York, Inc, 108 (1993).

[35] http://www.Srim.org, 2006.

[36] G.F. Knoll. Radiation Detection and Measurement. 2nd Edition, Wiley, New York. ISBN O-471-81504-7.

[37] F. A. Beck, Th. Byrski, D. Durien, G. Duchene, G. de France, B. Kharraja, L. Wei, P. Butler, G. Jones, P. Jones, & F. Hannachi. (1992). The Clover detector.

[38] S. L. Shepherd *et al.,* Nucl. Instrum. Methods Phys. Res. A 434, 373 (1999).

[39] P. M. Jones *et al.,* Nucl. Instrum. Methods Phys. Res. A 362, 556 (1995).

[40] Hamamatsu photonics K.K MCP and MCP assembly; URL: www.hamamatsu.com.

[41] Pixie-16 User Manual.

[42] D. C. Radford, Nucl. Instrum. Methods Phys. Res., Sect. A 361, 297 (1995).

[43] T. Nishi et al., RCNP Osaka Ann. Rep. p.119 (1980).

[44] P. Zeyen et al., Z. Phys. A 328, 399 (1987).

[45] R. A. Bark *et al.,* Nuclear Structure Conference, Oral presentation, Lawrence Berkeley National Laboratory, (2010).

[46] D. Ward *et al.,* Nucl. Phys. A **600**, 88 (1996).